

**DIAMETERS AND VELOCITIES FOR CHARGED LIQUID DROPS
UNDERGOING AERODYNAMIC BREAKUP**

by
Ze Yang

A Thesis

*Submitted to the Faculty of Purdue University
In Partial Fulfillment of the Requirements for the degree of*

Master of Science in Aeronautics and Astronautics



School of Aeronautics & Astronautics

West Lafayette, Indiana

May 2019

THE PURDUE UNIVERSITY GRADUATE SCHOOL
STATEMENT OF COMMITTEE APPROVAL

Dr. Paul E. Sojka, Chair

School of Mechanical Engineering

Dr. Sally P.M. Bane, Chair

School of Aeronautics and Astronautics

Dr. Jun Chen

School of Mechanical Engineering

Approved by:

Dr. Weinong Chen

Head of the Graduate Program

ACKNOWLEDGMENTS

I studied in Purdue University for two years as a master student. Although the period is short, it still filled with wonderful memories. And I am glad that I have met so many good people.

First, I would like to thank Professor Sojka. He is a kind and experienced advisor. He could always provide some useful and valuable advices. Under his guidance, I learned a lot. I am really happy to study and work in his group.

And I would like to thank other of my committee members, Professor Sally Bane and Professor Jun Chen. They are also very kind and provide me help in time.

Furthermore, I would like to thank the graduates helping with my experiments: Dayna Obenauf, Weixiao Shang, Yijie Wang.

Finally, I want to thank the staffs in Purdue University. They are kind and offer me help with high efficiency.

I am really happy having a chance to study in Purdue University and to meet all these people. And these two years are unforgettable period in my life.

TABLE OF CONTENTS

LIST OF TABLES	7
LIST OF FIGURES	8
LIST OF SYMBOLS	11
ABSTRACT.....	14
1. INTRODUCTION	15
1.1 Electrostatic Atomization.....	16
1.2 Scope.....	21
1.3 Thesis Organization	22
2. LITERATURE REVIEW	23
2.1 Experimental methods on secondary breakup	24
2.1.1 Shock Tube	24
2.1.2 Continuous Jet	25
2.1.3 Drop Tower.....	26
2.1.4 Hybrid Method.....	26
2.2 Breakup Process Description	27
2.3 Breakup Modes	29
2.3.1 Vibrational Breakup.....	29
2.3.2 Bag Breakup	29
2.3.3 Multimode Breakup	31
2.3.4 Sheet-thinning Breakup	32
2.3.5 Catastrophic Breakup.....	34
2.4 Dimensionless Parameters	34
2.4.1 Weber Number.....	35
2.4.2 Ohnesorge Number	35
2.4.3 Reynolds Number	37
2.4.4 Density Ratio	38
2.5 Fragment Size and Velocity Distribution	39
2.6 Charged Droplets	41
2.7 Summary and Conclusion	43

3.	ANALYSIS OF CHARGED DROPLET	45
3.1	Definition of Charge Number	45
3.2	Range of Applied High Potential	46
3.3	Breakup Model of Charged Drop	46
3.4	Force Analysis of Drop and Fragments	49
3.5	Summary and Conclusions	51
4.	EXPERIMENTAL APPARATUS	53
4.1	Material Properties	53
4.2	Charged Droplet Production	53
4.3	Air Jet Production	56
4.4	High Speed Imaging System	60
4.4.1	Shadowgraph Imaging System	60
4.4.2	Digital In-line Holography (DIH) System	61
4.5	Traversing System	62
4.6	Fragment Charge Measuring Component	63
4.7	Experiment Produce	64
4.8	Experimental Uncertainty	65
4.8.1	Uncertainty in the Weber Number	66
4.8.2	Uncertainty in the Charge Number	66
4.8.3	Uncertainty in the Minimal Detected Acceleration	67
4.8.4	Uncertainty in the Minimal Applied Potential	67
5.	RESULTS	69
5.1	Criteria for Data Processing and Selection	69
5.2	Shadowgraph of Breakup Process	70
5.3	Size Distribution of Charged Breakup Fragments	73
5.4	Velocity Distribution of Charged Breakup Fragments	87
5.4.1	Horizontal Velocity	87
5.4.2	Vertical Velocity	101
5.5	Acceleration of Charged Breakup Fragments	115
6.	SUMMARY AND CONCLUSIONS	117
6.1	Summary of Previous Chapters	117

6.2 Future Work	118
REFERENCES	119

LIST OF TABLES

Table 2.1 Dimensionless parameters in secondary atomization	34
Table 2.2 Transitional Weber number for Newtonian droplets and $Oh < 0.1$	35
Table 4.1 Relevant physical properties of air at 25°C and 1 bar	53
Table 4.2 Relevant physical properties of drop phase liquids	53
Table 5.1 Correspondence between applied potential and charge number of ethanol.....	73
Table 5.2 Correspondence between applied potential and charge number of salt solution.....	73
Table 5.3 Ethanol FWHM of nondimensional fragment size	83
Table 5.4 Salt solution FWHM of nondimensional fragment size	83
Table 5.5 Ethanol peak location of nondimensional fragment size	85
Table 5.6 Salt solution peak location of nondimensional fragment size	85
Table 5.7 Ethanol FWHM of nondimensional horizontal velocity.....	97
Table 5.8 Salt solution FWHM of nondimensional horizontal velocity	97
Table 5.9 Ethanol peak location of nondimensional horizontal velocity.....	99
Table 5.10 Salt solution peak location of nondimensional horizontal velocity	99
Table 5.11 Ethanol FWHM of nondimensional vertical velocity.....	111
Table 5.12 Salt solution FWHM of nondimensional vertical velocity	111
Table 5.13 Ethanol peak location of nondimensional vertical velocity.....	113
Table 5.14 Salt solution peak location of nondimensional vertical velocity	113

LIST OF FIGURES

Figure 1.1 Basic electrostatic device (from Guildenbecher 2009)	16
Figure 2.1 Shock tube experimental apparatus (from Theofanous, 2004).....	24
Figure 2.2 Continuous jet experimental apparatus (from Zhao 2007).....	25
Figure 2.3 Drop tower experimental apparatus (from Jurgen, 2000)	26
Figure 2.4 Breakup modes for Newtonian droplet (from Guildenbecher, 2007).....	28
Figure 2.5 Bag breakup mechanism (from Guildenbecher, 2009).....	30
Figure 2.6 Bag breakup process (from Kulkarni, 2014)	31
Figure 2.7 Bag/plume breakup mode (from Kulkarni, 2014)	32
Figure 2.8 Shear stripping mechanism (from Guildenbecher, 2009).....	33
Figure 2.9 Sheet-thinning mechanism (from Guildenbecher, 2009)	33
Figure 2.10 Relation between WeC and Oh (from Hsiang and Faeth, 1995)	36
Figure 2.11 WeC at different Oh from Brodkey and Kulkarni expressions (from Kulkarni, 2014)	37
Figure 2.12 Simulation results for critical Weber number at different Reynolds number at density ratio of 10(from Han and Tryggvason, 2001)	38
Figure 2.13 Breakup modes at different density ratio conditions (from Jain 2018)	39
Figure 2.14 Charged drop fragmentation morphology for (a) conductive water/0.4% (w/v) salt solution, (b) moderately conductive ethanol and (c) weakly conductive hexane/5% (v/v) ethanol solution (from Guildenbecher 2009).....	43
Figure 3.1 Geometry of deformed droplet in Cartesian coordinate (from Guildenbecher 2009)	47
Figure 3.2 Geometry of deformed droplet in spheriodal coordinate (from Guildenbecher 2009)	47
Figure 3.3 Stress ratio for perfect conducting liquid (from Guildenbecher 2009)	48
Figure 3.4 Stress ratio for moderate conducting liquid (from Guildenbecher 2009).....	49
Figure 4.1 Droplet producing component: [1] syringe tip, [2] nylon body, [3] charging needle (from Guildenbecher 2009).....	54
Figure 4.2 Sample detected voltage signal (from Gamero-Castanoa and Hurby 2002)	55
Figure 4.3 Scheme of examining system (from Guildenbecher, 2007)	56
Figure 4.4 Scheme of air flow component: [1] nozzle body, [2] honeycomb and mesh, [3] radial input ports, [4] droplet nozzle, [5] droplet axial traverse, [6] droplet nozzle radial traverse. (from Guildenbecher, 2009).....	57
Figure 4.5 LDV and PIV results at air flow rate is 0.7 kg/min (from Guildenbecher, 2009)...	59
Figure 4.6 LDV result at air flow rate is 0.7 kg/min (from Guildenbecher, 2009).....	59
Figure 4.7 LDV results for different mass flow ratio (from Guildenbecher, 2009)	60
Figure 4.8 Schematic of DIH for particle field measurement (from Gao, 2014).....	62
Figure 4.9 Traversing system on air flow system: [1] x-traverse, [2] z-traverse, [3] y-traverse, [4] droplet nozzle axial traverse, [5] droplet nozzle radial traverse. (from Guildenbecher, 2009)	63
Figure 4.10 Design of upper electrode.....	64
Figure 5.1 Shadowgraph of ethanol drop at We=20, U=0kV (a) start, (b) initiation, (c) deform, (d) finish.....	71
Figure 5.2 Shadowgraph of ethanol drop at We=20, U=0, 1 and 2 kV from left to right	72

Figure 5.3 Ethanol diameter PDF at $We=15$ (a) $Q=0$, (b) $Q=0.0142$, (c) $Q=0.0319$	74
Figure 5.4 Ethanol diameter PDF at $We=20$ (a) $Q=0$, (b) $Q=0.0142$, (c) $Q=0.0319$	75
Figure 5.5 Ethanol diameter PDF at $We=25$ (a) $Q=0$, (b) $Q=0.0142$, (c) $Q=0.0319$	76
Figure 5.6 Ethanol diameter PDF at $We=30$ (a) $Q=0$, (b) $Q=0.0142$, (c) $Q=0.0319$	77
Figure 5.7 Salt solution diameter PDF at $We=15$ (a) $Q=0$, (b) $Q=0.0119$, (c) $Q=0.0331$	79
Figure 5.8 Salt solution diameter PDF at $We=20$ (a) $Q=0$, (b) $Q=0.0119$, (c) $Q=0.0331$	80
Figure 5.9 Salt solution diameter PDF at $We=25$ (a) $Q=0$, (b) $Q=0.0119$, (c) $Q=0.0331$	81
Figure 5.10 Salt solution diameter PDF at $We=30$ (a) $Q=0$, (b) $Q=0.0119$, (c) $Q=0.0331$	82
Figure 5.11 Ethanol FWHM of fragment size	84
Figure 5.12 Salt solution FWHM of fragment size.....	84
Figure 5.13 Ethanol peak location of fragment size	85
Figure 5.14 Salt solution peak location of fragment size.....	86
Figure 5.15 Ethanol horizontal velocity PDF at $We=15$ (a) $Q=0$, (b) $Q=0.0142$, (c) $Q=0.0319$	88
Figure 5.16 Ethanol horizontal velocity PDF at $We=20$ (a) $Q=0$, (b) $Q=0.0142$, (c) $Q=0.0319$	89
Figure 5.17 Ethanol horizontal velocity PDF at $We=25$ (a) $Q=0$, (b) $Q=0.0142$, (c) $Q=0.0319$	90
Figure 5.18 Ethanol horizontal velocity PDF at $We=30$ (a) $Q=0$, (b) $Q=0.0142$, (c) $Q=0.0319$	91
Figure 5.19 Salt solution horizontal velocity PDF at $We=15$ (a) $Q=0$, (b) $Q=0.0119$, (c) $Q=0.0331$	93
Figure 5.20 Salt solution horizontal velocity PDF at $We=20$ (a) $Q=0$, (b) $Q=0.0119$, (c) $Q=0.0331$	94
Figure 5.21 Salt solution horizontal velocity PDF at $We=25$ (a) $Q=0$, (b) $Q=0.0119$, (c) $Q=0.0331$	95
Figure 5.22 Salt solution horizontal velocity PDF at $We=30$ (a) $Q=0$, (b) $Q=0.0119$, (c) $Q=0.0331$	96
Figure 5.23 Ethanol FWHM of fragment horizontal velocity	98
Figure 5.24 Salt solution FWHM of fragment horizontal velocity.....	98
Figure 5.25 Ethanol peak location of fragment horizontal velocity	99
Figure 5.26 Salt solution peak location of fragment horizontal velocity.....	100
Figure 5.27 Ethanol vertical velocity PDF at $We=15$ (a) $Q=0$, (b) $Q=0.0142$, (c) $Q=0.0319$	102
Figure 5.28 Ethanol vertical velocity PDF at $We=20$ (a) $Q=0$, (b) $Q=0.0142$, (c) $Q=0.0319$	103
Figure 5.29 Ethanol vertical velocity PDF at $We=25$ (a) $Q=0$, (b) $Q=0.0142$, (c) $Q=0.0319$	104
Figure 5.30 Ethanol vertical velocity PDF at $We=30$ (a) $Q=0$, (b) $Q=0.0142$, (c) $Q=0.0319$	105
Figure 5.31 Salt solution vertical velocity PDF at $We=15$ (a) $Q=0$, (b) $Q=0.0119$, (c) $Q=0.0331$	107
Figure 5.32 Salt solution vertical velocity PDF at $We=20$ (a) $Q=0$, (b) $Q=0.0119$, (c) $Q=0.0331$	108
Figure 5.33 Salt solution vertical velocity PDF at $We=25$ (a) $Q=0$, (b) $Q=0.0119$, (c) $Q=0.0331$	109
Figure 5.34 Salt solution vertical velocity PDF at $We=30$ (a) $Q=0$, (b) $Q=0.0119$, (c) $Q=0.0331$	110
Figure 5.35 Ethanol FWHM of fragment vertical velocity.....	112
Figure 5.36 Salt solution FWHM of fragment vertical velocity.....	112

Figure 5.37 Ethanol peak location of fragment vertical velocity.....	113
Figure 5.38 Salt solution peak location of fragment vertical velocity	114
Figure 5.39 Acceleration of particles on vertical direction.....	115

LIST OF SYMBOLS

a_A	droplet aerodynamic acceleration [m/s^2]
a_q	electrostatic acceleration [m/s^2]
C_D	drag coefficient
d_0	initial droplet diameter [μm]
d_{cro}	diameters of ellipse on long axis direction [μm]
d_{str}	diameters of ellipse on short axis direction [μm]
D_0	initial droplet diameter [μm]
D_{10}	arithmetic mean diameter [μm]
D_{10}	volume mean diameter [μm]
D_{32}	Sauter mean diameter [μm]
\tilde{D}	dimensionless logarithmic mean diameter
\bar{D}_{ln}	dimensionless logarithmic mean diameter
$f_0(D)$	fragment number probability distribution function
$f_3(D)$	fragment volume probability distribution function
F_A	aerodynamic force [N]
F_q	electrostatic force [N]
F_{surf}	net surface force [N]
$h(\xi, \eta)$	intensity of recorded hologram
k	electrostatic force constant [$\text{N} \cdot \text{m}^2/\text{C}^2$]
L	distance between two fragments [mm]
m_l	mass of liquid droplet [kg]
m_1	mass of the analyzed fragment [kg]
MMD	mass median diameter [μm]
$O(\xi, \eta)$	complex amplitudes of the object wave
$O^*(\xi, \eta)$	conjugate complex amplitudes of the object wave
Oh	Ohnesorge number
q	net charge [C]
q_1	charge of analyzed fragment [C]

q_2	charge of source fragment [C]
q_{Ra}	Rayleigh charge limit [C]
$q(t)$	total charge of the droplet [C]
Q	charge number
R	resistance [Ω]
$R(\xi, \eta)$	complex amplitudes of the reference wave
$R^*(\xi, \eta)$	conjugate complex amplitudes of the reference wave
Re	Reynolds number
Re_d	fragments Reynolds number
T_{ini}	initiate breakup time
U	applied potential [V]
U_0	air flow velocity [m/s]
V_x	horizontal velocity of fragments
V_y	vertical velocity of fragments
V_0	initial drop velocity [m/s]
V_{rel}	relative velocity of the droplet [m/s]
$V(t)$	voltage sensed by the tube [V]
$\bar{\tilde{V}}_x$	the mean of dimensionless horizontal velocity of fragments
$\bar{\tilde{V}}_y$	the mean of dimensionless vertical velocity of fragments
\tilde{V}_x	dimensionless horizontal velocity of fragments
\tilde{V}_y	dimensionless vertical velocity of fragments
We	Weber number
$We_{c\text{ Oh}\rightarrow 0}$	transitional Weber number at low Ohnesorge number
We_c	critical Weber number
$We_{D_{32}}$	Weber number based on Sauter mean diameter
We_e	electrostatic Weber number
δ	thickness of boundary layer [mm]
ε	density ratio
ε_0	vacuum permittivity [F/m]
κ_l	liquid dielectric constant

μ_a	air viscosity [Pa-s]
μ_l	liquid viscosity [Pa-s]
ρ_a	air density [kg/m ³]
ρ_l	liquid density [kg/m ³]
σ	surface tension [N/m]
σ_{e-}	electrical conductivity [1/ $\Omega \cdot m$]
σ_{ln}	logarithmic standard deviation
σ_s	standard deviation
ΔP_{e-}	local outward electrostatic stress [Pa]
ΔP_{σ}	local inward surface tension stress [Pa]

ABSTRACT

Author: Yang, Ze. MSAAE

Institution: Purdue University

Degree Received: May 2019

Title: Diameters and Velocities for Charged Liquid Drops Undergoing Aerodynamic Breakup

Committee Chair: Dr. Sally P.M. Bane, Dr. Paul E. Sojka

The sizes and velocities of fragments resulting from the aerodynamic breakup of charged drops are reported here. Measurements were made using digital inline holography (DIH). Highly and moderate conductive liquid droplets are used. Uncertainty of parameters is discussed. Finally, a discussion on the applied potential used for possible fragment charge-to-mass ratio charge is presented.

1. INTRODUCTION

The process of a bulk liquid transforming to numerous small fragments is called atomization and it plays a key role in many modern technologies. It has many applications, including fuel jets, fertilizer and pesticide atomizers, spray guns for painting or coating, and medical applications where it could be used during coating of pharmaceutical tablets and in nebulizers.

These applications perform the same fundamental task, which is to disperse a bulk fluid into a large number of small fragments. However, the difficulties in controlling the spray process bring significant challenges to the application and designing of those devices. For example, in combustion applications, various pollutants will form if the fuel drops are too large and thus are not completely combusted. On the other hand, in pharmaceutical applications, coating is wasted if the drops are so small that they are blown away with exhaust air. It is also similar in agricultural and painting applications that small drops should be avoided to prevent spray drift. Other applications require moderate drop sizes and avoidance of both small and large ones. The medical nebulizer is a good illustration, where drops must be small enough to reach alveoli, but cannot be so small that the drops remain airborne and leave the lungs when the patient exhales.

Besides with final drop size, other requirements such as spray dispersal, flow rate, drop transportation, etc. should also be considered by designers. To make a design that fulfills these needs, an exhaustive understanding of the atomization processes and mechanism is the first step to achieve. To this end, researchers have spent decades working in the atomization and sprays field.

To better assist investigations, atomization is divided into two regions: primary atomization and secondary atomization. In primary atomization region, liquid is

typically in the form of a sheet or jet and breaks up for the first time to produce drops. This process might be followed by secondary atomization where the droplets are affected by aerodynamic forces, causing them to deform and may break into fragments. In spray process, primary atomization always occurs at or near the nozzle exit and secondary atomization typically occurs further downstream. This thesis focuses on secondary atomization, especially secondary atomization of charged liquid drops.

1.1 Electrostatic Atomization

The study of electrostatic atomization could be traced back to 100 years ago and has been investigated by many distinguished scholars in history, such as Rayleigh (1882) and Taylor (1964, 1966). Their work has revealed a number of unique properties of electrosprays.

Electrosprays are typically characterized by very fine drops due to the additional disruptive force. Figure 1.1 gives an image of a commonly used electrostatic atomizer. Conductive liquid drops flow from a capillary tube needle. A grounded surface is located some distance from the tube. An electric field is formed when a voltage is applied and the value of electric field can be found using Maxwell's equations.

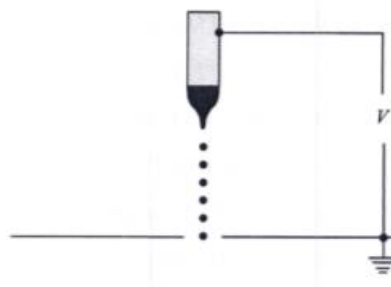


Figure 1.1 Basic electrostatic device (from Guildenbecher 2009)

At the liquid surface the electric field is balanced by a net surface charge. This gives rise to an outward electrostatic stress which acts against surface tension and may therefore increase the likelihood of atomization. Finally, as the liquid jet breaks up

into droplets, some of the surface charge remains resulting in droplets which are electrically charged.

Many variations on the setup shown in Figure 1.1 can be found in the literature and in applications of electrostatic atomization. Some involve multiple electrodes, non-contacting electrodes, time varying potentials, triodes, etc. Whatever the setup, the fundamental requirement for electrostatic-induced breakup is the presence of a strong electric field at the site of atomization.

Electrostatic forces can be made more significant by increasing the electric field. This is typically done by applying a larger potential. However, practical limits exist. At sufficiently high electric field strengths (potentials), the surrounding medium will become ionized and remove a portion of the charge in a process termed corona discharge. At still higher electric field strength, complete break-down of the surroundings may occur resulting in arcing between the electrode and ground.

The breakup of conductive liquids has been extensively studied and is typically classified into a number of modes based on the flow rate and applied voltage (Cloupeau and Prunet-Foch, 1994). At low liquid flow rates and a low level of charge, droplets form at the tip of the capillary and break off under the action of gravity. As the charge is increased, the sizes of the droplets decrease, and their frequency of formation increases. Interestingly, it is possible to form droplets which are significantly smaller than the nozzle diameter. This was termed micro-dripping by Cloupeau and Prunet-Foch (1994) and results from the fact that the electric field, and hence electrostatic stress, is highest where the radius of curvature is a minimum. Because the nozzle diameter can be increased without increasing the drop size, micro-dripping is advantageous in applications where clogging of the nozzle is a concern.

At higher levels of charge, the liquid cone depicted in Figure 1.1 will form a fine jet at its tip. This is referred to as the cone-jet mode. Using this mode it is possible to

produce fine drops spaced at regular intervals. Chen and Pui, (1997) measured drops at the order of $1\mu\text{m}$. If the diameter of the jet is known Neukermans (1973) showed that it is possible to estimate the diameter and frequency of the droplets using stability analyses which include electrostatic stresses. An in-depth discussion of this cone-jet mode is available in Cloupeau and Prunet-Foch (1994) and Cloupeau (1994).

At higher flow rates, the jet formed is approximately equal in diameter to the capillary. Depending on the level of electrostatic stress, breakup proceeds in a variety of modes. The above discussion has assumed the liquid is a good conductor (for which the rate of charge movement is sufficiently high). If this is not the case, then there is insufficient time for charge buildup at the surface. Attempts at increasing the total charge by applying higher potentials can result in corona discharge. As a result, the method shown in Figure 1.1 may not effectively atomize non-conductive liquids.

Techniques to charge non-conductive liquids typically rely on the phenomena of electron emission. An electrode with a fine tip is placed in the liquid. A negative potential is applied to the electrode such that the electric field at the needle tip is sufficiently high to cause transfer of electrons into the liquid.

The foregoing discussion serves as a very brief introduction to the topic of electrostatic atomization. Many more details can be found in a number of books written on the subject (Crowley, 1986; Bailey, 1988; Lefebvre, 1989; Michelson, 1990; Chang et al., 1995; Castellanos, 1998).

Here some of the applications of electrostatic atomization are discussed. This is intended to highlight key issues and motivate the work discussed later. It is by no means a comprehensive review.

Perhaps the most widely known use of electrostatic atomization is in the painting and coating industries. Here, the goal is to create an even coat over all surfaces while at the same time minimizing the overspray that can lead to wasted material and pollution. Since electrostatic atomization produces very fine drops with a narrow distribution of sizes, it results in an even coat on the surface. In addition, when the part is conductive, image charge forces attract the paint to the surface. In fact, due to “warp around”, charged drops can actually coat surfaces that do not face the atomizer and can penetrate into small crevasses. All reduce the amount of paint required and increase the coverage on areas which may be difficult to access using more traditional air-blast or air-assist atomizers.

In a related application, a significant amount of effort has been devoted to the development of electrostatic agricultural sprays. Example can be found in: Bailey (1998), Chang et al. (1995), Law (2001), and Jahannama et al. (2005). Because many plants are at least partially conductive and grounded via their root system, electrostatics can be used to increase dispersion of herbicides and pesticides over plant surfaces while reducing overspray and corresponding environmental pollution. Often electrostatic forces alone are not enough to transport drops to the inner surfaces of thick foliage and a combination of electrostatic and pneumatic nozzles are required, as discussed in Chang et al. (1995).

Electrostatic sprays are also used in food processing. Typical applications include spraying solutions onto meat and fowl, as well as onto harvested fruit (Law, 2001). The electrical conductivity of the meat and fowl make them particularly amenable to electrostatic spraying, and the ability of charged drops to penetrate into small spaces ensures more complete coverage.

Recently, applications have been developed for applying solutions to the human body. These include sunscreens, sunless tanning products, soaps, lotions, disinfectants, antibiotics/antitoxins and even topical treatments to burn victims (Cooper and Law,

2003). Medical personnel also employ electrostatic atomization for hand and skin sanitation because of the ability of charged drops to penetrate into small spaces such as under cuticles and fingernails. They are currently used by cruise ships and airlines for exterminating viruses and can also be used for odor control.

In a related field, electrostatic sprays are used during decontamination of equipment and personnel that have been subjected to either biological or chemical agents. Their effectiveness in providing thorough coverage of complex shapes and minimizing waste makes them particularly advantageous.

Other applications of electrostatic sprays take advantage of the narrow drop size distribution. Early jet printers used either the micro-dripping or cone-jet mode to produce highly controlled streams of charged drops. Varying electric fields were used to deflect the drops onto the writing surface (Kamphoefner, 1972). More recently, similar atomizers have been used in analytical chemistry instruments, some of which see service in airport security portals. An example is DESI (desorption electro-spray ionization) mass spectrometry (MS) discussed in Venter et al. (2006). In this case, a reagent is electro-sprayed and directed at a sample surface. Drops strike the surface, after which they ionize and transport any target molecules (explosives, illicit drugs, etc.) from the surface to the mass spectrometer inlet.

Finally, electrostatic atomization has been intensively investigated for application to combustion processes. Small drop sizes can be produced using less energy than is generally required for other methods, such as air-blast, air-assist, or pressure-swirl. This decreased energy input without sacrificing combustion efficiency. In addition, self-dispersal of the spray results in improved pre-mixing. Nevertheless, electrostatic atomization has yet to be implemented on a wide scale in combustion applications. This is because of the significant modifications that would be required to current injector designs. Also, if the injection is not properly timed, charged drops may be attracted to the walls of the combustion chamber, significantly degrading combustion

efficiency (Shrimpton, 2003). Future demands for improved efficiency and reduced pollution may necessitate a revisit of electrostatic atomization in combustion applications.

With increased proliferation of electrostatic sprays, a thorough understanding of the underlying atomization processes is becoming ever more important. As introduced above, the primary atomization of an electrostatically charged liquid has been exhaustively studied. However, despite the fact that aerodynamic forces are significant in many of the above applications, very little has been published on the secondary atomization of charged drops.

1.2 Scope

This thesis focuses on the secondary atomization of electrostatically charged drops. The goal is to find the size and velocity probability distribution function of charged fragments. Though it also focuses on the charged droplet breakup, it still differs from former researches like the breakup of charged jets and sheets conducted by Cloupeau and Prunet-Foch (1990), as well as Rayleigh (1882), which explored the spontaneous breakup of a stationary drop charged above a critical limit. De Juan (1996) studied charge and size distributions of electrospray drops but mainly on primary atomization. In contrast, this thesis is an extension of Guildenbecher (2009) who focused on breakup morphology and time of charged droplet.

This work is restricted to Newtonian liquids. While non-Newtonian liquids are used in many important applications, a thorough understanding of Newtonian liquid condition is first desired before involving shear-thinning, shear-thickening, and elasticity which make study more complicated. Studies on secondary atomization of charged non-Newtonian drops may come in the future.

For a more concise description, the term “breakup” will be widely used in the remaining parts of this work, and it is interchangeable with “secondary atomization” or “secondary breakup” since they all refer to the secondary atomization of drops due to aerodynamic forces.

1.3 Thesis Organization

Though secondary atomization was widely studied, few efforts were directed at the secondary atomization of charged drops. Focusing on the atomization of Newtonian liquid, this work starts with a literature review addressing the secondary breakup of uncharged droplets. A brief discussion on charged drops follows that. Once all the previous literature has been assessed, a theoretical analysis for the secondary atomization of charged drops is presented. Then, an experimental investigation to determine the size and velocity distribution of charged fragments is presented. The experimental setup will be discussed in detail followed by an in-depth consideration of the results. This thesis concludes with a summary of findings and suggestions for future work.

2. LITERATURE REVIEW

Researches of secondary atomization could be found in many literatures. The first comprehensive review was provided by Pilch et al. (1987). Gelfand (1996) and Guildenbecher (2009) also did review after that. A short review based on these works would be presented below including some new findings after their review.

Besides with experimental researches, some numerical investigation would be included for supplement. And the effect of parameters other than commonly used Weber number and Ohnesorge number are included. Some revisions for the past hypotheses are also contained especially for the charged drops.

This review includes published articles and dissertations on the secondary breakup field. Conference papers and other sources with important conclusions also are contained.

The work shown here is limited to secondary atomization where gas was used as continuous phase. It starts with introducing four experimental methods used for droplet breakup research. Then, the breakup processes occurring during secondary breakup are introduced and discussed in detail, followed by an analysis of influencing parameters such as Weber number, Ohnesorge number etc., on secondary breakup. Furthermore, the diameter and velocity distribution of uncharged droplets will be discussed. Finally, a brief introduction of past research on charged droplet breakup will be provided and followed by a short summary.

2.1 Experimental methods on secondary breakup

In the past, experiments were main approaches used on the investigations for secondary breakup. Researchers came up with plenty of novel ideas. Among them, three methods are most commonly used, which are (1) shock tubes, (2) continuous jets, and (3) drop towers. The aerodynamic condition of the droplet varied in different setups. Shock tube makes relative velocity altered uniformly in the space. Continuous jet gives a shearing effect. Drop tower offers a gradual change. Due to these differences, the observed drop behavior would be varied.

2.1.1 Shock Tube

This method mainly uses the flow after the shock to make a drop break up. A sketch of a shock tube is shown in Figure 2.1. The tube is divided into driver and driven two sections by diaphragm. A shock wave is formed by pressurizing the gas and so it flows through the tube. Drops are inserted into driven section where they break up.

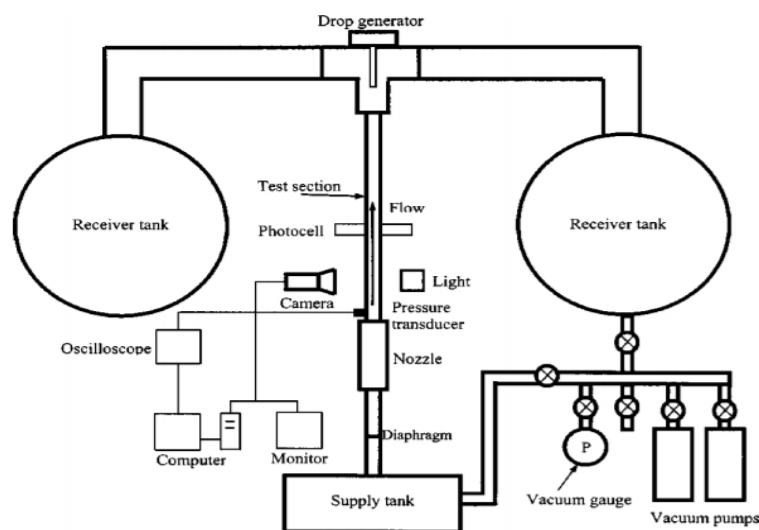


Figure 2.1 Shock tube experimental apparatus (from Theofanous, 2004)

The advantage of this method is that drop breakup occurs in an environment where changes over drop surfaces are uniform. However, the low data rate and high cost to make shocks weaken the feasibility of this method.

Dated back to Hinze (1995), many studies based on this method have been performed, including Ranger and Nicholls (1969), Gelfand et al. (1973), Chou and Faeth (1998), Joseph et al. (2002), and Theofanous et al. (2004).

2.1.2 Continuous Jet

This method allows continuous experiments without reset. Drops are formed at generator fall and break in the flow field. Optical techniques like DIH are used to perform measurements. A sketch of a continuous jet apparatus is shown in Figure 2.2.

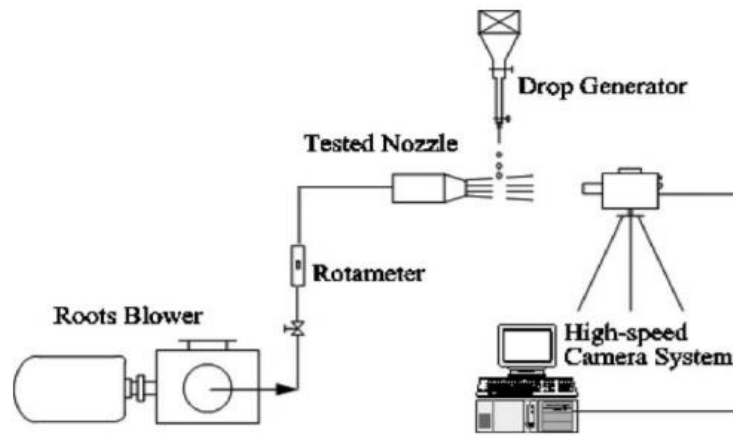


Figure 2.2 Continuous jet experimental apparatus (from Zhao 2007)

To make the results equivalent to the shock tube methods, boundary layers in the free jet should be minimized in case part of the drop breaks rather than the whole one when the relative drop velocity is relatively slow. Guildenbecher (2009) gave an expression for drop velocity V_0 and flow velocity U_0 as:

$$\frac{1+\delta/d_0}{T_{ini}\epsilon^{0.5}} < \frac{V_0}{U_0} < \sqrt{\frac{We_c}{We}} \quad (2.1)$$

Here δ is thickness of boundary layer, T_{ini} is initiate breakup time, d_0 is droplet diameter, ϵ is density ratio, We_c is critical Weber number. Experiments used this method could be dated back to Liu et al. (1993), Hwang et al. (1996) and Cao et al. (2007).

2.1.3 Drop Tower

In this method, secondary atomization is studied by having drops fall into a quiescent environment under gravity. A picture showing this setup is given in Figure 2.3.

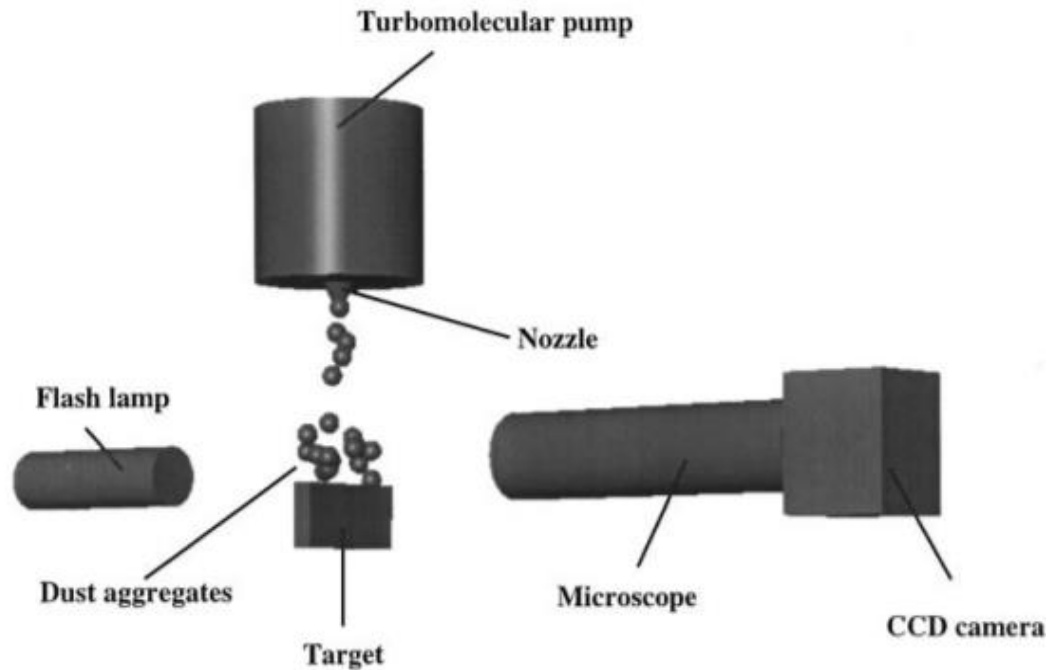


Figure 2.3 Drop tower experimental apparatus (from Jurgen, 2000)

This setup will not be discussed in detail since it was not widely used and has little relation to our experiment research.

2.1.4 Hybrid Method

Shraiber et al. (1996) used drops falling by gravity through various nozzles that make a non-uniform velocity profile. Schmelz and Walzel (2003) used drops falling through a shaped contraction to make ambient air accelerate during breakup. These methods show some similarity to methods mentioned before. The results of these studies, however, are different from those using former methods.

To briefly summarize, the continuous jet method is the most convenient and suitable one for charged drop breakup, since it allows various measurements using optical equipment and has high data rates.

2.2 Breakup Process Description

Though people used various methods to explore secondary atomization, the results usually show common morphology and similar characteristics. The breakup process starts with the droplet entering the flow field. It begins to deform due to the aerodynamic forces induced by the pressure difference between the front and back surfaces of the droplet. This deformation process is resisted by the surface tension and viscous forces which try to keep the droplet in the initial spherical shape. If the aerodynamic force, however, overcomes the resistance, the droplet will break into small fragments.

The surface tension and viscous forces can be relatively constant for a particular liquid with little temperature change. The flow field, therefore, dominates the fragmentation process. Different breakup modes occur when flow conditions change. For Newtonian liquid, usually five modes occur at different flow conditions. These modes are shown in Figure 2.4 and are called vibrational, bag, multimode, sheet-thinning and catastrophic breakup from top to bottom.

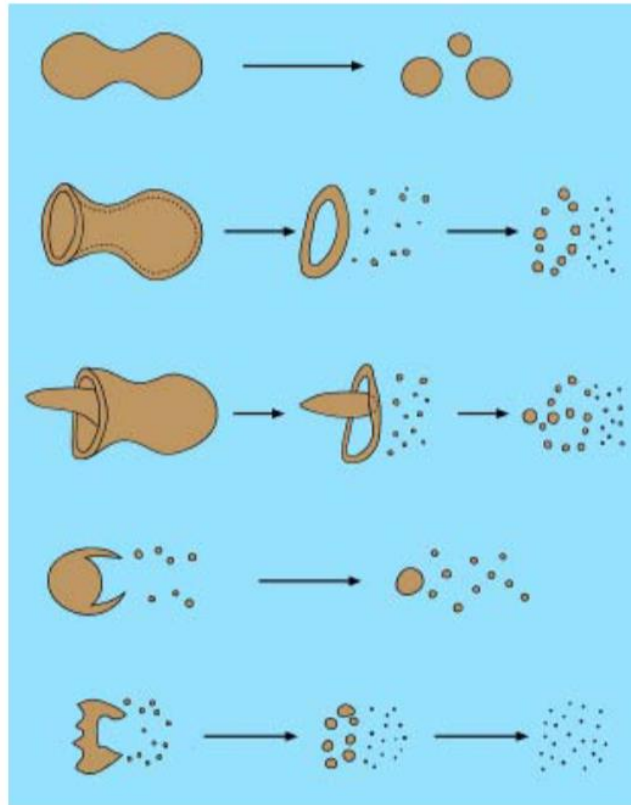


Figure 2.4 Breakup modes for Newtonian droplet (from Guildenbecher, 2007)

Usually, vibrational breakup cannot be observed. The droplet oscillates at low frequency and produces few fragments with comparable sizes to the parent droplet.

In bag breakup mode, the initial spherical droplet will deform to the shape like a thin hollow bag connected on a thick toroidal rim. The thin bag breaks into small fragments first usually starting at the tail of the bag. Disintegration then moves forward to the rim. The fragments produced by the thin bag always have smaller sizes but larger numbers than rim fragments.

Similar to bag mode, a thin hollow bag and thick rim appears in multimode breakup. But here a stamen attached to the bag oriented anti-parallel to the flow direction occurs, which makes this mode also called bag-and-stamen breakup. Though the droplet also starts to disintegrate from the bag, the fragment sizes have a wider range.

In sheet-thinning mode, plenty of small fragments are produced and removed from the parent drop. Numerous fragments are generated and, in some cases, a core with comparable size to parent droplet is maintained.

Finally, in the catastrophic mode, the surface of the droplet is corrugated by waves and fragments that are smaller than parent droplet is produced. These drops then further break into smaller fragments. Some researchers further subdivide this mode into wave-crest stripping and catastrophic modes.

Though this breakup morphology is widely used, some aberrations were observed. Theofanous *et al.* (2004) applied shock tube method to investigate the breakup processes in rarefied, supersonic flows. An apparently different morphology from the one conducted at subsonic experimental conditions was found. Further investigation is still needed.

2.3 Breakup Modes

2.3.1 Vibrational Breakup

Before a droplet breaks, the deformation that is mainly due to aerodynamic forces occurs first. But if the aerodynamic force is not strong enough, according to Hsiang and Faeth (1992), the surface tension may lead to the oscillation of drops in either stable or unstable ways depending on the flow. If it is unstable, the drop will break into fragments, which is referred as vibrational breakup. Different from other breakup modes, it will not produce final fragments as small as in other modes and its procedure is relatively slow.

2.3.2 Bag Breakup

This mode involves times and spatial dimensions at ms and μm scales, and experimental researches are relatively few. People like Han and Tryggvason (1999, 2001), Chou and Faeth (1998), Hwang et al. (1996) and Liu and Reitz (1997) made

contributions. Guildenbecher (2009) used experimental methods to further study this breakup mode.

This breakup mode requires higher droplet velocity than the vibrational mode, but lower velocities than other modes. The boundaries between this breakup mode and others, which could be described by a critical Weber number, We_C , are reported. For low Oh number ($Oh < 0.1$), it is widely accepted that We_C is roughly 11 for vibrational mode and 35 for sheet-thinning mode. A picture showing the breakup mechanism is given in Figure 2.5.

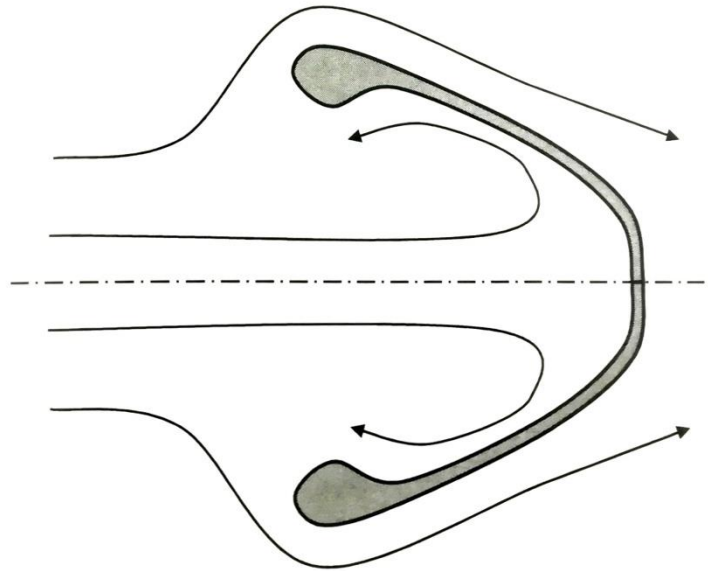


Figure 2.5 Bag breakup mechanism (from Guildenbecher, 2009)

As described in previous section, the whole process of bag breakup is given in Figure 2.6.

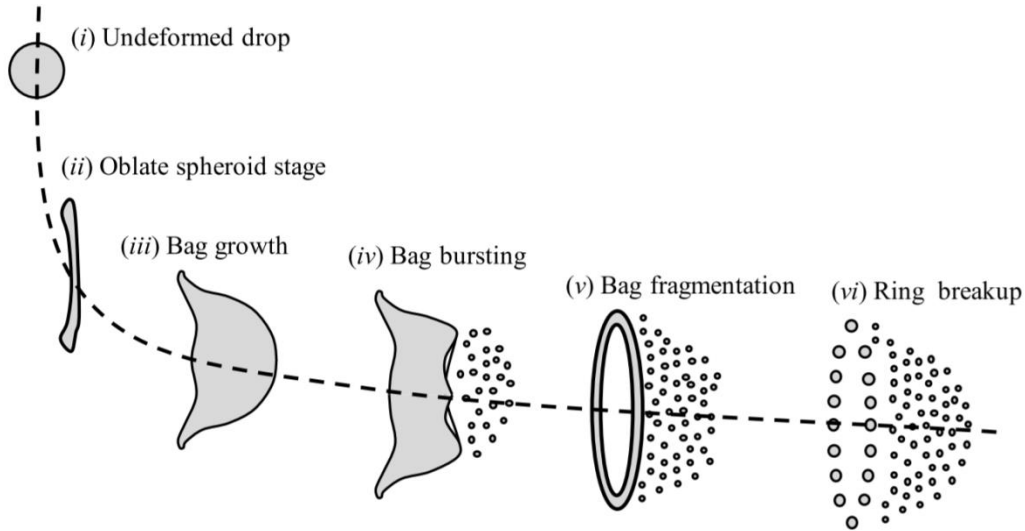


Figure 2.6 Bag breakup process (from Kulkarni, 2014)

2.3.3 Multimode Breakup

This mode is a transitional mode between bag and sheet-thinning modes. Different authors give it different names. Pilch et al. (1987) referred to it as bag-and-stamen mode. Cao et al. (2007) described it as dual-bag breakup mode. We here use multimode breakup mode, which is used by Hsiang and Faeth (1992). Dai and Faeth (2001) further subdivided this mode into two regions. When Weber number locates in the range from 18 to 40, it is called bag/plume breakup. When Weber number rise to the range from 40 to 80, the breakup is named as plume/shear breakup. Ohnesorge number for these two regions are still smaller than 0.1. Figure 2.7 shows the breakup mode of bag/plume which is observed by Dai and Faeth (2001).

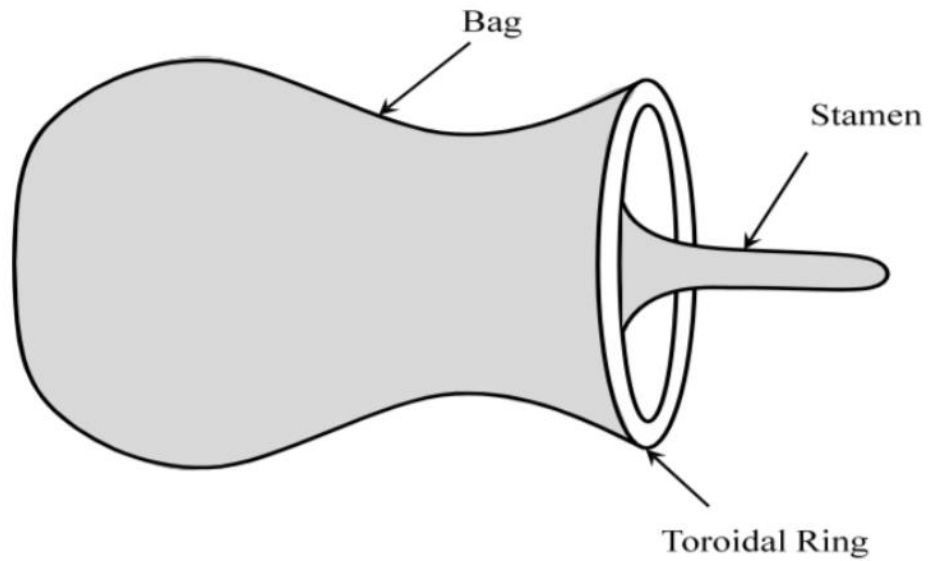


Figure 2.7 Bag/plume breakup mode (from Kulkarni, 2014)

To further understand the mechanism of this mode, Theofanous et al. (2004) used Rayleigh-Taylor instabilities to describe it. This theory showed good agreement with drops in rarefied, supersonic flow.

2.3.4 Sheet-thinning Breakup

In this breakup mode, ligaments are formed at the droplet perimeter and finally break into small fragments. Two controlling mechanisms were put forward. One was by Ranger and Nicholls (1969), named shear stripping, and the other was termed sheet-thinning by Liu and Reitz (1997). Sketches of these two mechanisms are shown in Figures 2.8 and 2.9.

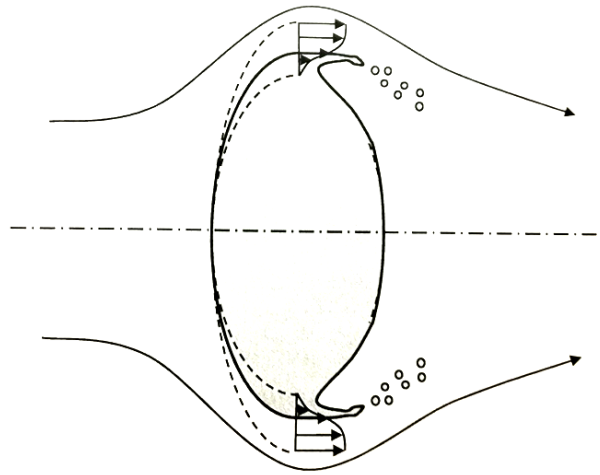


Figure 2.8 Shear stripping mechanism (from Guildenbecher, 2009)

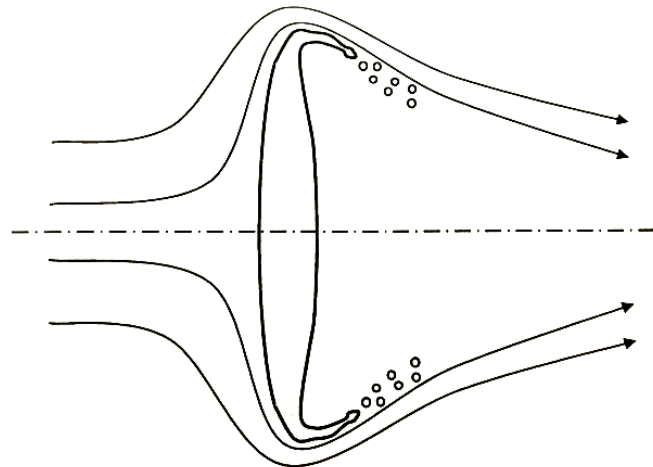


Figure 2.9 Sheet-thinning mechanism (from Guildenbecher, 2009)

The first figure indicates that the boundary layer formed inside the drop surface becomes unstable and results in stripping of mass, which leads to breakup of the droplet. Chou and Faeth (1997), Igra and Takayama (2001) and Igra et al. (2002) conducted shock tube experiments and the results from these experiments were considered to be the evidence of shear stripping mechanism. Liu and Reitz (1997) noticed the difference between experiments and models given by shear stripping mechanism. They then proposed the sheet-thinning mechanism, which shows sheet breaks into ligaments first and then to fragments. This mechanism is not only

supported by experiments from Liu and Reitz (1997) and Lee and Reitz (2000), but also by numerical investigations due to Khosla et al. (2006) and Wadhwa et al. (2007).

2.3.5 Catastrophic Breakup

This breakup mode is the least studied one. Faeth *et al.* (1995) did not give more details about velocities and drop sizes of this mode. This kind of breakup is dominated by the growth of unstable waves on the drop leading surface which makes it different from other modes. Wierzba and Takayama (1988) used holographic interferometry to study on this mode.

2.4 Dimensionless Parameters

From previous sections, flow field characteristics play important roles in the secondary atomization. Together with complicated multiple entities and complex surfaces, it makes analysis very challenging both mathematically and numerically. Therefore, researchers use a number of non-dimensional parameters to describe their findings. In secondary atomization the dimensionless parameters used are listed below in table 2.1. In the next part of this section, these parameters will be briefly discussed.

Table 2.1 Dimensionless parameters in secondary atomization

Weber number (We)	$We = \frac{\rho_a U_0^2 d_0}{\sigma}$
Ohnesorge number (Oh)	$Oh = \frac{\mu_l}{\sqrt{\rho_a \sigma d_0}}$
Reynolds number (Re)	$Re = \frac{\rho_a U_0 d_0}{\mu_l}$
Density ratio (ε)	$\varepsilon = \frac{\rho_l}{\rho_g}$

2.4.1 Weber Number

Numerous researches have shown that the transition between two modes mainly depends on We and Oh . For the most widely used and studied conditions, which is for Newtonian drops and $Oh < 0.1$, the values of transitional Weber number are listed in Table 2.2.

Table 2.2 Transitional Weber number for Newtonian droplets and $Oh < 0.1$

Vibrational	0~11
Bag	11~35
Multimode	35~80
Sheet-thinning	80~350
Catastrophic	>350

But to different researchers, the value might be different. Pilch et al. (1987) reported the transitional Weber number between multimode and sheet-thinning mode as $We=100$, whereas Hsiang and Faeth (1992) gave $We=80$ and Gelfand (1996) showed $We=40$.

2.4.2 Ohnesorge Number

Though classifying breakup modes by Weber number is widely used and valid for low Ohnesorge number ($Oh < 0.1$), it does not hold true for high Oh situations. Faeth et al (1995) mentioned in high-pressure spray conditions, Oh changed rapidly due to the decrease of surface tension and density ratio. Though breakup modes remain the same, transitional Weber number increases. Hsiang and Faeth (1995) gave the relation between transitional Weber number and Oh and the plot is shown in Figure 2.10.

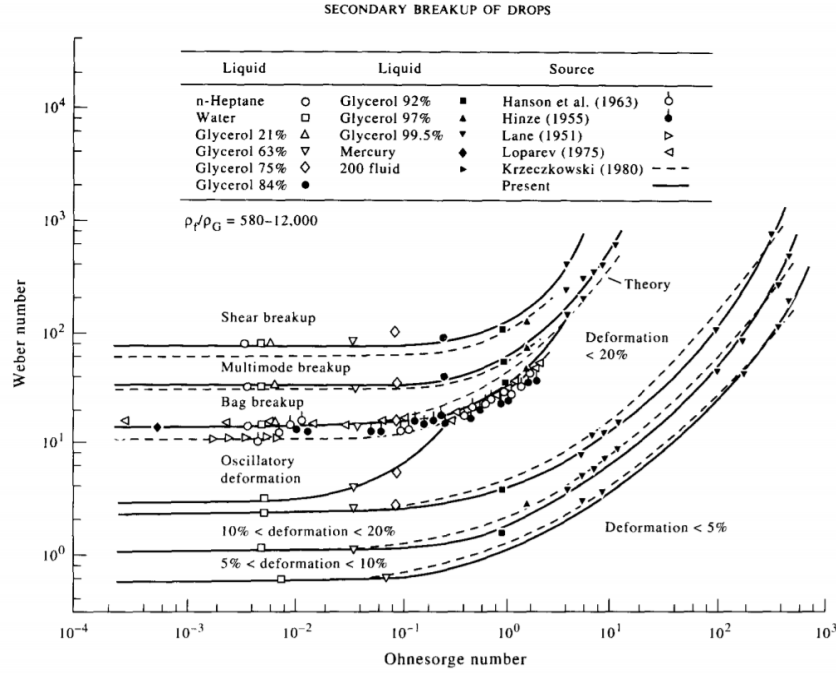


Figure 2.10 Relation between We_C and Oh (from Hsiang and Faeth, 1995)

Brodkey (1967) gave following expression to describe We_C and Pilch et al. (1987) confirmed for $Oh < 10$.

$$We_C = We_{C\,Oh \rightarrow 0}(1 + 1.077Oh^{1.6}) \quad (2.2)$$

Here $We_{C\,Oh \rightarrow 0}$ is transitional Weber number at low Oh which is shown in Table 2.2.

Kulkarni (2014) similarly gave an expression as:

$$We_C = We_{C\,Oh \rightarrow 0}(1 + 0.667Oh^2) \quad (2.3)$$

From Figure 2.10, huge difference could be observed at $Oh > 3$.

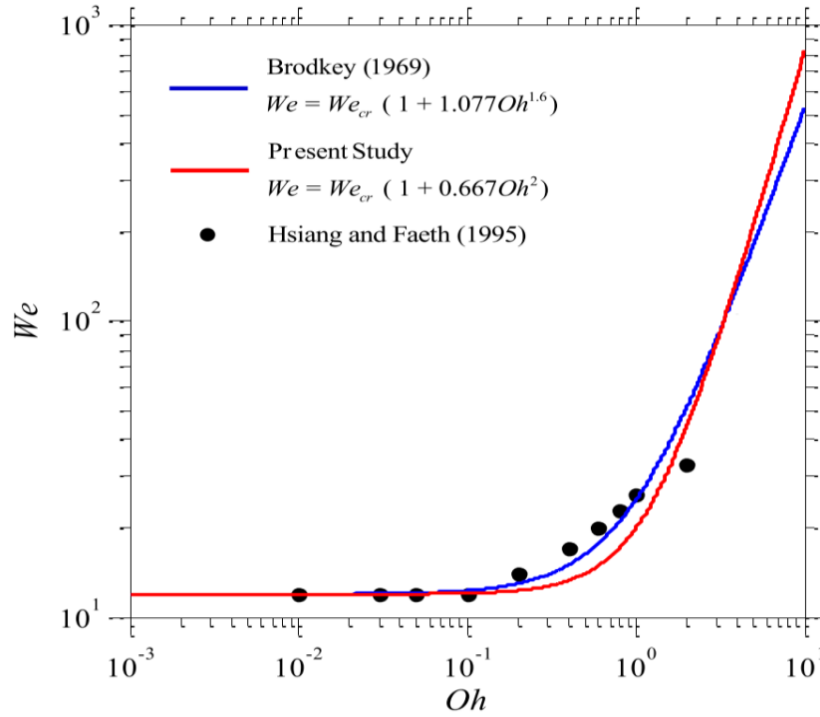


Figure 2.11 We_c at different Oh from Brodkey and Kulkarni expressions (from Kulkarni, 2014)

Cohen (1994) further studied about this and provided a new relation as:

$$We_c = We_{c, Oh \rightarrow 0} (1 + C \cdot Oh) \quad (2.4)$$

Here C is between 1.0 and 1.8 and depends on the breakup modes. Aalburg et al. (2003) also gave that $Oh \propto We^{0.5}$ when $Oh \gg 1$ based on his study.

Though many expressions are given, no one is accurate enough when $Oh > 1$. Further study on this is still needed.

2.4.3 Reynolds Number

Aalburg et al. (2003) studied drop deformation at low Re conditions using a numerical method. When $Re < 200$, the critical Weber number, We_c , changed apparently, whereas little change occurred when $Re > 200$. For many secondary breakup cases, Re is over 1000 and shows little effect on the breakup morphology.

Hsiang and Faeth (1995) mentioned dependence of We_c on Re in liquid-liquid drop tower experiments. Han and Tryggvason (2001) studied the influence of Re using numerical methods. They simulated drop breakup at different Re and We conditions. Their work is shown in Figure 2.12. As Re grows, breakup occurs at lower We .

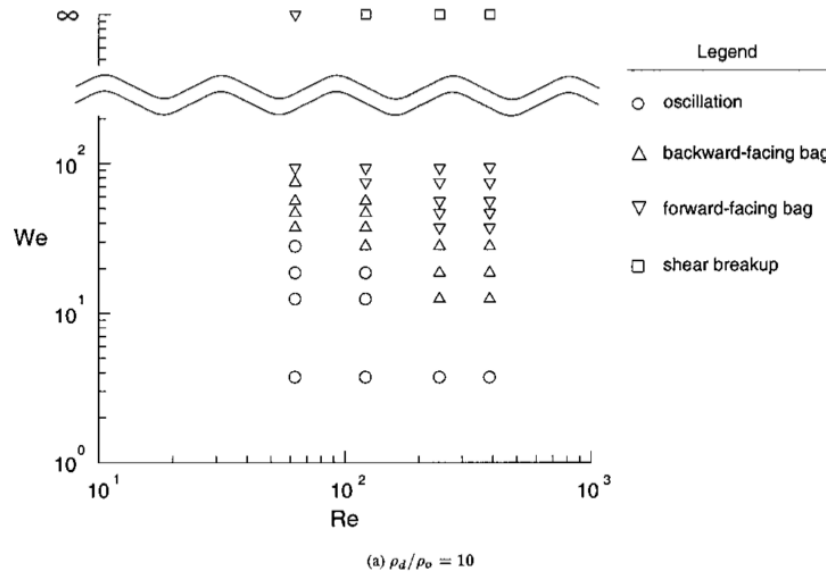


Figure 2.12 Simulation results for critical Weber number at different Reynolds number at density ratio of 10 (from Han and Tryggvason, 2001)

2.4.4 Density Ratio

Jain et al. (2018) studied the effects of density ratio also numerically. The result is shown in Figure 2.13, where we see that the drop tends to break at lower Weber numbers if density ratio goes up. This is similar to the tendency of the effect of Reynolds number. Furthermore, with the drop at $We=20$ and the density ratio=10, it did not break up. This is consistent with the result from Han and Tryggvason (2001).

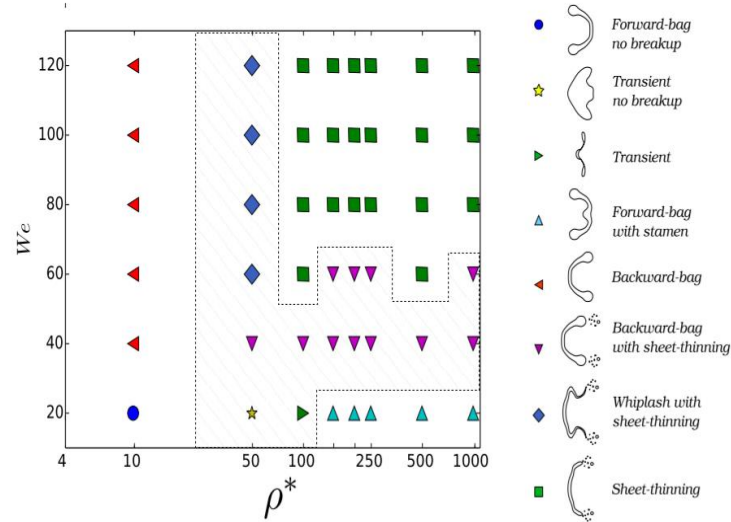


Figure 2.13 Breakup modes at different density ratio conditions (from Jain 2018)

2.5 Fragment Size and Velocity Distribution

Size distribution of fragments is one of the most important, but difficult to measure, properties in secondary breakup. In the past, techniques to measure fragment sizes are confined by their precision. Among those available methods, the rapid solidification of the fragments is a viable choice together with holography. However, both methods are hard to set, hard to analyze, and time consuming. Many optical drop size measuring methods, such as PDA, were developed to provide more rapid and precise measurements. Nevertheless, these techniques require a continuous process and are hard to achieve in shock tube method due to their relatively small testing region.

Drop size distributions are often described using two or more characteristic diameters. A representative diameter is expressed as:

$$D_{pq} = \left[\frac{\int_0^\infty D^p f_0(D) dD}{\int_0^\infty D^q f_0(D) dD} \right]^{\frac{1}{p-q}} \quad (2.5)$$

Here p and q are positive integers and $f_0(D)$ is the number probability distribution function (abbreviated as PDF in next chapters). Commonly used diameters in

researches are the arithmetic mean diameter, D_{10} , the volume mean diameter, D_{30} , and the Sauter mean diameter, D_{32} .

Simmons (1977) used plenty of aircraft and industrial gas turbine nozzles to study the size distribution of drops. In these places, secondary atomization played an important role to affect the size distribution of spray particles. The mass median diameter (abbreviated as MMD) and D_{32} of fragment were related by $\frac{\text{MMD}}{D_{32}} \approx 1.2$. Furthermore, either MMD or D_{32} could be used to estimate the fragment volume PDF, $f_3(D)$, using root normal distribution. Finally, Simmons (1977) found the maximum size of fragment is roughly three times of MMD.

Following Simmons (1977), Hsiang and Faeth (1992, 1993) used holography to measure drop size distributions at low Oh. In both bag and multimode region, the root normal distribution together with $\frac{\text{MMD}}{D_{32}} \approx 1.2$ proposed by Simmons (1977) was found to fit the data reasonably well.

Hsiang and Faeth (1992) conducted an analysis by taking the size of the drop phase boundary layer into consideration, which is thought to determine the size of the fragments in shear breakup. This gives:

$$\text{We}_{D_{32}} = C\varepsilon^{\frac{1}{4}}\text{Oh}^{\frac{1}{2}}\text{We}^{\frac{3}{4}} \quad (2.6)$$

$\text{We} < 1000$, $\text{Oh} < 0.1$, $580 < \varepsilon < 1000$

Here $\text{We}_{D_{32}} = \frac{\rho_a D_{32} U_0^2}{\sigma}$ and C is a constant of proportionality. Considering the parameters in the range mentioned above, Hsiang and Faeth (1992) applied $C=6.2$ and the D_{32} of fragments matched the values from Eq. (2.6) well. However, they pointed out that the range of density ratio was relatively narrow and needed further testing. Note that Eq. (2.6) was derived based on the assumption of shear breakup. Therefore, it does not fit well to bag and multimode breakup region.

Those size distributions mentioned above were mainly from the experimental methods. But many researchers hope to find out the size and velocity distributions of drops in theoretical ways. A possible method is the maximum entropy formulism (abbreviated as MEF). In this method, the fragment size and velocity distributions are required to fulfill certain conditions, such as spherical drops and conserved mass. The momentum and energy transferred to the drops from ambient phase need to be estimated. Thus, a PDF with minimum deviation was calculated. Babinsky and Sojka (2002) gave a full discussion on the development of the MEF and its applications to sprays. Li et al. (2005) pointed out the MEF could be applied to isolated systems in thermodynamic equilibrium. Unfortunately, not many sprays fulfill these prerequisites. To solve this, Li et al. (2005) came up with a new model with extra constraints to show the deviation level from the equilibrium assumption. This fitted experiment results better. And it helps to understand the reasons for inaccuracies when using the MEF. The size and velocity distributions of fragments could be correlated by applying the MEF method. But this does not mean the MEF can be regarded as a predictive method since *a priori* restraints are needed, unless part of restraints could be known in experiments or based on *ad hoc* assumptions.

2.6 Charged Droplets

The previous sections reviewed literature on the secondary atomization of uncharged, Newtonian liquid drops. Here, the few studies on the breakup of charged droplets are reviewed.

Experimental research on secondary atomization of charged drops is still rare, though people have been studying secondary atomization for quite a time. Some authors studied spray devices that employ both liquid electrostatic charging and a high-speed co-flow gas (Chang et al., 1995; Kim and Nakajima, 1999; Zhou and Cook, 2000). The secondary atomization of charged drops may occur in those experiments but did not draw much attention from the researchers. Kim and Nakajima (1999) found the

combination of spray charging and co-flow gas may allow independent control of droplet sizes and velocities. Such a capability would be useful in many spray applications.

Shrimpton and Laoonual (2006) showed for a charge spherical drop the net surface force, F_{surf} , becomes:

$$F_{\text{surf}} = 4\pi\sigma d_0 - \frac{q^2}{2\pi\epsilon_0 d_0^2} \quad (2.7)$$

Here q is net charge, σ is surface tension and d_0 is the droplet diameter. The permittivity of the surrounding fluid is approximated by the vacuum permittivity, ϵ_0 . The net surface force goes to zero when $q = q_{\text{Ra}}$, where q_{Ra} is the Rayleigh charge limit:

$$q_{\text{Ra}} = \sqrt{8\pi^2\sigma\epsilon_0 d_0^3} \quad (2.8)$$

Shrimpton and Laoonual (2006) came up with a new type of Weber number called electrostatic Weber number, We_{e-} , which was defined to explicate the effective reduction in surface tension:

$$We_{e-} = \frac{\rho_a U_0^2 d_0}{\sigma - \frac{q^2}{8\pi^2\epsilon_0 d_0^3}} \quad (2.9)$$

Shrimpton and Laoonual (2006) used the electrostatic Weber number in place of the traditional Weber number in their theoretical calculations of a charged diesel spray. However, this was disproved by Guildenbecher (2009) experimentally. Using a high-speed camera and shadowgraph imaging, Guildenbecher (2009) analyzed hundreds of videos and conclude that charge carried in a droplet plays a limited role in the secondary breakup of the charged drop.

From Figure 2.14, Guildenbecher (2009) found that charge would not affect breakup regimes obtained from original Weber number. Therefore, the modification of original Weber number is unnecessary and incorrect.

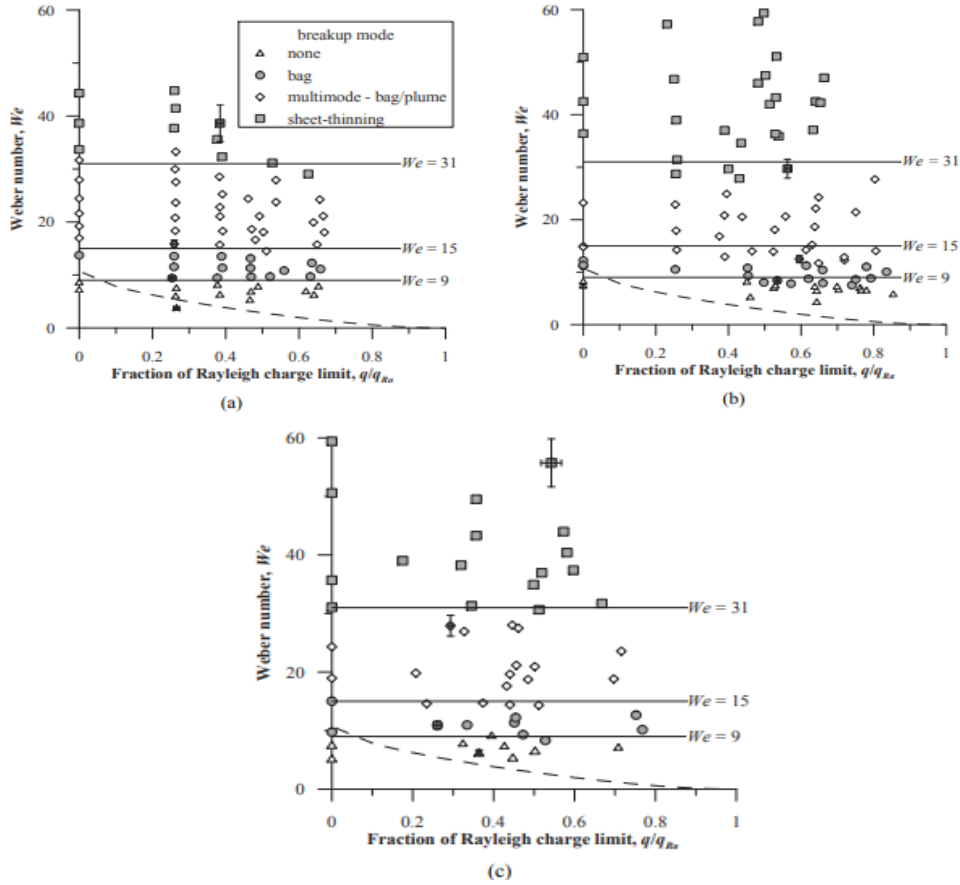


Figure 2.14 Charged drop fragmentation morphology for (a) conductive water/0.4% (w/v) salt solution, (b) moderately conductive ethanol and (c) weakly conductive hexane/5% (v/v) ethanol solution (from Guildenbecher 2009)

2.7 Summary and Conclusion

In this chapter, literatures focus on secondary atomization have been reviewed based on the comprehensive work by Pilch et al. (1987). The commonly used experimental apparatus were introduced. For uncharged Newtonian liquids, secondary breakup is characterized by a morphology containing vibrational, bag, multimode, sheet-thinning, and catastrophic modes. Each mode was briefly discussed. The breakup process has a strong relation to Weber number but relatively independent of other parameters such as Reynolds number, viscosity and density ratios when Ohnesorge number is low.

Although many correlations were put forward, most of them are empirical and might have huge difference between each other. Therefore, extrapolation beyond the scope

of experiments is of low confidence. To solve this problem, models based on the basic physical mechanism are required. The review of published papers shows the following conclusions. Bag breakup mode is observed at the lowest values of Weber number when secondary breakup occurred. And this is due to the pressure difference between the front stagnation point and the back. This makes the deformation in the center of the drop more rapidly than the peripheral area. Different from this mechanism, sheet-thinning mode appears at higher Weber number when the initial drop rapidly deforms to a disk with thin edges. Small fragments are generated from thin edges before the formation of the bag structure. When the Weber number locates in the intermediate range, multimode breakup is observed in which bag-and-stamen structure could be seen. Finally, when Weber number is extremely high, the fast-growing unstable surface waves will dominate the breakup mechanism. This breakup type is called catastrophic mode.

Furthermore, some parameters that might affect the secondary breakup were discussed. Although the Oh, Re and density ratio would affect the breakup in some extent, these influences are achieved by affecting the transitional We. That means We still play an important in the secondary atomization.

In addition to the above, this chapter highlights the lack of fundamental understanding of the effects of electrostatic charge on the breakup process. There is no information available on fragment sizes nor their velocities. Fragment charge-to-mass ratio is also of interest.

The following chapters of this thesis will discuss the secondary breakup of charged droplets in theoretical and experimental methods based on the research from Guildenbecher (2009). And results from conducted experiments based on setup in chapter 4 will be given in chapter 5.

3. ANALYSIS OF CHARGED DROPLET

This chapter begins with a discussion of the definition of non-dimensional parameter, charge number. Then it goes to the theoretical breakup model of different conductivity liquid drops. And finally, we combine theoretical analysis with experimental results to get the conclusion.

3.1 Definition of Charge Number

Table 2.1 defines the non-dimensional groups which compare the various physical forces that play a role in the secondary atomization of uncharged, Newtonian drops. As discussed above, charge results in an additional electrostatic stress so a new non-dimensional group is warranted.

To this end, the charge number, Q , is defined as:

$$Q = \frac{q^2}{8\pi^2\epsilon_0\sigma d_0^3} \quad (3.1)$$

Since the Rayleigh charge limit is defined as:

$$q_{Ra} = \sqrt{8\pi^2\epsilon_0\sigma d_0^3} \quad (3.2)$$

So, Eq. (3.2) could be also written as $Q = (\frac{q}{q_{Ra}})^2$. Drops must break apart when the charge number becomes 1, so when $Q=1$, breakup would occur regardless of the effect of aerodynamic or other additional forces.

Shrimpton and Laoonual (2006) put forth an electrostatic Weber number defined as:

$$We_{e-} = \frac{\rho_a U_0^2 d_0}{\sigma - \frac{q^2}{8\pi^2\epsilon_0 d_0^3}} \quad (3.3)$$

This suggests changes in charge level would affect the breakup morphology, but this was proved to be incorrect by Guildenbecher (2009). Therefore, the charge number

and standard Weber number will be used as separate non-dimensional parameters in the charged droplet breakup, rather than using the electrostatic Weber number.

3.2 Range of Applied High Potential

Kim and Turnbull (1976) studied droplet size and charge. They noticed that as the voltage increased, the diameter of the drop became smaller together with an increase in the frequency of droplet formation. When the potential was further increased, the formation of droplets would be more unstable.

In this experiment, similar phenomena were observed. As the voltage became higher than 3 kV, drops would occur in smaller sizes and at higher frequency. When the potential was further increased, the diameter of the drops would decrease, and evaporation would occur once the voltage was higher than 11 kV. To avoid too much difference in the size of drops, the applied potential was limited to the range of 0 to 2.0 kV. Several pairs of shadowgraphs were taken to confirm the diameters have little difference over this range of applied voltage.

3.3 Breakup Model of Charged Drop

Guildenbecher (2009) derived a model which compared the electrostatic stress to the surface tension stress over the surface of deformed drops. As the drop deforms, the ratio of the electrostatic stress to the surface tension stress is:

$$\frac{\Delta P_{e-}}{\Delta P_{\sigma}} = f(x, y, z) \quad (3.4)$$

Here ΔP_{e-} is the local outward electrostatic stress, ΔP_{σ} is the local inward surface tension stress. If the ratio is larger than 0, it means the electrostatic stress acts against the surface tension stress. If the ratio is larger than 1, the electrostatic stress overcomes the surface tension stress and the fluid would leave the drop.

The geometry is shown in Figure 3.1. An oblate spheroid is formed when an ellipse is rotated around z-axis. d_{cro} and d_{str} are diameters of ellipse on long axis and short axis directions respectively, which means $d_{cro} \geq d_{str}$.

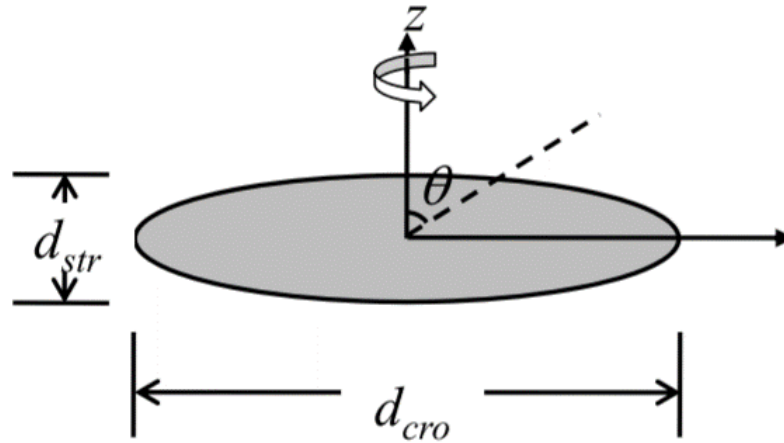


Figure 3.1 Geometry of deformed droplet in Cartesian coordinate (from Guildenbecher 2009)

To further simplify the problem, the oblate spheroidal coordinates developed by Moon and Spencer (1961) were introduced to replace the Cartesian coordinates. The geometry of the spheroidal coordinate is given in Figure 3.2.

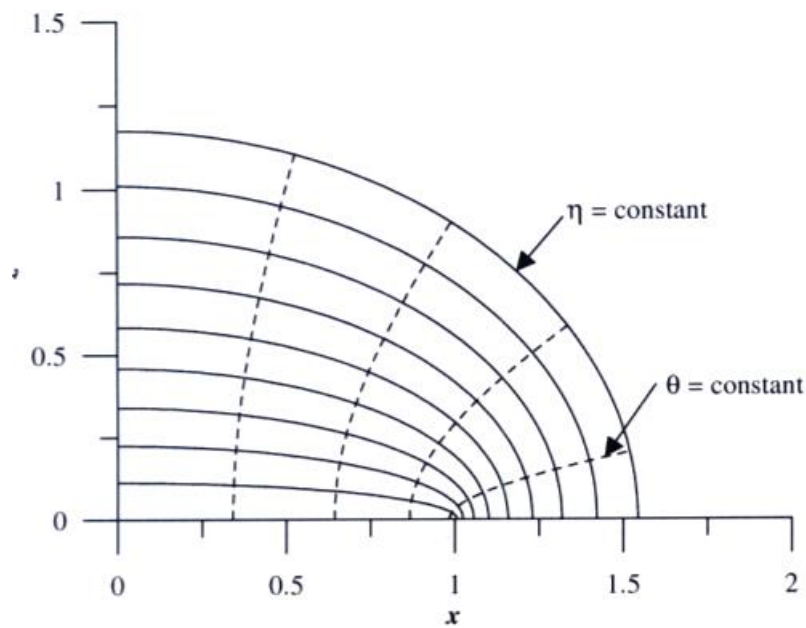


Figure 3.2 Geometry of deformed droplet in spheroidal coordinate (from Guildenbecher 2009)

And the transformation from Cartesian coordinate to spheriodal coordinate is:

$$x = b \cosh(\eta) \sin(\theta) \cos(\psi) \quad (3.5)$$

$$y = b \cosh(\eta) \sin(\theta) \sin(\psi) \quad (3.6)$$

$$z = b \sinh(\eta) \cos(\theta) \quad (3.7)$$

Here $0 \leq \eta < \infty$, $-\frac{\pi}{2} \leq \theta \leq \frac{\pi}{2}$, $0 \leq \psi < \infty$ and b is a constant.

With further derivation and simplification, Eq. (3.4) becomes:

$$\frac{\Delta P_{e-}}{\Delta P_{\sigma}} = Q \left(\frac{d_{cro}}{d_{str}} \right) \frac{2 \sqrt{\sin^2 \theta + \left(\frac{d_{cro}}{d_{str}} \right)^2 \cos^2 \theta}}{\sin^2 \theta + \left(\frac{d_{cro}}{d_{str}} \right)^2 \cos^2 \theta + \left(\frac{d_{cro}}{d_{str}} \right)^2} \quad (3.8)$$

A plot showing the relation between $\frac{\Delta P_{e-}}{\Delta P_{\sigma}}$, Q and $\frac{d_{cro}}{d_{str}}$ is given in Figure 3.3.

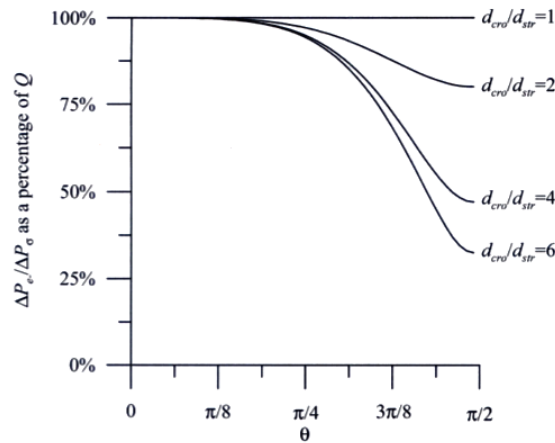


Figure 3.3 Stress ratio for perfect conducting liquid (from Guildenbecher 2009)

Since Q is always smaller than 1, $\frac{\Delta P_{e-}}{\Delta P_{\sigma}}$ will not be larger than 1 meaning the electrostatic charge gives little effect on the secondary breakup of an isolated drop.

For the liquid with lower conductive ability, a similar plot was developed and is shown in Figure 3.4. The above-mentioned model was confirmed with experimental results by Guildenbecher (2009).

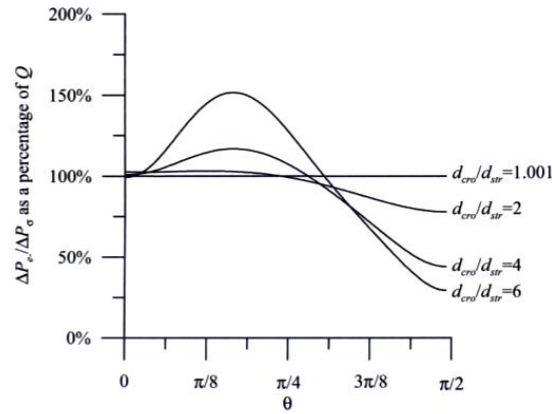


Figure 3.4 Stress ratio for moderate conducting liquid (from Guildenbecher 2009)

3.4 Force Analysis of Drop and Fragments

For the initial droplet in the flow field, two forces, which are aerodynamic drag and gravity, act on it.

The aerodynamic force is:

$$F_A = \frac{1}{2} \rho_a V_{rel}^2 \cdot C_D \cdot \frac{1}{4} \pi d_0^2 \quad (3.9)$$

Here ρ_a is the air density, V_{rel} the relative velocity of the droplet, C_D the drag coefficient and d_0 is droplet diameter.

The acceleration due to the aerodynamic force is:

$$a_A = \frac{F_A}{m_l} \quad (3.10)$$

Here m_l is the mass of liquid droplet.

For initial spherical droplet, C_D could be computed using Turton and Levenspiel (1986):

$$C_D = \left[0.352 + \sqrt{\left(0.124 + \frac{24}{Re} \right)} \right]^2 \quad (3.11)$$

$$Re < 2 \times 10^5$$

In the bag breakup case, C_D is about 0.47 and gives a_A the magnitude about 20 m/s^2 . The direction of the aerodynamic force is opposite to the direction of the relative velocity. Since the droplet falls from 15 mm above the flow field, the vertical velocity of the drop would be smaller than 0.1 m/s , which is much smaller than horizontal velocity which has a magnitude about 10 m/s . Therefore, the vertical component of a_A was neglected. At the same time, the droplet will accelerate quickly and then break apart into fragments.

As for fragments generated from the breakup, J. Zeleny (1915) results were used to estimate C_D :

$$C_D = \begin{cases} \frac{24}{Re_d} & \text{for } 0 < Re_d < 1 \\ \frac{24}{Re_d^{0.646}} & \text{for } 1 < Re_d < 400 \end{cases} \quad (3.12)$$

Further analyzing the generated fragments, C_D gives a value about 0.01. That means a_A is at the magnitude of 0.1 m/s^2 and will further decrease when the velocity rises. The horizontal velocity of fragments, therefore, tends to have little change.

Different from the uncharged situation, electrostatic repulsion exists between those fragments. So the electrostatic force between two charged fragments should be considered. It is written as:

$$F_q = k \frac{q_1 q_2}{L^2} \quad (3.13)$$

Here k is the electrostatic force constant, q_1 and q_2 are the charges of the analyzed fragment and source fragment respectively, and L is the distance between the two fragments. The acceleration induced by electrostatic force is:

$$a_q = \frac{F_q}{m_1} = k \frac{q_2}{L^2} \frac{q_1}{m_1} \quad (3.14)$$

Here m_1 is the mass of the analyzed fragment.

The charge to mass ratio $\frac{q_1}{m_1}$ is estimated using the Rayleigh charge limit:

$$\frac{q_1}{m_1} = \frac{12\sqrt{2}}{\rho_l} \sqrt{\frac{\epsilon_0 \sigma}{d_1^3}} \quad (3.15)$$

Here ρ_l is liquid density, ϵ_0 is vacuum permittivity, σ is surface tension, and d_1 is the diameter of the fragment. This equation gives the upper limit of the charge density for an isolated droplet and was confirmed by Gemci et al. (2002) experimentally.

The fragments produced by the bag are usually smaller than those produced by the rim during bag breakup mode. To find the effect of electrostatic force in the vertical and horizontal directions, the electrostatic acceleration was compared with gravity acceleration and the acceleration due to aerodynamic forces. The distance of two fragments should be larger than 6 mm if the electrostatic acceleration overcomes gravity acceleration and should be larger than 50 mm to exceed the aerodynamic acceleration. The values would be larger if the electrostatic field was induced by the fragment produced from the rim part.

From the analysis above, the breakup morphology and time should be different from the uncharged situation due to the strong electrostatic repulsion. But no apparent difference was observed from Guildenbecher (2009). That means the charge density of those fragments would be greatly smaller than the value calculated from Eq. (3.15). The size and velocity distribution of fragments in the charged breakup were little affected by the charge. The experiments and results to show this would be discussed in the next chapters.

3.5 Summary and Conclusions

A criterion to measure the charge level of a charged droplet was introduced and was used in the analysis of a theoretical model. These were confirmed to be correct by Guildenbecher (2009) using experiment results. To further explore the effect on the size and velocity of fragments, the force and movement of those fragments were analyzed. From the analyses above, it is reasonable for us to infer that those fragments carry the charge much less than Rayleigh charge limit and their size distribution and

movement would not be apparently affected by the carried charge. To further verify this assumption, experiments were conducted. The experiment setup and results would be discussed in detail in the next chapters.

4. EXPERIMENTAL APPARATUS

4.1 Material Properties

Before discussing the details of the setup, it is important to consider the properties of the fluids used. In this study, air is the ambient phase and it is at atmospheric pressure (1 bar) and room temperature (nominally 22°C).

The relevant properties are listed in Table 4.1.

Table 4.1 Relevant physical properties of air at 25°C and 1 bar

Density, ρ_a [kg/m ³]	1.18
Viscosity, μ_a [Pa-s]	1.83×10^{-5}

Two liquids were selected for the use. A water/salt solution was prepared with high conductivity. Neat ethyl-alcohol was also used to provide a lower but moderate conductivity. Relevant liquid material properties are listed in Table 4.2.

Table 4.2 Relevant physical properties of drop phase liquids

	99.6% Water -0.4% NaCl (v/v)	Ethly-alcohol
Density, ρ_l [kg/m ³]	995	788
Viscosity, μ_l [Pa-s]	8.93×10^{-4} ^a	1.08×10^{-3} ^c
Surface tension, σ [N/m]	0.0733	0.0244
Electrical conductivity, σ_e -[1/ $\Omega \cdot m$]	0.15	7.8×10^{-6}
Dielectric constant, κ_l	77.7 ^b	24.6 ^c

^a Fox and McDonald (1998), pure water at 25°C

^b Uematsu and Frank (1980)

^c Riddick and Bunger (1970)

4.2 Charged Droplet Production

A method to produce droplets with desired diameter is first required. Charging the drops to a measurable level is also needed. A design of nozzle to fulfill these

requirements is shown in Figure 4.1 (Guildenbecher, 2009). A stainless-steel tip (EFD Inc., internal diameter between 0.1 and 1.5 mm) is connected to an insulating nylon box in which a brass charging needle is inserted. Liquid enters the nylon box from the side and passes over the brass charging needle, and then exits through the syringe tip. The side of the nylon box is connected to a syringe pump (Harvard Apparatus Model 22) via nylon tubing.

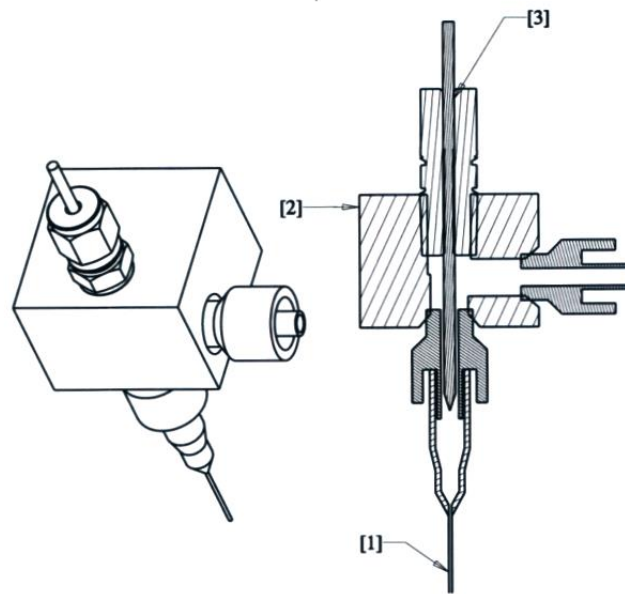


Figure 4.1 Droplet producing component: [1] syringe tip, [2] nylon body, [3] charging needle (from Guildenbecher 2009)

Similar to Zhang et al. (2006), drops are charged by a high potential applied to the needle by means of a high voltage power supply (Spellman High Voltage Electronics Corporation model SL30PN10). The power supply has a range from 0 to 30kV DC with a peak-to-peak ripple of less than 0.1%. Either positive or negative polarity could be applied on the needle. This nozzle charges conductive liquids by injecting a net charge into the liquid which collects at the nozzle tip.

Before entering the air jet flow field, the charge on each drop was measured using the detecting device similar to the system described by Gamero-Castanoa and Hurby (2002). It consists of a stainless-steel charge sensing tube (with a diameter of 10 mm)

covered with a larger co-axial Teflon tube. The combination was connected to an operational amplifier circuit specified for an ultralow input bias current (analog Devices AD549). The op-amp was grounded through a $10.06 \text{ M}\Omega$ resistor whose resistance was measured using a LCR meter (Stanford Research Systems Model SR 715) with an accuracy of $\pm 0.01 \text{ M}\Omega$. Voltage was recorded using a LabView® controller with a NI PCI-MIO-16E-4 DAQ card. To minimize background noise, the op-amp circuit was placed in a grounded metallic box and shielded co-axial cable was used.

As the drop enters the tube, an equal value charge but with opposite polarity is induced. Gamero-Castanoa and Hurby (2002) showed that if the response time of the detecting system is significantly smaller than the time for the drop to pass through the tube, the charge value on the drop could be calculated by integrating induced the current. The inverse process occurs as the drop leaves the tube. A sample result is shown in Figure 4.2.

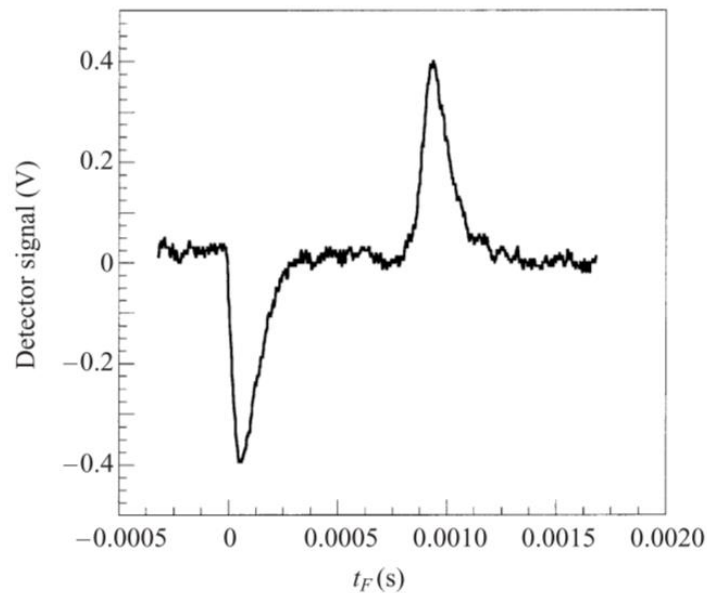


Figure 4.2 Sample detected voltage signal (from Gamero-Castanoa and Hurby 2002)

To calculate the total charge passing through the resistor, Gamero-Castanoa and Hurby (2002) gave a method using Ohm's law:

$$q(t) = \int_0^t \frac{V(t)}{R} dt \quad (4.1)$$

To examine the accuracy of the detecting system, A picoammeter (Keithley model 610BR) was used. As shown in Figure 4.3, charged droplets were collected in an isolated cup which was attached to the picoammeter. In all cases measurements agreed to within the accuracy of the picoammeter ($\pm 1 \times 10^{-11} \text{C}$).

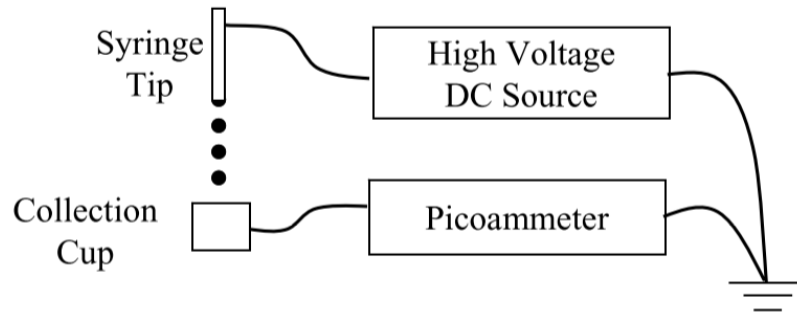


Figure 4.3 Scheme of examining system (from Guildenbecher, 2007)

Charged droplets then fell into the flow field produced by the air flow component discussed in the next section.

4.3 Air Jet Production

From the previous section, we know that three experimental methods are typically used to study droplet breakup: the shock tube method, the continuous jet method, the drop tower method. Each has its advantages and disadvantages. In this study the continuous jet method was selected since it best simulates the breakup conditions found in practice. Also, continuous jet can be operated in a way to reproduce shock tube results if certain requirements are satisfied.

Guildenbecher (2009) describes the jet production unit used in this experiment. Figure 4.4 is a schematic. The internal air flow pass through a 15 cm diameter cylindrical section followed by a converging nozzle designed to eliminate boundary layers. Flow leaves the nozzle through a 25.4mm diameter exit. The entire nozzle is made of

translucent acrylic, which is a very good electrical insulator to avoid interaction with the charged droplets.

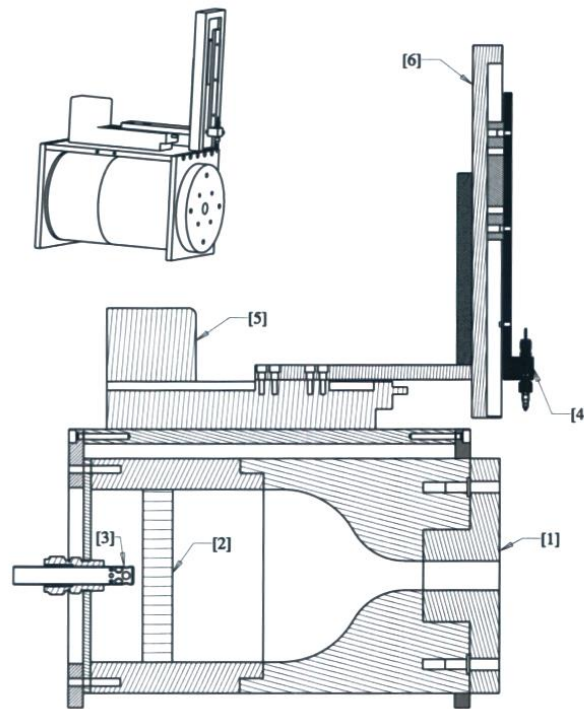


Figure 4.4 Scheme of air flow component: [1] nozzle body, [2] honeycomb and mesh, [3] radial input ports, [4] droplet nozzle, [5] droplet axial traverse, [6] droplet nozzle radial traverse. (from Guildenbecher, 2009)

Droplets enter the air jet vertically with the initial trajectory being approximately perpendicular to the centerline of the nozzle. To adjust drop injecting position along the flow axis direction, a traversing system was placed on the nozzle allowing for adjustment within the range of 0 to 80 mm from the exit plane. In addition, the initial falling position of the droplet from needle could also be adjusted from 0 to 300 mm using another traversing system.

The majority of previous results of breakup discussed in former chapters were conducted at steady, laminar air flow conditions. Therefore, precautions were taken to minimize velocity fluctuations and to maintain a flow field similar to other setups. Turbulence was reduced using Locherke and Nagib's (1972) methods.

Air enters the nozzle through radial ports. This improves flow uniformity throughout the rest of the nozzle. A honeycomb section was installed in the larger chamber (Plascore Inc. Polycarbonate Honeycomb 4mm cell diameter, 25.4 mm in length) to decrease large scale eddies and reduce radial air flow. A fine wire mesh (0.05 mm diameter, 0.07mm between wires) was placed after it to produce small scale, homogeneous turbulence which quickly dissipates and generates a steady, laminar flow field at the exit of nozzle.

Air flow is delivered to the nozzle using a piping system. A 19 mm diameter pipe is used to convey pressurized air up to 600 kPa. The air flow rate is controlled by a needle valve. A Coriolis flow meter (Micro Motion F-Series) was located between the valve and air nozzle. The flow meter could read the mass flow rate of gas within $\pm 0.1\%$ of the reported value.

When using this experimental setup to study secondary breakup, the properties of the flow field created by this air flow component should be well known. For example, flow mean velocity, the size of the boundary layer, and velocity fluctuation level are important characteristics that affect breakup.

To measure the velocity profile, Guildenbecher (2009) used both Particle Image Velocimetry (PIV) and Laser Doppler Velocimetry (LDV). Specific PIV and LDV results are given in his PhD dissertation and are shown in figures 4.5 to Figure 4.6.

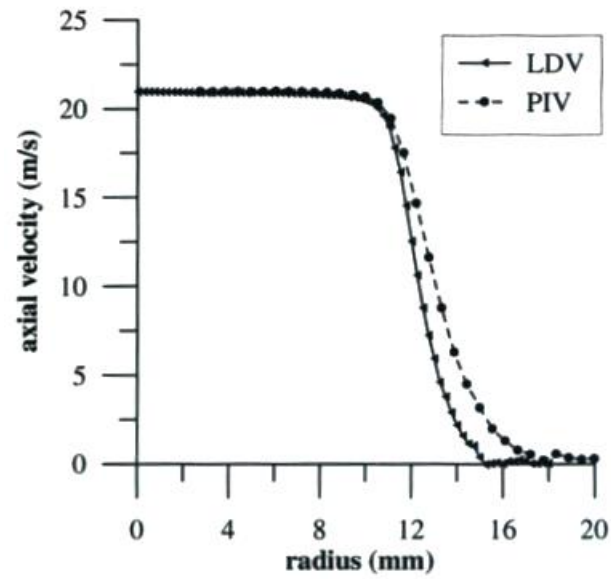


Figure 4.5 LDV and PIV results at air flow rate is 0.7 kg/min (from Guildenbecher, 2009)

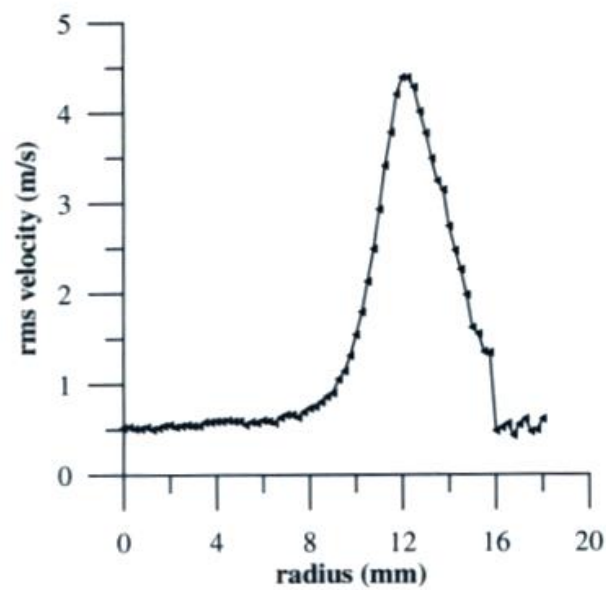


Figure 4.6 LDV result at air flow rate is 0.7 kg/min (from Guildenbecher, 2009)

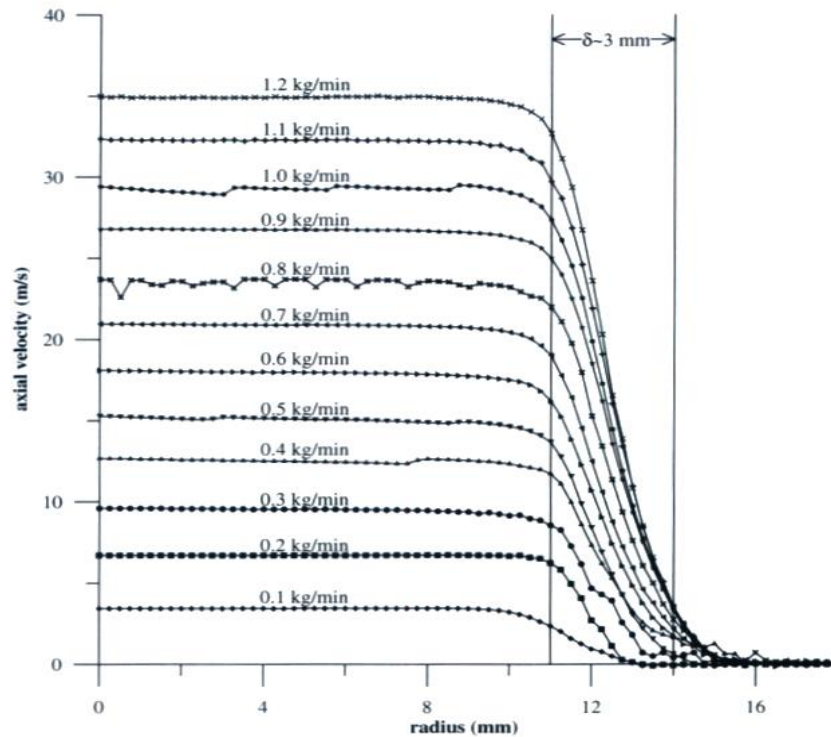


Figure 4.7 LDV results for different mass flow ratio (from Guildenbecher, 2009)

From Figure 4.5 and Figure 4.6, we see that PIV and LDV show agreement with each other and the fluctuation in axial velocity is small when the radius is small. From Figure 4.7, we see that for all flow rates, the velocity is nearly at small radii and that there is boundary layer with a thickness about 3mm occurs between radii of 11 and 14 mm.

4.4 High Speed Imaging System

4.4.1 Shadowgraph Imaging System

The shadowgraph imaging system consists of recording and illuminating parts. The recording part is a 60mm focal length lens (Nikon AF Micro Nikkor) attached to a high-speed digital camera (Fastcam SA-Z). The camera was oriented perpendicular to the air nozzle plane and focused on the centerline of the jet flow. Illumination was achieved using a 50W LED lamp. Using this arrangement movies of drop breakup were recorded at 20000 fps with a shutter time of $1\mu\text{s}$, effectively freezing the motion.

Uncertainty in the measured drop diameters is assumed to be dominated by the uncertainty in selecting the drop edge. The edge of the drop could only be accurately selected to within ± 1 pixel.

4.4.2 Digital In-line Holography (DIH) System

Holography was first introduced by Gabor and was promoted by the invention of the laser due to its high coherence. Gao (2014) gave a thorough discussion about holography. Recording and reconstruction are two important steps.

In the recording step, the interference pattern of the object wave and the reference wave is recorded as a hologram, which could be described mathematically by

$$h(\xi, \eta) = |O(\xi, \eta) + R(\xi, \eta)|^2 = |O|^2 + |R|^2 + OR^* + O^*R \quad (4.2)$$

Here, O and R are the complex amplitudes of the object wave and reference wave, and O^* and R^* are their complex conjugates.

In the reconstruction step, it can be regarded as the process of light illuminating from the hologram plane to the image plane. The complex amplitude at the hologram plane can be written as

$$h(\xi, \eta)R^*(\xi, \eta) = |O(\xi, \eta) + R(\xi, \eta)|^2 R^* = (|O|^2 + |R|^2)R^* + OR^{*2} + O^*|R|^2 \quad (4.3)$$

For the in-line configuration, the uniform plane wave can be expressed as $R(\xi, \eta) = 1$ and Eq. (4.3) simplified as

$$h(\xi, \eta)R(\xi, \eta) = (|O|^2 + 1) + O + O^* \quad (4.4)$$

This is solved using Fourier transforms.

In digital in-line holography, system is used to record movement of the particle field and recorded holograms are reconstructed using a computer. The whole scheme is shown in Figure 4.8.

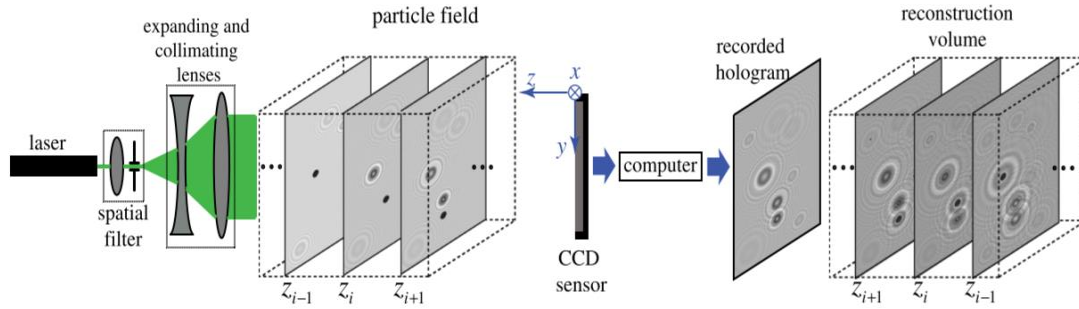


Figure 4.8 Schematic of DIH for particle field measurement (from Gao, 2014)

In this experiment, a 532 nm wavelength fiber laser with power 0.3 W is used. The laser beam is diverged after going through a spatial filter. The beam is further expanded through a concave lens and then becomes parallel light after passing through the collimating lens. The beam further propagates through the test section to illuminate the particle field, and finally reaches the camera. The object wave is formed by light reflection, diffraction and scattering by the small drops. And the undisturbed part of the beam from the same laser source is referred to as the reference wave. As those two waves propagate to the hologram plane, the interference pattern is recorded by the CCD sensor as holograms, $h(m,n)$. After the reconstruction using the computer, the particle field is acquired.

4.5 Traversing System

A traversing system was used to position the focus of sensitive measuring devices LDV, PIV, DIH etc. The acrylic air nozzle and the droplet producing nozzle were attached to a 3-axis traverse. Two additional traverses were used to control the axial and radial distance from air jet to the droplet nozzle. The whole system is shown in Figure 4.9.

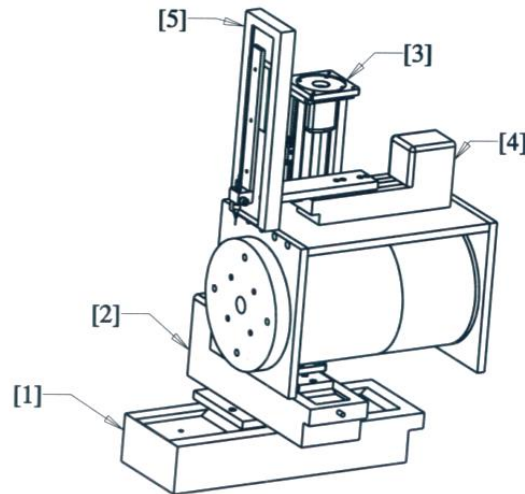


Figure 4.9 Traversing system on air flow system: [1] x-traverse, [2] z-traverse, [3] y-traverse, [4] droplet nozzle axial traverse, [5] droplet nozzle radial traverse. (from Guildenbecher, 2009)

The laser system used for DIH imaging system was also set on a 3-axis traverse to adjust illumination position. Both traversing systems could be easily controlled using software.

4.6 Fragment Charge Measuring Component

To determine the charge of each fragment, we applied two electrodes to generate a uniform electric field downstream in the flow field. By analyzing the movement and trajectory of individual fragments, we could calculate the acceleration of each of them.

The charge measuring component consists of two parts. Both parts are made of aluminum. The first part is the upper round electrode. As shown in Figure 4.10, its main body is about 25 mm thick with a diameter of 180 mm. A hollow cylinder with inner and outer diameters of 15 and 25 mm, respectively, with a height of 25 mm is attached to the main body in order to get the electrode charged using a clip. This electrode is supported on acrylic cuboidal arms.

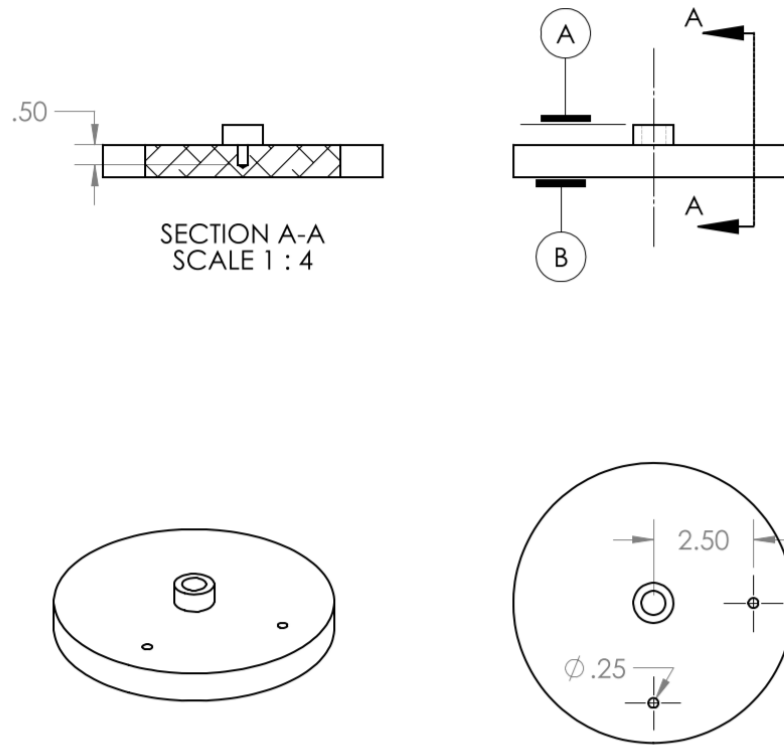


Figure 4.10 Design of upper electrode

The other part of the charge measuring device is the lower flat plate electrode. It is a $340 \times 300 \text{ mm}^2$ thin sheet. It was held by a stainless frame co-axially under the upper electrode to generate a uniform electrical field. The bottom surface of this sheet was covered with insulating tape and placed on an acrylic board to avoid leakage of electricity.

The two electrodes were charged by a DC power supply with a voltage range from 0 to 30V. In this work, a 20 V potential was applied on the electrodes, which have a spacing of 125 mm. This resulted in a uniform electric field with the intensity of 160 V/m.

4.7 Experiment Produce

This section describes how the whole experiment works based on individual components descriptions given in previous sections.

An experiment began with adjusting the traverse system to make the droplet drip from appropriate location so that it fell onto the centerline of the flow field. We next set the high voltage power supply to the desired level and adjusted the liquid flow so that droplets fell at the rate of about 0.2Hz. Next, we placed charge measuring component under the nozzle without contact and made sure each droplet falls through the measuring tube. Finally, the voltage pulses similar to the sample pulse shown in Figure 4.2 were observed from computer. Instead of letting drops fall into the flow field, a small metal plate was used to collect them. The initial setup was followed with the data recording procedure.

During data recording, the air valve was opened and adjusted to give the desired flow rate (We). When the flow became steady, the collecting plate was removed and droplets fell into the flow field. The holograms of the secondary atomization of charged droplets were recorded by the high-speed camera system.

The particle flow field was obtained by reconstructing the recorded holograms. After reconstruction, the diameter and spatial position of each detected particles were known. By correlating the particle positions in each consecutive frame, the velocity and acceleration of each particle could be computed. The vertical velocity component was directly related to the measured fragment charge and diameter, along with the known electric field.

4.8 Experimental Uncertainty

In this section, the associated uncertainty of some non-dimensional parameters and measured values are discussed. Based on the method of Klein and McClintock (1953), the propagation of measurement uncertainties is calculated.

4.8.1 Uncertainty in the Weber Number

The Weber number is defined as $We = \frac{\rho v^2 d}{\sigma}$. The uncertainty in Weber number is related to the uncertainty in ambient density u_ρ , relative velocity u_v , drop diameter u_{d_0} , and surface tension u_σ . The total uncertainty of Weber number could be expressed as:

$$u_{We} = \sqrt{\left(\frac{\partial We}{\partial \rho} u_\rho\right)^2 + \left(\frac{\partial We}{\partial v} u_v\right)^2 + \left(\frac{\partial We}{\partial d_0} u_{d_0}\right)^2 + \left(\frac{\partial We}{\partial \sigma} u_\sigma\right)^2} \quad (4.5)$$

Here

$$\frac{\partial We}{\partial \rho} = \frac{v^2 d_0}{\sigma} \quad (4.6)$$

$$\frac{\partial We}{\partial v} = \frac{2v d_0}{\sigma} \quad (4.7)$$

$$\frac{\partial We}{\partial d_0} = \frac{2\rho v d_0}{\sigma} \quad (4.8)$$

$$\frac{\partial We}{\partial \sigma} = \frac{-\rho v d_0}{\sigma^2} \quad (4.9)$$

Analysis for a typical result gives $\frac{u_{We}}{We} \approx 10\%$. The uncertainties in velocity and diameter contribute the most to the total uncertainty.

4.8.2 Uncertainty in the Charge Number

The charge number is defined as $Q = \frac{q^2}{8\pi^2 \epsilon_0 \sigma d_0^3}$. The uncertainty in charge number is related to the uncertainty in drop charge u_q , surface tension u_σ and drop diameter u_{d_0} .

The total uncertainty of charge number could be expressed as:

$$u_Q = \sqrt{\left(\frac{\partial Q}{\partial q} u_q\right)^2 + \left(\frac{\partial Q}{\partial \sigma} u_\sigma\right)^2 + \left(\frac{\partial Q}{\partial d_0} u_{d_0}\right)^2} \quad (4.10)$$

Here

$$\frac{\partial Q}{\partial q} = \frac{q}{4\pi^2 \epsilon_0 \sigma d_0^3} \quad (4.11)$$

$$\frac{\partial Q}{\partial \sigma} = \frac{-q^2}{8\pi^2 \epsilon_0 \sigma^2 d_0^3} \quad (4.12)$$

$$\frac{\partial Q}{\partial d_0} = \frac{-3q^2}{8\pi^2 \epsilon_0 \sigma d_0^4} \quad (4.13)$$

Analysis for a typical result shows $\frac{u_Q}{Q} \approx 10\%$. The uncertainties in charge and diameter contribute the most to the total uncertainty.

4.8.3 Uncertainty in the Minimal Detected Acceleration

The minimal velocity that could be effectively measure is $v_m = \frac{\Delta x}{\Delta t}$. Here Δx is the pixel size and Δt is the shutter time. So the minimal detected acceleration is $a_m = \frac{\Delta v_m}{\Delta t} = \frac{v_m}{\Delta t}$. For the camera used in this experiment, the typical value of a_m is 8000m/s². The total uncertainty on the minimal acceleration is:

$$u_{a_m} = \sqrt{\left(\frac{\partial a_m}{\partial \Delta t} u_{\Delta t}\right)^2 + \left(\frac{\partial a_m}{\partial v_m} u_{v_m}\right)^2} \quad (4.14)$$

Here:

$$\frac{\partial a_m}{\partial \Delta t} = \frac{-2v_m}{\Delta t^2} \quad (4.15)$$

$$\frac{\partial a_m}{\partial v_m} = \frac{1}{\Delta t} \quad (4.16)$$

$$u_{v_m} = \sqrt{\left(\frac{\partial v_m}{\partial \Delta t} u_{\Delta t}\right)^2 + \left(\frac{\partial v_m}{\partial \Delta x} u_{\Delta x}\right)^2} \quad (4.17)$$

$$\frac{\partial v_m}{\partial \Delta t} = \frac{-2\Delta x}{\Delta t^2} \quad (4.18)$$

$$\frac{\partial v_m}{\partial \Delta x} = \frac{1}{\Delta t} \quad (4.19)$$

Analysis of a typical result shows $\frac{u_{a_m}}{a_m} \approx 11\%$. The uncertainty in shutter time contributes the most.

4.8.4 Uncertainty in the Minimal Applied Potential

The gravitational acceleration, compared to the minimal detected acceleration, is much smaller and could be neglected. Thus, the applied electric field contributes more to the acceleration and should be larger than the minimal value based on the minimal acceleration. Therefore, the minimal potential would be:

$$U_m = \frac{a_m L_m}{q} \quad (4.20)$$

Here L is the gap between two electrodes. Since charge to mass ratio cannot be measured directly, this value is estimated using Rayleigh charge limit in Eq. (3.14).

The total uncertainty of minimal applied potential is expressed as:

$$u_U = \sqrt{\left(\frac{\partial U}{\partial a_m} u_{a_m}\right)^2 + \left(\frac{\partial U}{\partial L} u_L\right)^2 + \left(\frac{\partial U}{\partial \rho} u_\rho\right)^2 + \left(\frac{\partial U}{\partial d} u_d\right)^2 + \left(\frac{\partial U}{\partial \sigma} u_\sigma\right)^2} \quad (4.21)$$

Here:

$$\frac{\partial U}{\partial a_m} = \frac{\rho L}{12} \sqrt{\frac{d^3}{2\varepsilon_0 \sigma}} \quad (4.22)$$

$$\frac{\partial U}{\partial L} = \frac{a_m \rho}{12} \sqrt{\frac{d^3}{2\varepsilon_0 \sigma}} \quad (4.23)$$

$$\frac{\partial U}{\partial \rho} = \frac{a_m L}{12} \sqrt{\frac{d^3}{2\varepsilon_0 \sigma}} \quad (4.24)$$

$$\frac{\partial U}{\partial d} = \frac{a_m \rho L}{8} \sqrt{\frac{d}{2\varepsilon_0 \sigma}} \quad (4.25)$$

$$\frac{\partial U}{\partial \sigma} = \frac{-a_m \rho L}{24} \sqrt{\frac{d^3}{2\varepsilon_0 \sigma^3}} \quad (4.26)$$

Analysis of a typical result shows $\frac{u_U}{U} = 13\%$. Further discussion will be presented in chapter 5.

5. RESULTS

Using the experimental apparatus described in the former chapter, experiments were conducted, and results were collected with the liquid shown in the Table 4.2. The flow condition was limited to bag breakup range which is roughly from $We=11$ to 30. And at each aerodynamic condition, different potentials were applied to the droplet.

This chapter begins with a brief introduction of how to select and process the acquired data. Then, size and velocity distribution of the fragments produced by the breakup of the charged droplet will be discussed. Plots and fitting curves would be given in the figures. Finally, a summary and conclusions will be given at the end of this chapter.

5.1 Criteria for Data Processing and Selection

After collecting the holograms, the first step is to reconstruct the particle field. In this step, the information of the particle field, such as particle location, particle size and solidity etc. would be known. But in practice, the particle diameter is calculated based on the area of the detected particle which is assumed to be a sphere. If the fragment deforms apparently, the assumption is not valid which will give large error to the diameter. To verify the assumption, solidity value was taken into consideration. Ranged from 0 to 1, solidity is expressed as $\frac{d_{str}}{d_{cro}}$. If the value is closer to 1, it means the shape of the fragment is closer to a sphere. Therefore, to acquire higher accuracy, those fragments with solidity values lower than 0.9 were discarded.

In the bag breakup regime, the diameters of fragments range from about $40\mu m$ to $600\mu m$. Since the pixel size of the high-speed camera is $20\mu m$, some small fragments would take about 2×2 pixels. So the computer is not able to give accurate diameters of the small fragments due to the low resolution. To avoid the accuracy due to the resolution, the fragments with diameters lower than $60\mu m$ were be erased.

To further get the velocity of each fragment, correlation of particles in two consecutive frames are needed. After matching particles, the velocity could be calculated based on their movement. Similar to the former step, the fragments with smaller than $60\mu\text{m}$ or highly deformed were deleted first. Furthermore, not all particles could be perfectly detected in both consecutive frames. Some particles may appear in the first frame but not shown up in the second frame. The velocity of these particles usually appeared to be opposite to the flow direction with large values. To avoid this kind of error, these particles were removed.

To acquire higher accuracy, the best method is to process the holograms of each breakup frame by frame and correlate all the particles recorded in the holograms. However, each breakup process takes about 200 frames and several minutes are needed to process each frame. More time will be consumed to count the total number of fragments in each breakup. Comparing to this method, it was more efficient to process the hologram once per 60 frames based on the average velocity. And data were taken from the processed holograms. Multiple groups with same flow and charging conditions were taken and processed. Roughly thousands of fragments data were collected for a certain condition. Though some particles might be omitted or repeatedly counted, but the number of these is negligible compared to the sample base.

Based on the criteria mentioned above, data were processed and selected. The specific results are shown in the next sections.

5.2 Shadowgraph of Breakup Process

Since the region of bag breakup is narrow and vague, some small change in the air flow rate might lead the breakup process to the sheet-thinning mode. So shadowgraphs were taken to check the droplet breakup still in the bag regime when the drop was not charged. In addition, shadowgraph imaging provides more details to the breakup process of charged droplet. Some important information such as, the

whole breakup process, the geometry of liquid bag under different charging condition and distribution of fragments etc. could be known from the shadowgraphs.

Figure 5.1 shows the whole breakup process of an ethanol droplet under the condition of $We=20$, applied voltage $U=0kV$.

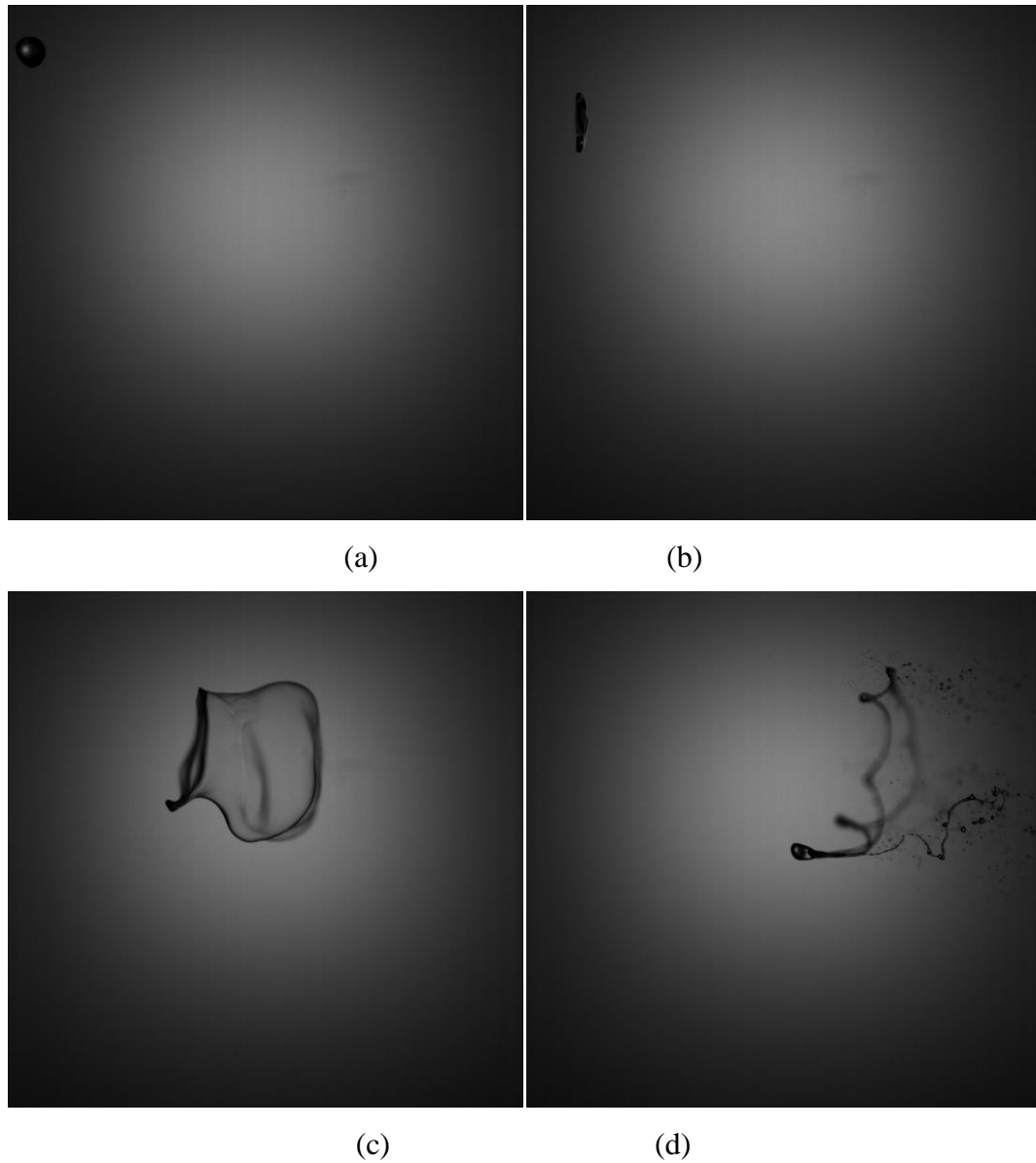


Figure 5.1 Shadowgraph of ethanol drop at $We=20$, $U=0kV$ (a) start, (b) initiation, (c) deform, (d) finish

As the applied voltage increase, the geometry of the bag changed a bit but still in the bag breakup region. Figure 5.2 shows the shape of bag when it is going to break apart at different charging potential.



Figure 5.2 Shadowgraph of ethanol drop at $We=20$, $U=0, 1$ and 2 kV from left to right

Apparently, from the shadowgraphs, no significant difference was found between different charging conditions. Although the size of bag changed, neither did new morphology appear, nor did the breakup mode shift to vibrational or multimode breakup. This is consistent with Guildenbecher (2009) showing charge did not give significant contribution to the breakup morphology.

5.3 Size Distribution of Charged Breakup Fragments

Within the bag breakup regime, experiments were conducted at Weber number is 15, 20, 25 and 30. Applied potential ranges from 0 to 2.0 kV. The correspondence between applied potential (U) and charge number (Q) is given in Table 5.1 and Table 5.2. DIH system was used to record the particle field of fragment after breakup.

Table 5.1 Correspondence between applied potential and charge number of ethanol

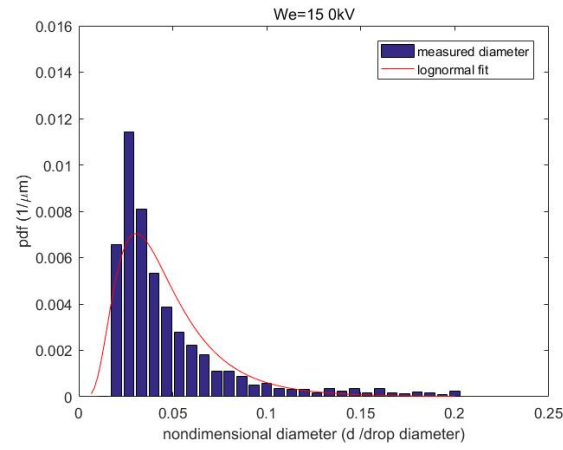
U (kV)	0	0.5	1.0	1.5	2.0
Q	0	8.86×10^{-4}	0.0142	0.0221	0.0319

Table 5.2 Correspondence between applied potential and charge number of salt solution

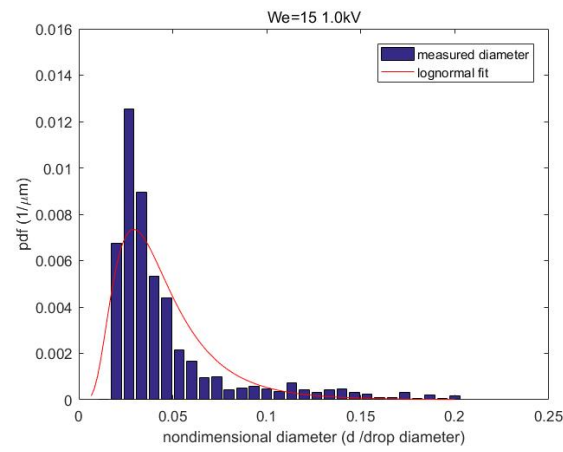
U (kV)	0	1.0	2.0
Q	0	0.0119	0.0331

After reconstructing the holograms, the number and diameter of fragments were known to us. The diameter PDF could be plotted using MATLAB. And the lognormal fitting curve was also plotted in the graph.

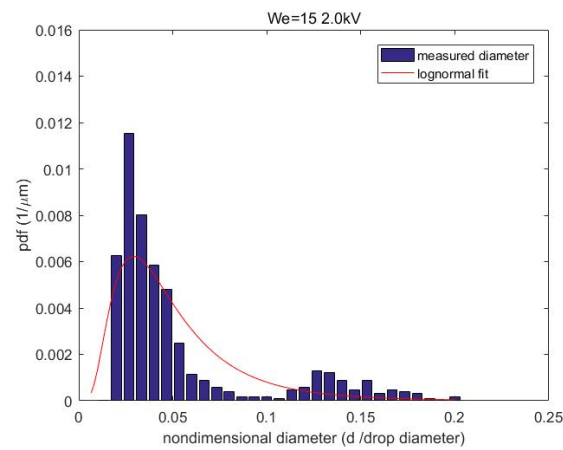
To begin with, ethanol results are given from Figure 5.3 to Figure 5.6. Probability distribution function was plotted in blue bars, and the lognormal fitting curve was plotted in red. Diameters were nondimensionalized by dividing the initial drop size.



(a)

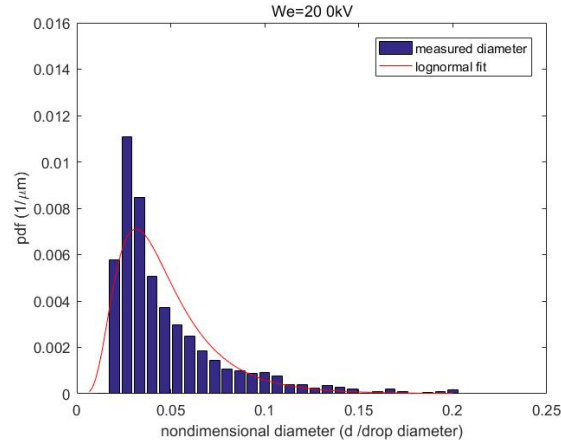


(b)

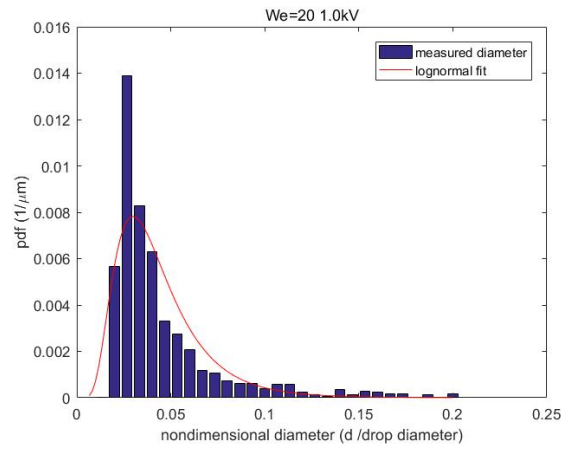


(c)

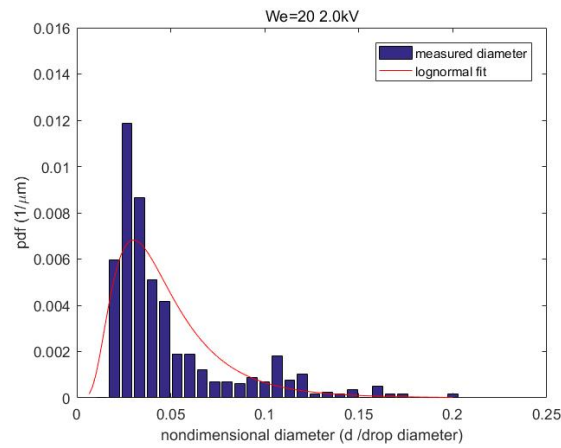
Figure 5.3 Ethanol diameter PDF at $We=15$ (a) $Q=0$, (b) $Q=0.0142$, (c) $Q=0.0319$



(a)

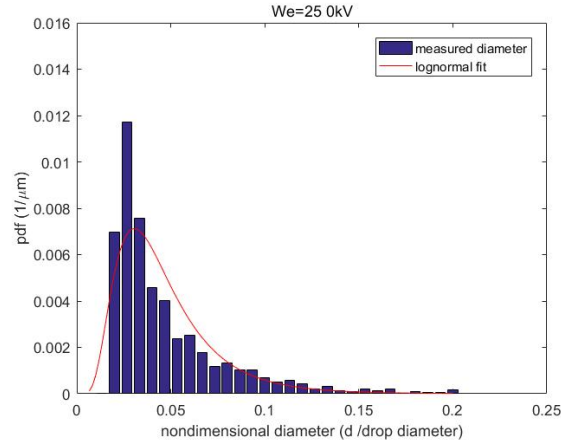


(b)

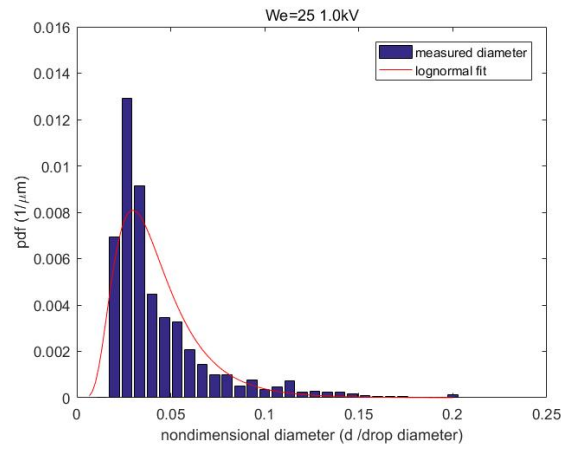


(c)

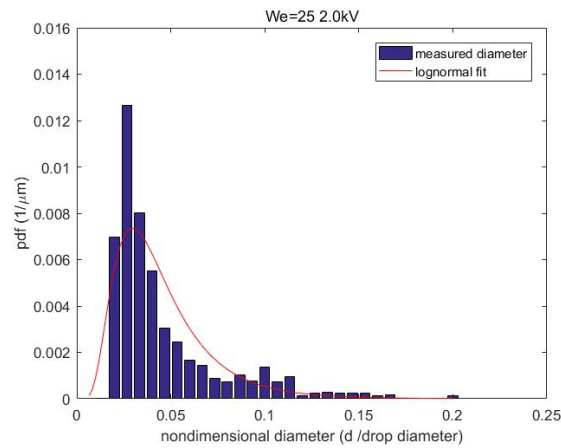
Figure 5.4 Ethanol diameter PDF at $We=20$ (a) $Q=0$, (b) $Q=0.0142$, (c) $Q=0.0319$



(a)

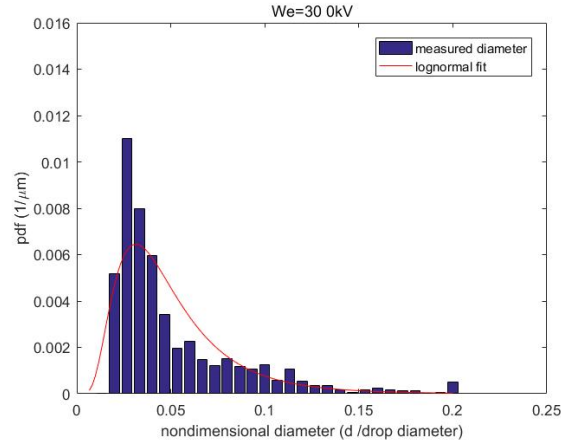


(b)

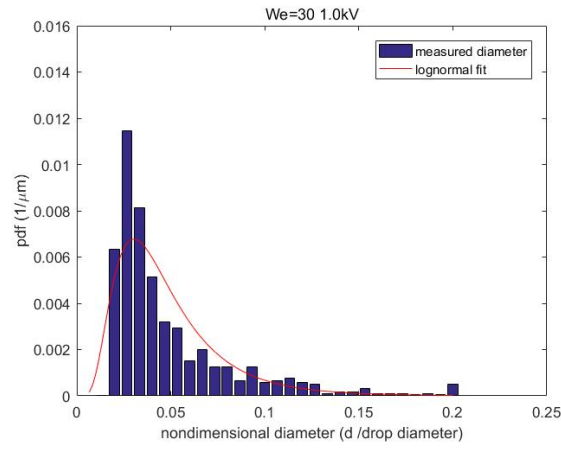


(c)

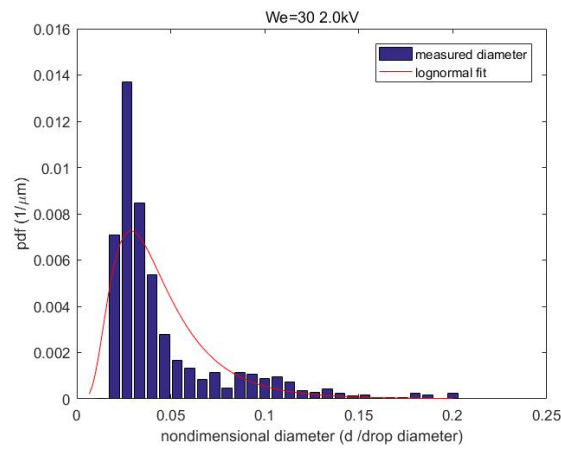
Figure 5.5 Ethanol diameter PDF at $We=25$ (a) $Q=0$, (b) $Q=0.0142$, (c) $Q=0.0319$



(a)



(b)

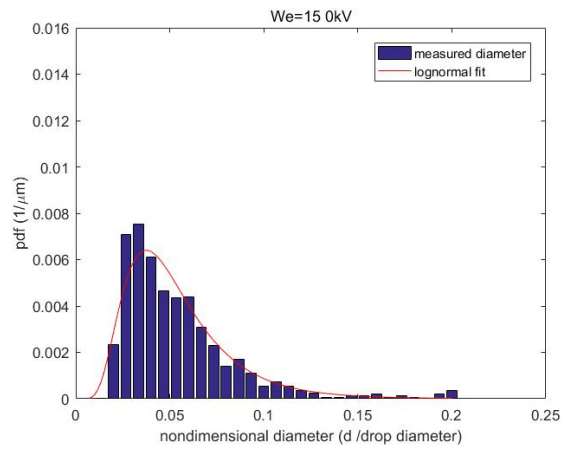


(c)

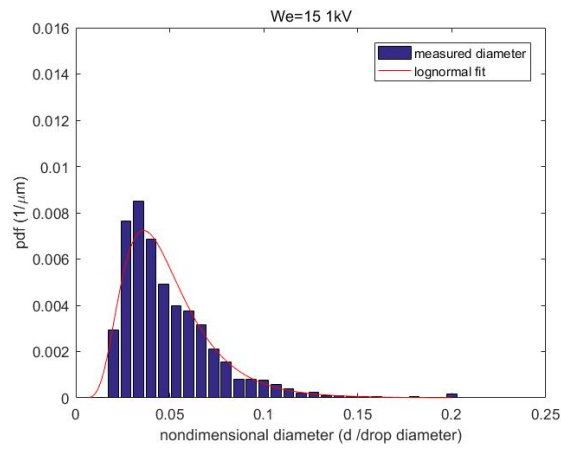
Figure 5.6 Ethanol diameter PDF at $We=30$ (a) $Q=0$, (b) $Q=0.0142$, (c) $Q=0.0319$

From 4 groups of graphs shown above, no apparent difference on the PDF was observed when the potential changes. The range of nondimensionalized fragment sizes is about 0.02 to 0.2. And most of fragments have a nondimensionalized diameter around 0.03.

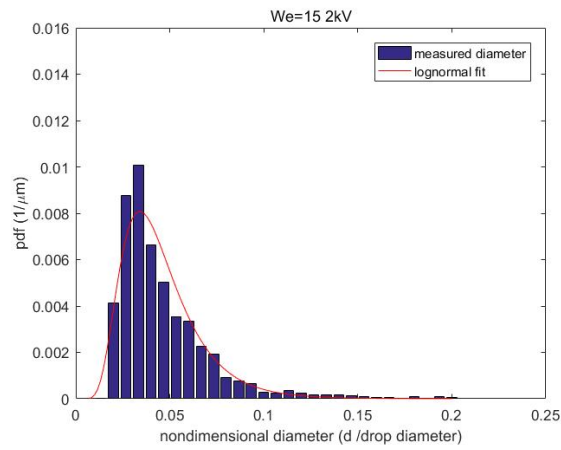
Similar to the ethanol results, graphs of salt solution PDF are shown next in Figure 5.7 to 5.10.



(a)

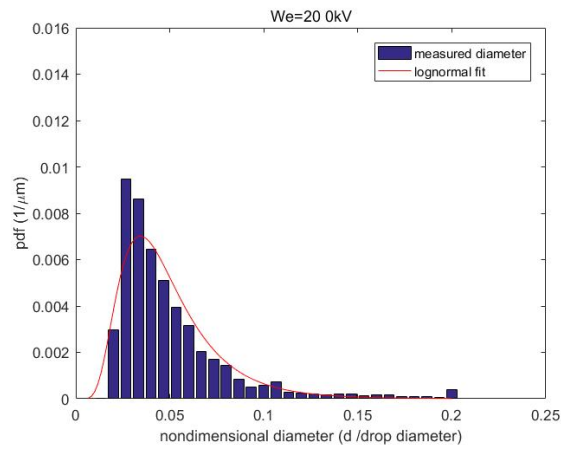


(b)

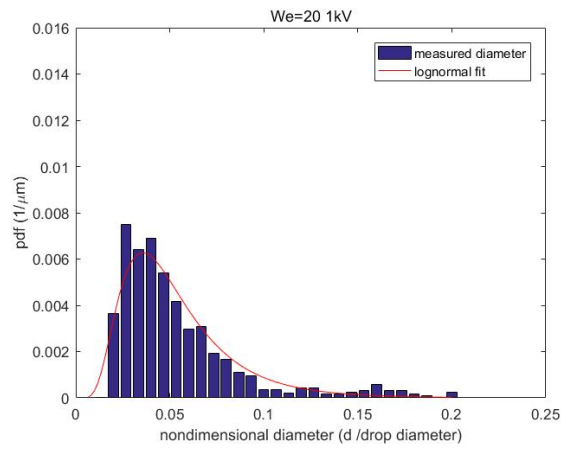


(c)

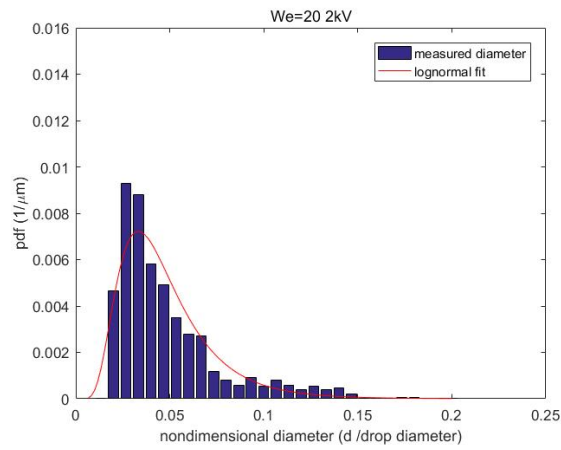
Figure 5.7 Salt solution diameter PDF at $We=15$ (a) $Q=0$, (b) $Q=0.0119$, (c) $Q=0.0331$



(a)

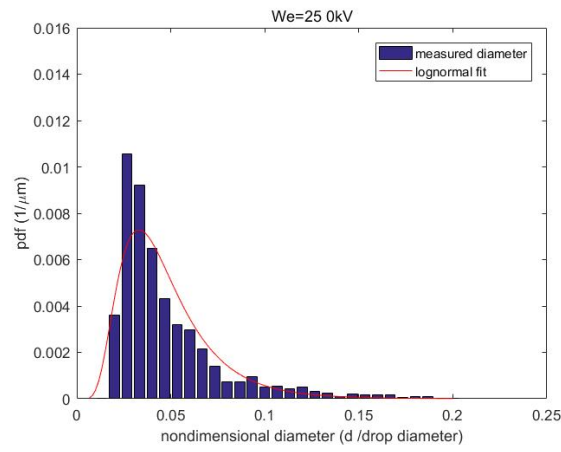


(b)

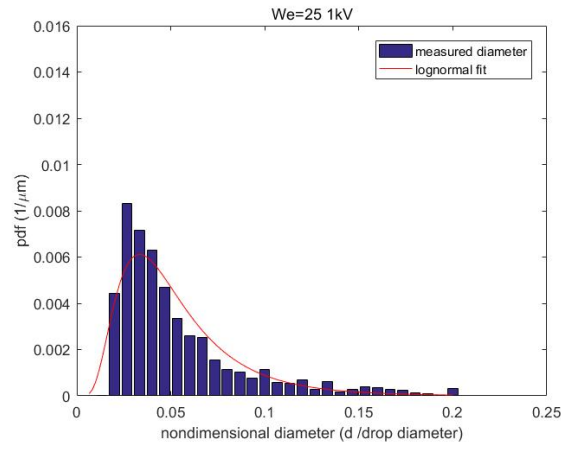


(c)

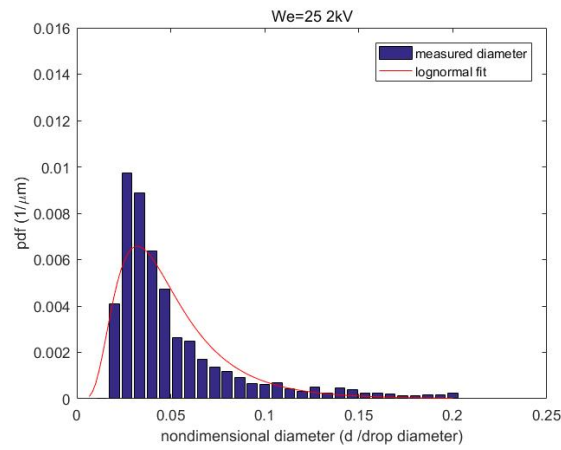
Figure 5.8 Salt solution diameter PDF at $We=20$ (a) $Q=0$, (b) $Q=0.0119$, (c) $Q=0.0331$



(a)

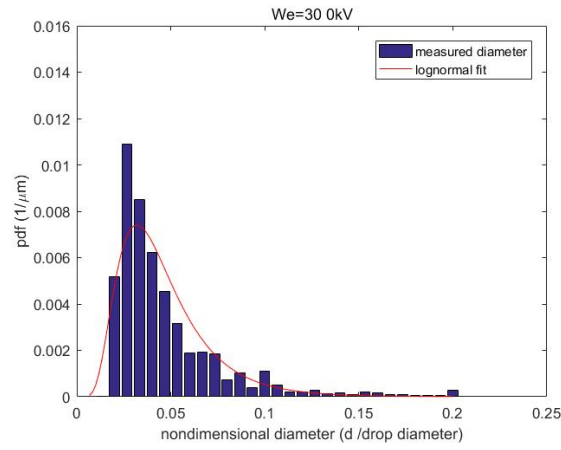


(b)

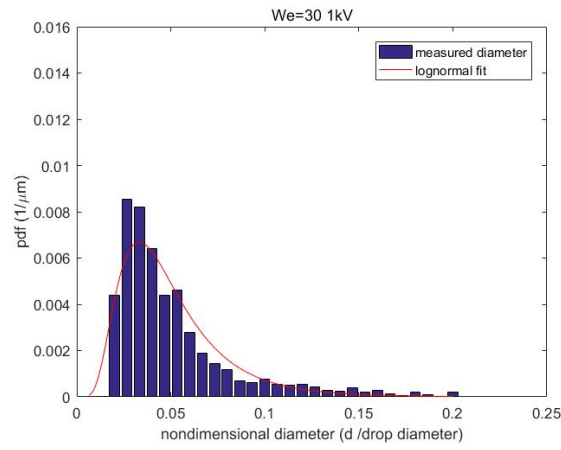


(c)

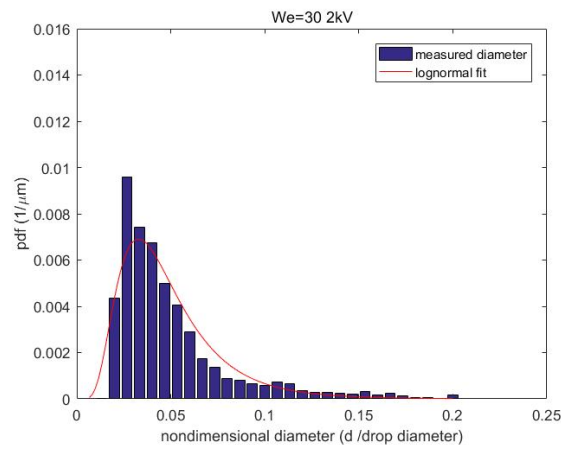
Figure 5.9 Salt solution diameter PDF at $We=25$ (a) $Q=0$, (b) $Q=0.0119$, (c) $Q=0.0331$



(a)



(b)



(c)

Figure 5.10 Salt solution diameter PDF at $We=30$ (a) $Q=0$, (b) $Q=0.0119$, (c) $Q=0.0331$

The results are also similar to the ethanol situation. The difference in the applied voltage did not give apparent change in the diameter PDF.

Besides the full range of fragment sizes, the full width at half maximum (FWHM) size results of ethanol and salt solution are also shown next. Specific values are shown in Table 5.3 and 5.4. And the results are also plotted in Figure 5.11 and 5.12 with uncertainty bar. All results shown are nondimensionalized.

Table 5.3 Ethanol FWHM of nondimensional fragment size

$Q \backslash We$	0	8.86×10^{-4}	0.0142	0.0221	0.0319
15	0.0336	0.0337	0.0321	0.0334	0.0369
20	0.0340	0.0331	0.0306	0.0331	0.0344
25	0.0332	0.0309	0.0302	0.0280	0.0322
30	0.0326	0.0350	0.0347	0.0342	0.0324

Table 5.4 Salt solution FWHM of nondimensional fragment size

$Q \backslash We$	0	0.0119	0.0331
15	0.0371	0.0331	0.0303
20	0.0342	0.0382	0.0332
25	0.0330	0.0383	0.0352
30	0.0323	0.0355	0.0345

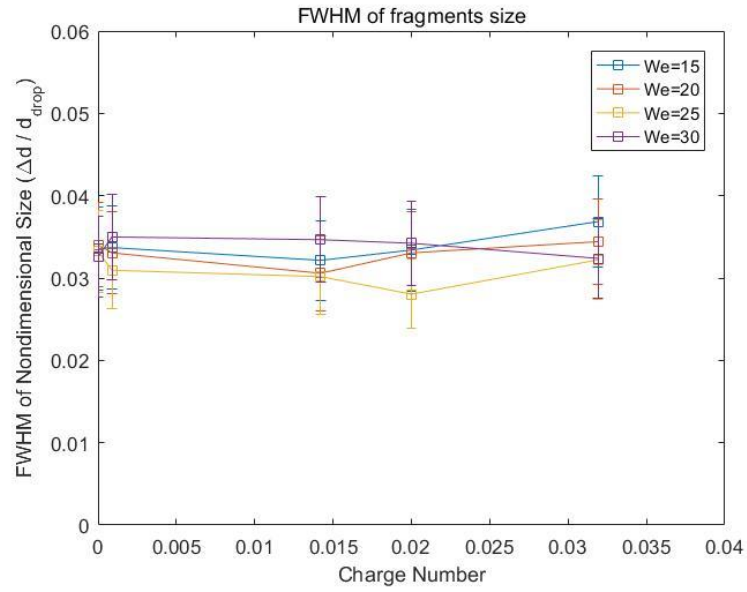


Figure 5.11 Ethanol FWHM of fragment size

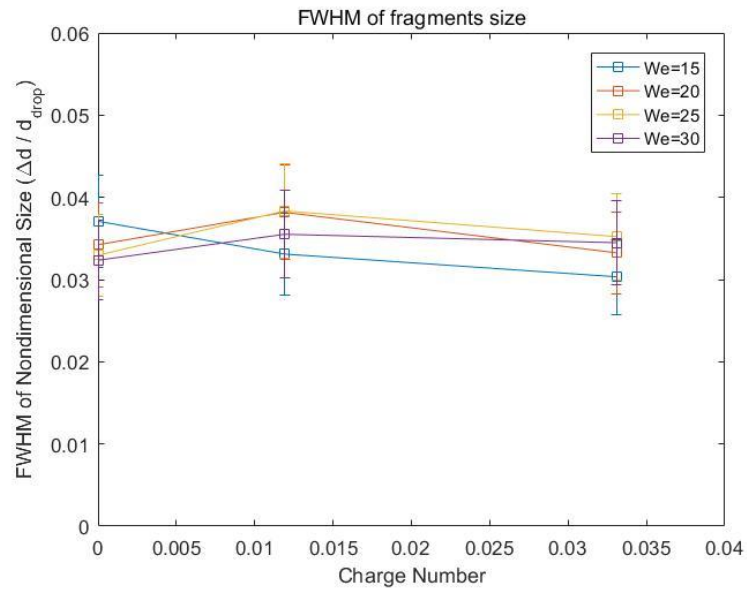


Figure 5.12 Salt solution FWHM of fragment size

The peak locations of histogram are shown in Table 5.5 to 5.6, and Figure 5.13 to 5.14.

Table 5.5 Ethanol peak location of nondimensional fragment size

$Q \backslash We$	0	8.86×10^{-4}	0.0142	0.0221	0.0319
15	0.0271	0.0256	0.0247	0.0264	0.0263
20	0.0271	0.0272	0.0251	0.0257	0.0274
25	0.0264	0.0255	0.0248	0.0262	0.0266
30	0.0284	0.0277	0.0279	0.0252	0.0257

Table 5.6 Salt solution peak location of nondimensional fragment size

$Q \backslash We$	0	0.0119	0.0331
15	0.0327	0.0298	0.0307
20	0.0300	0.0312	0.0296
25	0.0304	0.0298	0.0283
30	0.0283	0.0278	0.0289

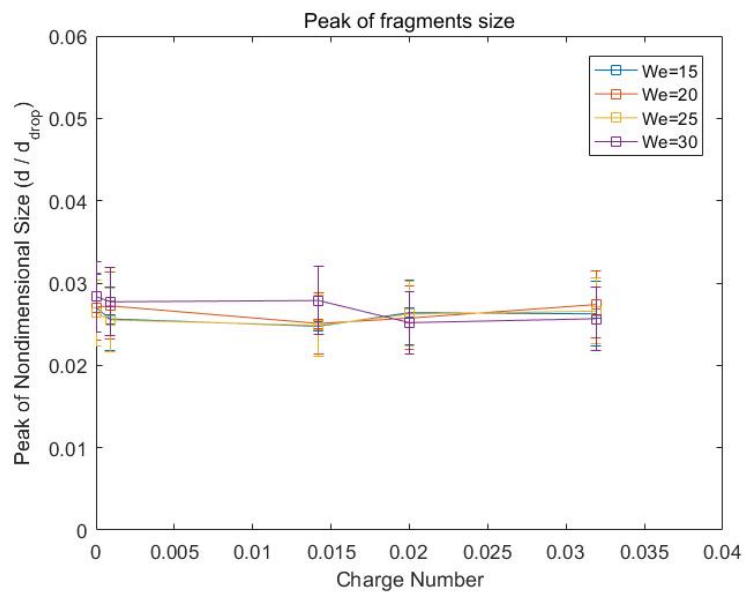


Figure 5.13 Ethanol peak location of fragment size

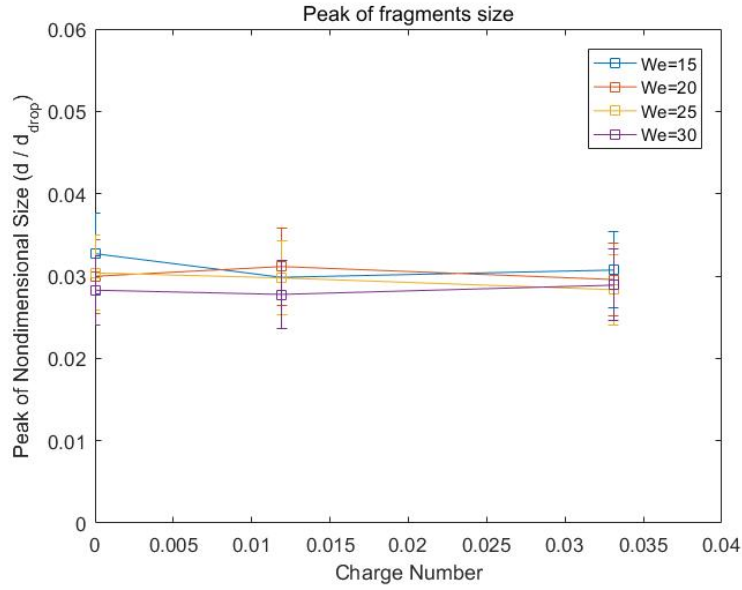


Figure 5.14 Salt solution peak location of fragment size

From above tables and figures, FWHM values of both ethanol and salt solution do not show significant difference as charge number changes. The observed differences are within the range of uncertainty. Similar to FWHM values, the results of peak location also show little relation between charge level and fragment sizes.

Log-normal size distributions for ethanol and salt-water solution can be described by the following expression:

$$f_0(D) = \frac{1}{D_0 \tilde{D} \sqrt{2\pi} \sigma_{ln}} \exp\left[-\frac{1}{2\sigma_{ln}^2} (\ln \tilde{D} - \bar{D}_{ln})^2\right] \quad (5.1)$$

Here σ_{ln} is the logarithmic standard deviation and \bar{D}_{ln} is the dimensionless logarithmic mean diameter. D_0 is the diameter of initial droplet and \tilde{D} is the dimensionless diameter.

For ethanol, $\bar{D}_{ln} = 0.0401$ and $\sigma_{ln} = 0.536$ with maximum errors of 9.15% and 13.9% respectively. And for salt-water solution, $\bar{D}_{ln} = 0.0446$ and $\sigma_{ln} = 0.501$ with maximum errors of 10.3% and 13.4% respectively.

To conclude, the charging voltage gives little effect to the fragment's diameter distribution. Nondimensional diameter of fragments mostly falls in the range from 0.02 to 0.2 for both charged and uncharged conditions. According to Guildenbecher (2009), charged droplets have no new breakup morphology and have roughly the same breakup time with the uncharged ones. In other words, the size of produced fragments has little connection to the charging condition of the initial droplet. And the result from this experiment is consistent with this conclusion. Although Guildenbecher (2009) achieved higher charge number, the charge level was not further increased due to the decreasing of the size of initial droplet at higher charge level. The peak location of fragment diameter might move to the low reliable range at current pixel size.

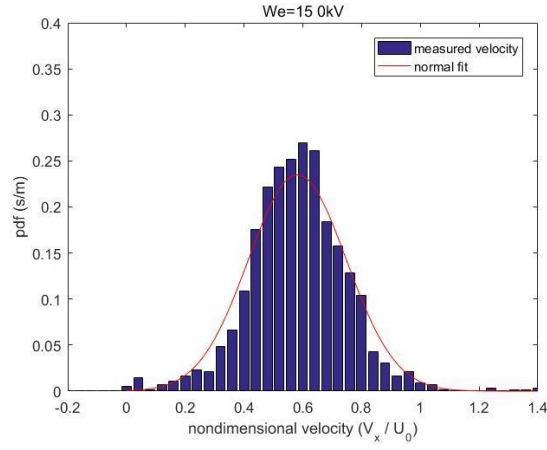
5.4 Velocity Distribution of Charged Breakup Fragments

5.4.1 Horizontal Velocity

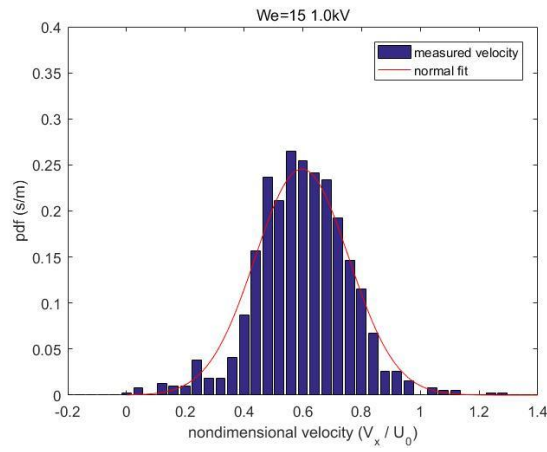
Besides with the size distribution, velocity of each fragment was computed by correlating the particles in consecutive frames. Horizontal and vertical velocities were measured and plotted in the figures shown next.

Different Weber number and applied voltage were conducted. On horizontal direction, velocities are nondimensionalized by dividing the average air velocity, U_0 , based on the Weber number.

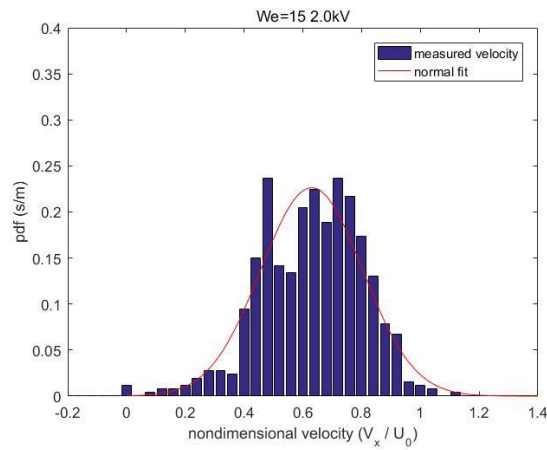
For ethanol group, part of results are show in Figure 5.15 to 5.18.



(a)

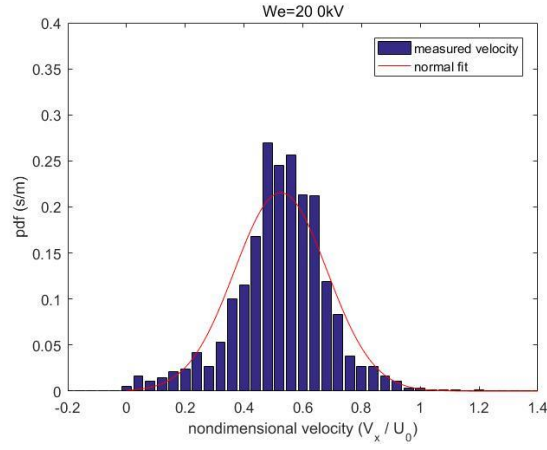


(b)

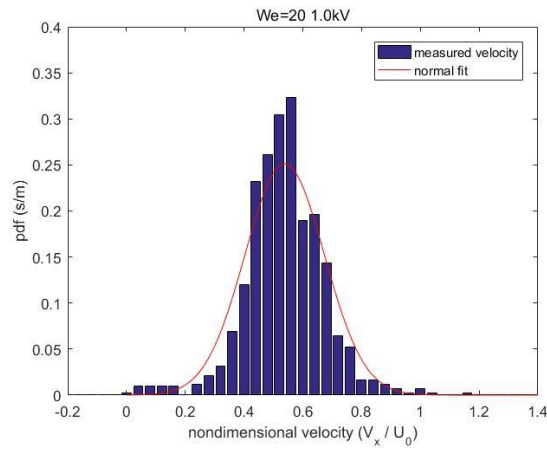


(c)

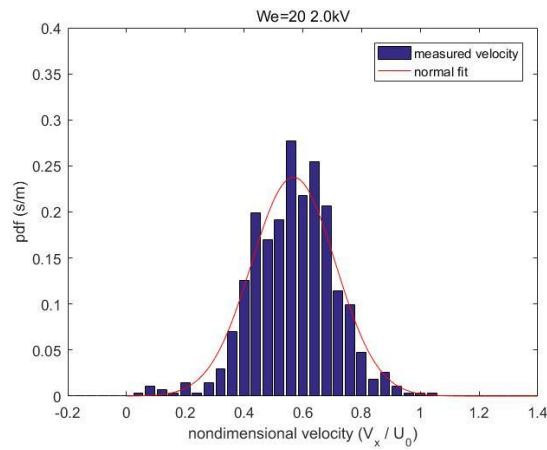
Figure 5.15 Ethanol horizontal velocity PDF at $We=15$ (a) $Q=0$, (b) $Q=0.0142$, (c) $Q=0.0319$



(a)

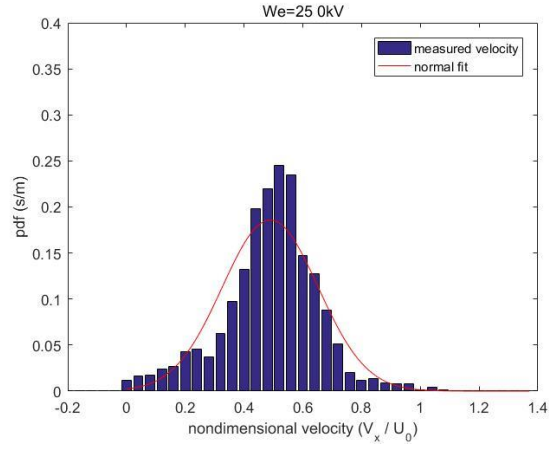


(b)

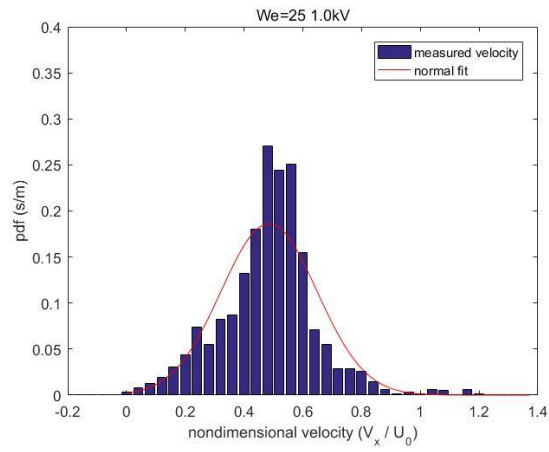


(c)

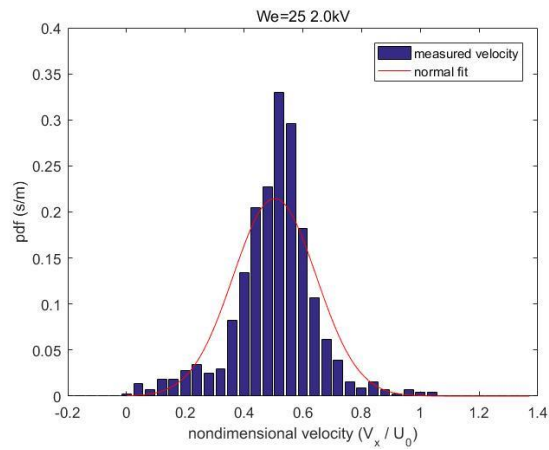
Figure 5.16 Ethanol horizontal velocity PDF at $We=20$ (a) $Q=0$, (b) $Q=0.0142$, (c) $Q=0.0319$



(a)

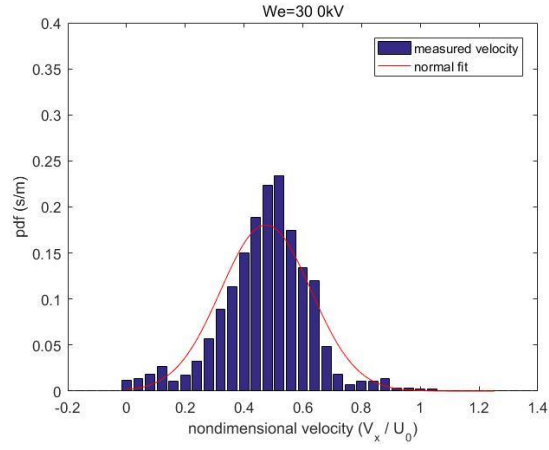


(b)

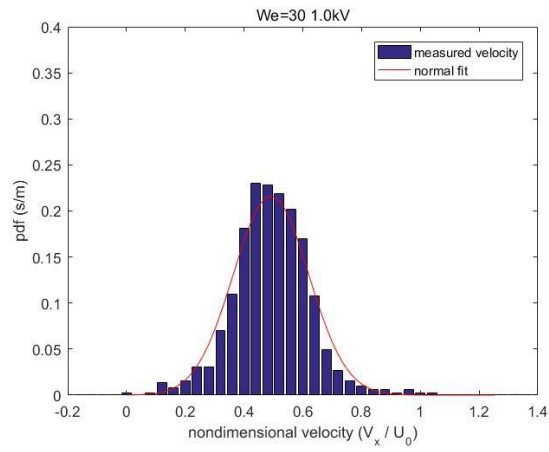


(c)

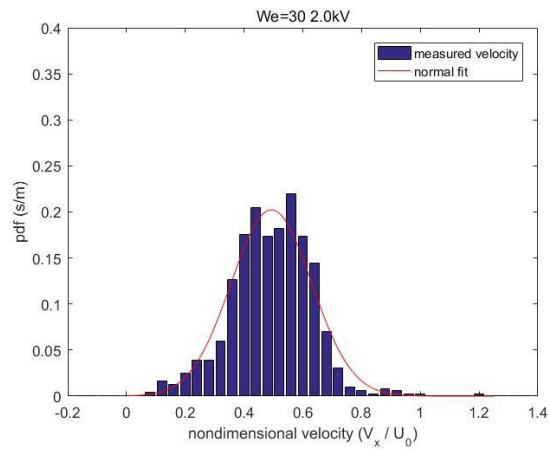
Figure 5.17 Ethanol horizontal velocity PDF at $We=25$ (a) $Q=0$, (b) $Q=0.0142$, (c) $Q=0.0319$



(a)



(b)

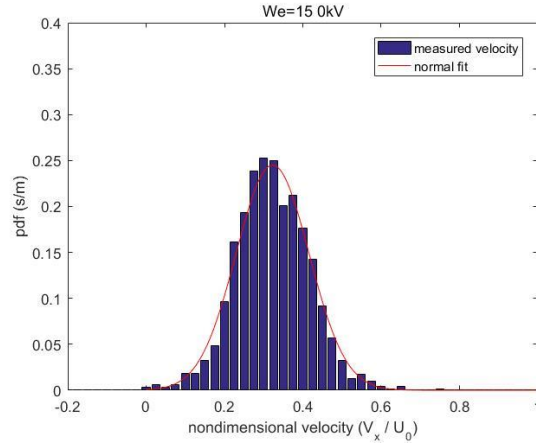


(c)

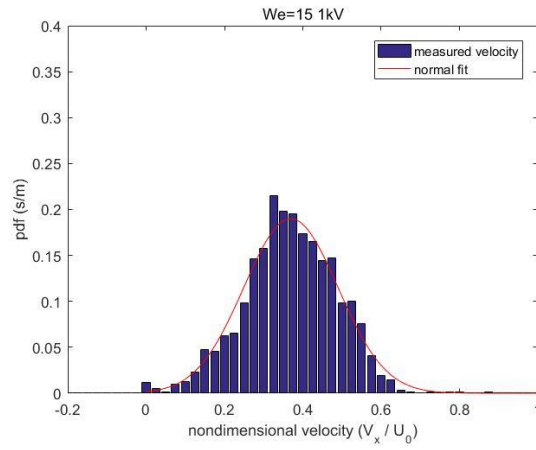
Figure 5.18 Ethanol horizontal velocity PDF at $We=30$ (a) $Q=0$, (b) $Q=0.0142$, (c) $Q=0.0319$

For ethanol, the horizontal velocity PDF did not change too much at different applied voltage under the same Weber number. Although with some oscillation, the peak location of nondimensional velocity is around 0.5.

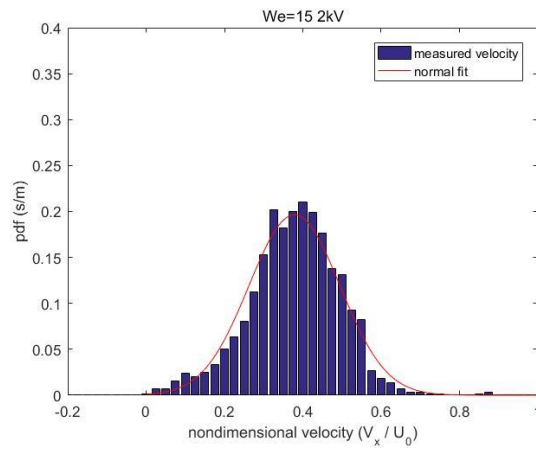
By matching the salt solution particles from processed holograms, the velocity distribution of salt solution was also obtained. The nondimensional horizontal velocities of salt solution groups are plotted below in Figure 5.19 to 5.22.



(a)

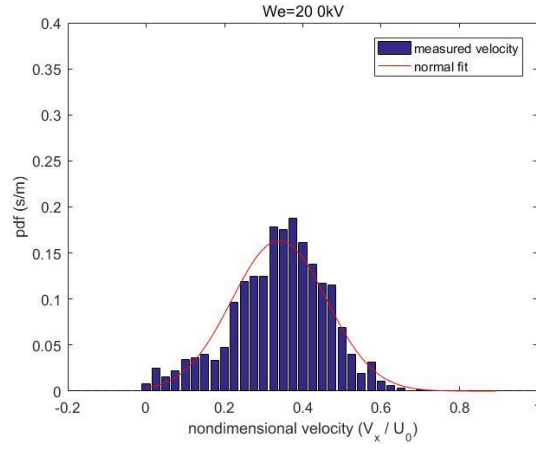


(b)

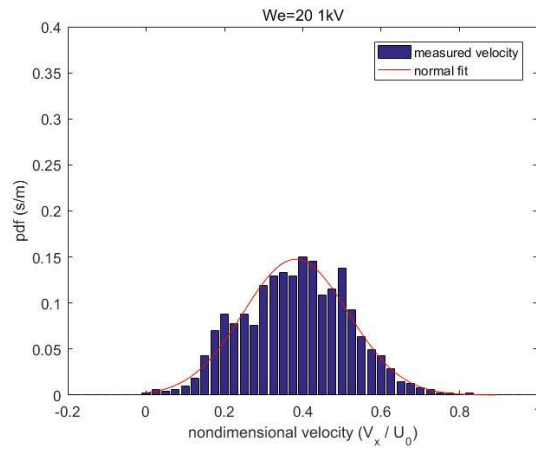


(c)

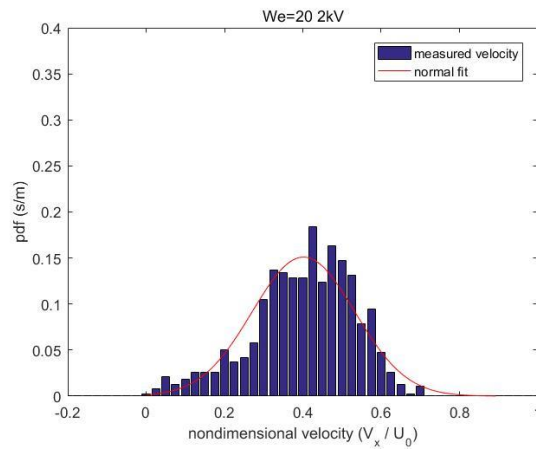
Figure 5.19 Salt solution horizontal velocity PDF at $We=15$ (a) $Q=0$, (b) $Q=0.0119$, (c) $Q=0.0331$



(a)

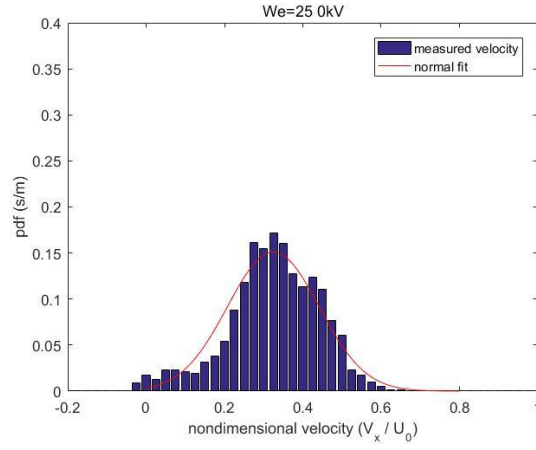


(b)

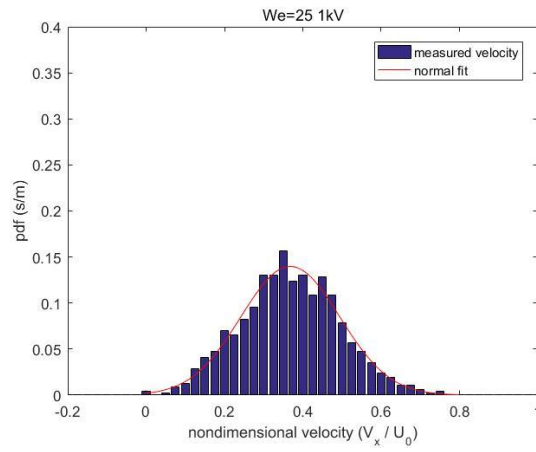


(c)

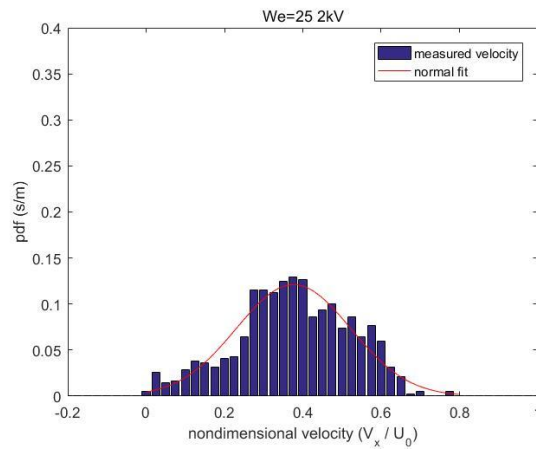
Figure 5.20 Salt solution horizontal velocity PDF at $We=20$ (a) $Q=0$, (b) $Q=0.0119$, (c) $Q=0.0331$



(a)

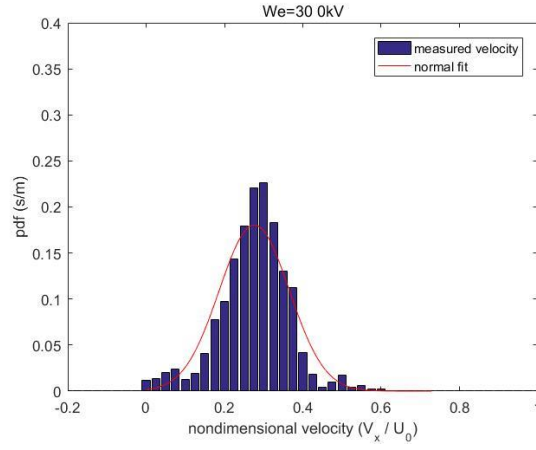


(b)

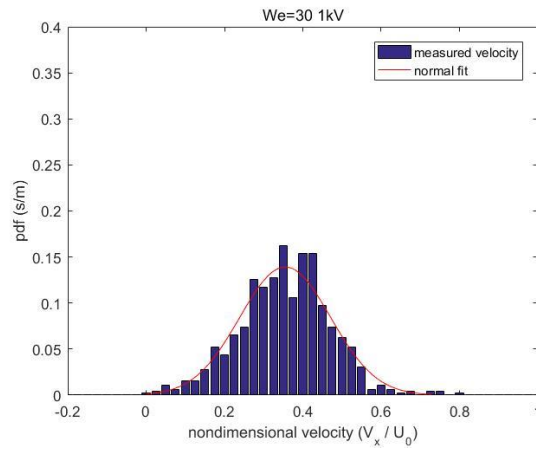


(c)

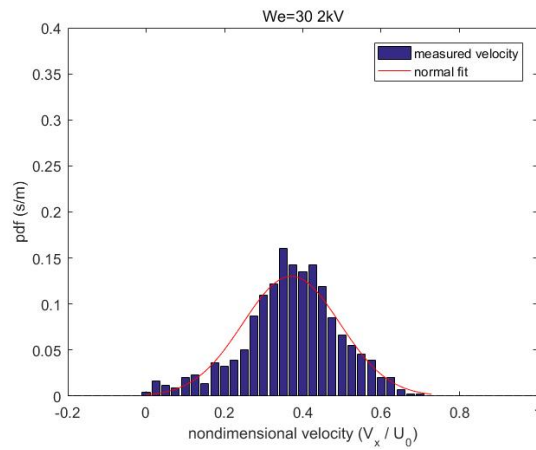
Figure 5.21 Salt solution horizontal velocity PDF at $We=25$ (a) $Q=0$, (b) $Q=0.0119$, (c) $Q=0.0331$



(a)



(b)



(c)

Figure 5.22 Salt solution horizontal velocity PDF at $We=30$ (a) $Q=0$, (b) $Q=0.0119$, (c) $Q=0.0331$

Similar to the former section, the FWHM and peak location of velocity are shown below. To reduce the effect of We , fragment velocities were nondimensionalized by dividing the average air velocity, U_0 , based on the We . The specific values are shown in Table 5.7 to 5.8.

Table 5.7 Ethanol FWHM of nondimensional horizontal velocity

$We \backslash Q$	0	8.86×10^{-4}	0.0142	0.0221	0.0319
15	0.393	0.333	0.376	0.398	0.408
20	0.371	0.310	0.319	0.324	0.337
25	0.385	0.330	0.385	0.382	0.334
30	0.362	0.319	0.302	0.340	0.323

Table 5.8 Salt solution FWHM of nondimensional horizontal velocity

$We \backslash Q$	0	0.0119	0.0331
15	0.219	0.283	0.274
20	0.285	0.316	0.308
25	0.276	0.298	0.344
30	0.294	0.273	0.292

The results are plotted in Figure 5.23 and 5.24 with uncertainty bar.

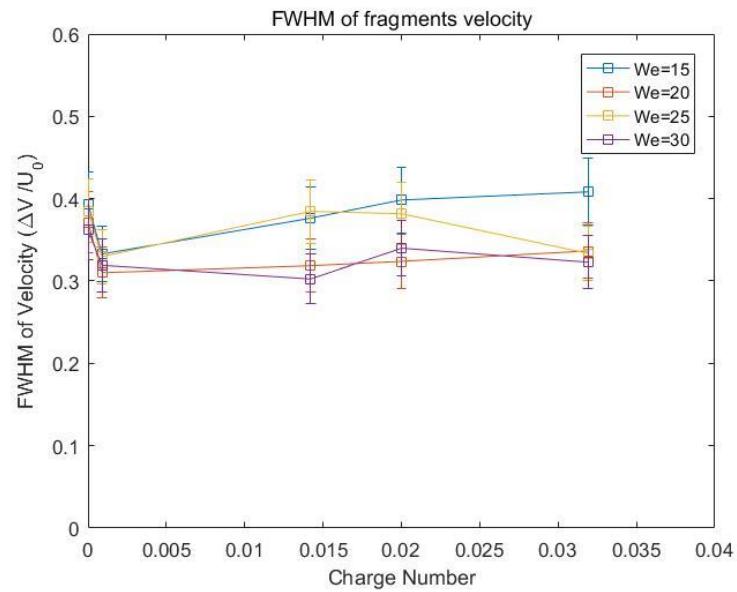


Figure 5.23 Ethanol FWHM of fragment horizontal velocity

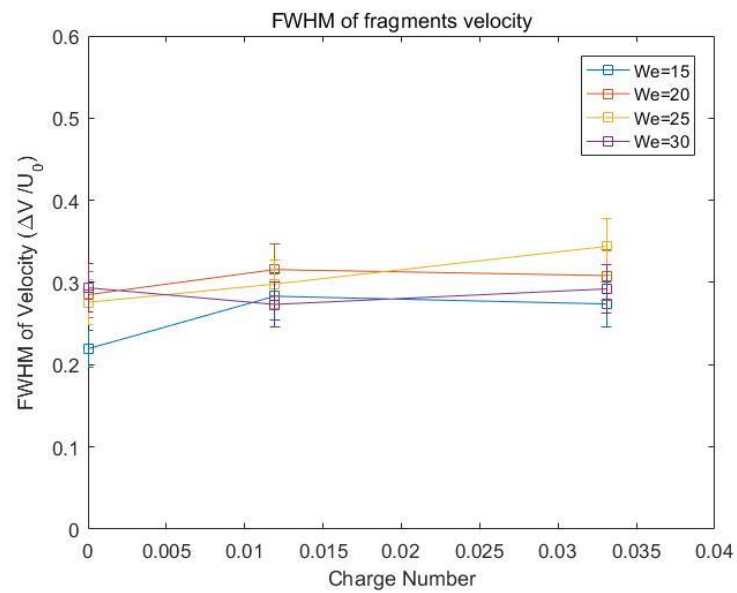


Figure 5.24 Salt solution FWHM of fragment horizontal velocity

The peak values are also shown in the following tables and figures.

Table 5.9 Ethanol peak location of nondimensional horizontal velocity

$We \backslash Q$	0	8.86×10^{-4}	0.0142	0.0221	0.0319
15	0.601	0.591	0.590	0.581	0.660
20	0.522	0.540	0.518	0.571	0.591
25	0.526	0.502	0.514	0.516	0.539
30	0.498	0.477	0.462	0.509	0.546

Table 5.10 Salt solution peak location of nondimensional horizontal velocity

$We \backslash Q$	0	0.0119	0.0331
15	0.294	0.348	0.380
20	0.354	0.392	0.446
25	0.320	0.357	0.361
30	0.317	0.354	0.373

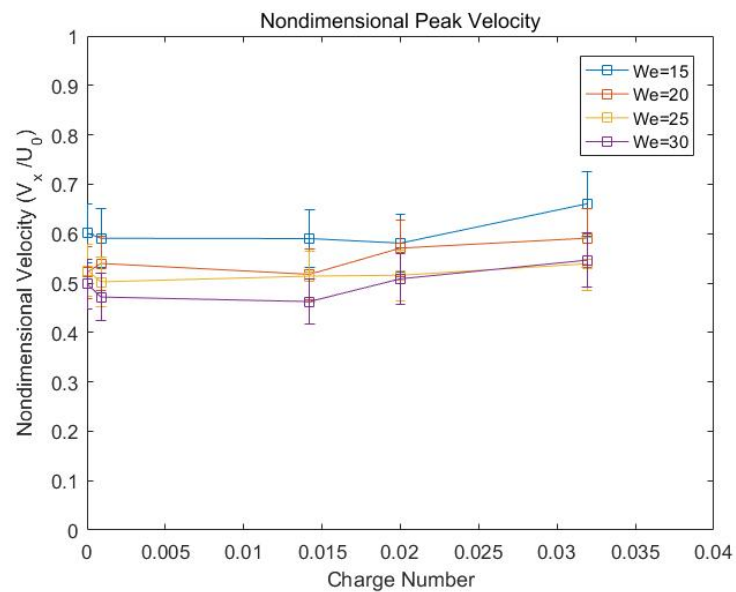


Figure 5.25 Ethanol peak location of fragment horizontal velocity

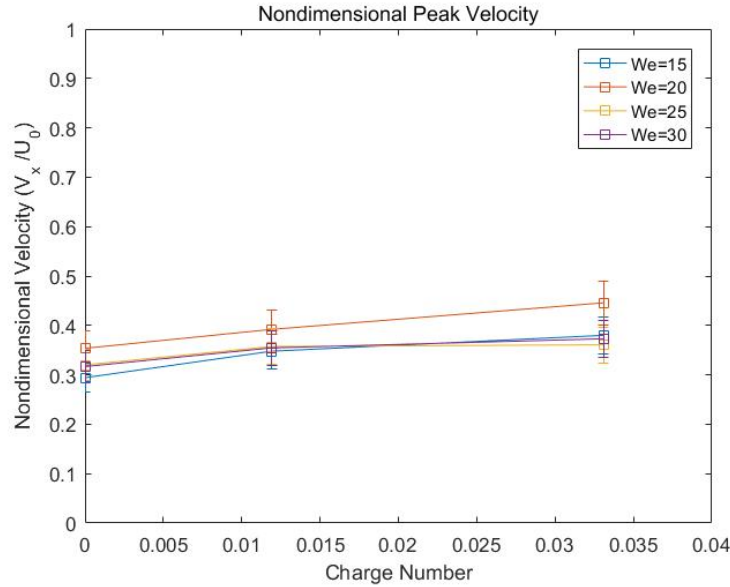


Figure 5.26 Salt solution peak location of fragment horizontal velocity

Combining the plots and tables shown above, no big changes on the FWHM and peak location of the fragment velocity. Thus, we are able to conclude the charge level of the droplet has no contribution to the fragment velocities for either ethanol or salt solution. Though some oscillation or rising tendency are observed, these differences still within the range of uncertainty.

Normalized Gaussian horizontal velocity distribution for ethanol and salt-water solution can be described as:

$$\text{PDF}(\tilde{V}_x) = \frac{1}{U_0 \sigma_s \sqrt{2\pi}} \exp\left[-\frac{(\tilde{V}_x - \bar{\tilde{V}}_x)^2}{2\sigma_s^2}\right] \quad (5.2)$$

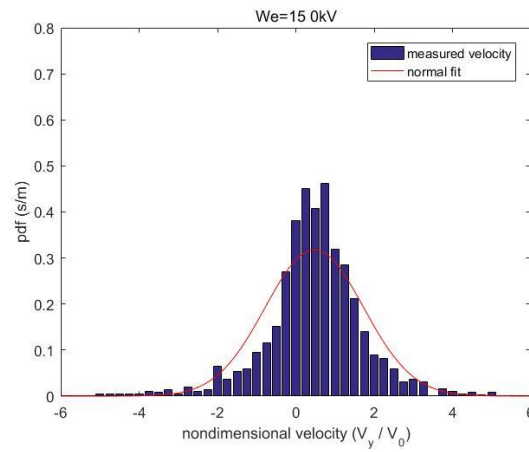
Here \tilde{V}_x is dimensionless horizontal velocity of fragments and $\bar{\tilde{V}}_x$ is the mean of dimensionless horizontal velocity of fragments. U_0 is air flow velocity and σ_s is standard deviation of dimensionless horizontal velocity.

For ethanol, $\bar{\tilde{V}}_x = 0.528$ and $\sigma_s = 0.149$ with maximum error around 19.4% and 16.1%. For salt-water solution group, $\bar{\tilde{V}}_x = 0.355$ and $\sigma_s = 0.149$ with maximum error around 22.3% and 25.2%.

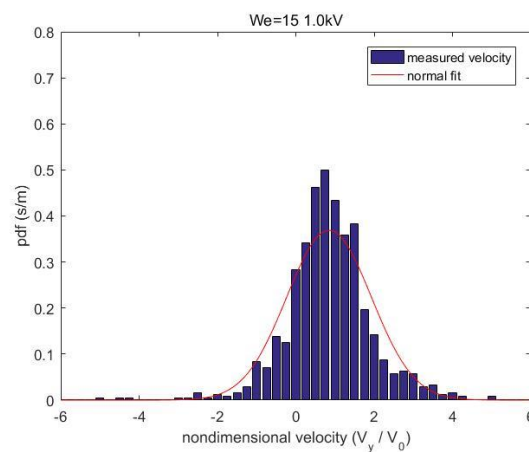
5.4.2 Vertical Velocity

Besides the horizontal velocity plots, vertical velocity of fragments was also collected and plotted. And vertical velocities were further processed to get the acceleration on the vertical direction which would be presented in the next section.

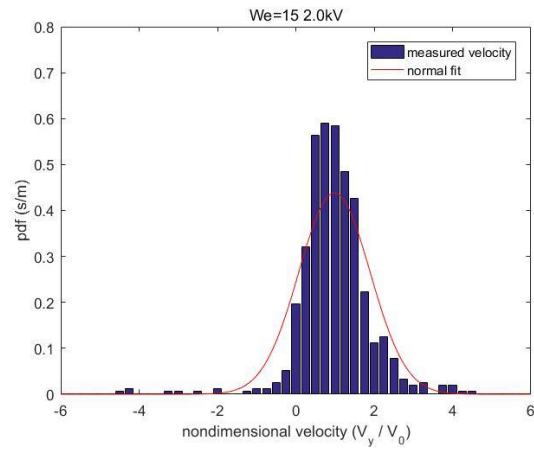
Similar to the former section, the vertical velocities were nondimensionalized by dividing the initial droplet velocity, V_0 . It could be computed based on the distance from needle tip to the center of air nozzle. The results of nondimensionalized vertical velocities of ethanol fragments were plotted in Figure 5.27 to 5.30.



(a)

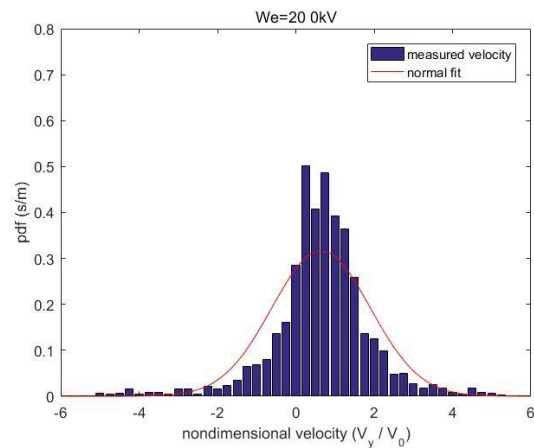


(b)

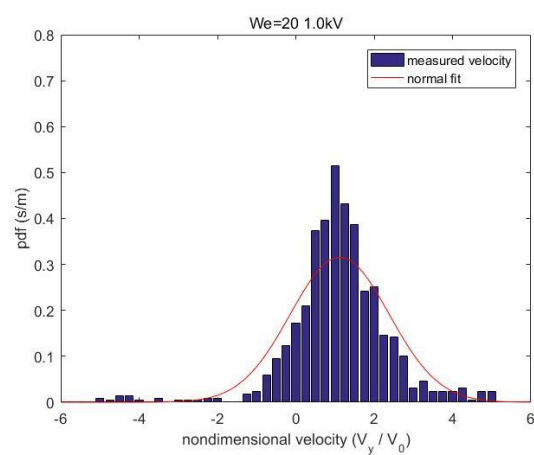


(c)

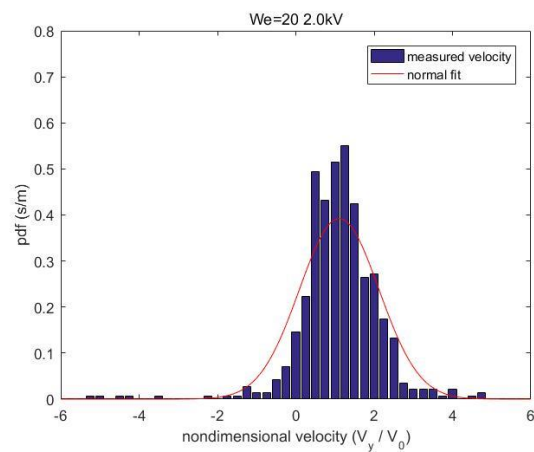
Figure 5.27 Ethanol vertical velocity PDF at $We=15$ (a) $Q=0$, (b) $Q=0.0142$, (c) $Q=0.0319$



(a)

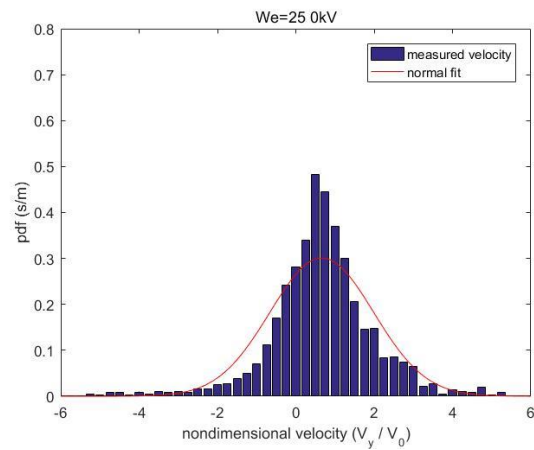


(b)

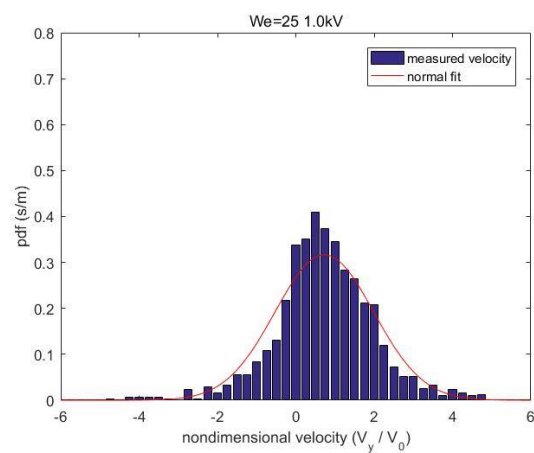


(c)

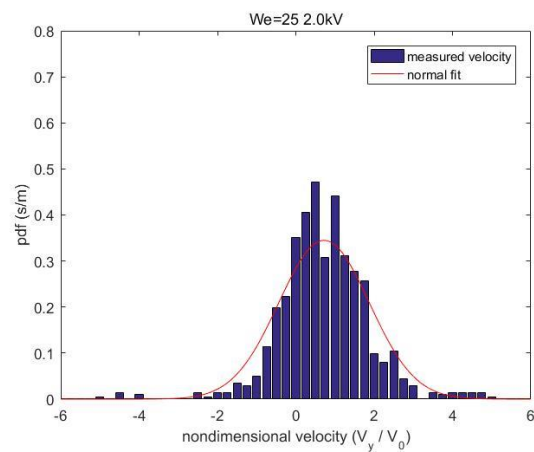
Figure 5.28 Ethanol vertical velocity PDF at $We=20$ (a) $Q=0$, (b) $Q=0.0142$, (c) $Q=0.0319$



(a)

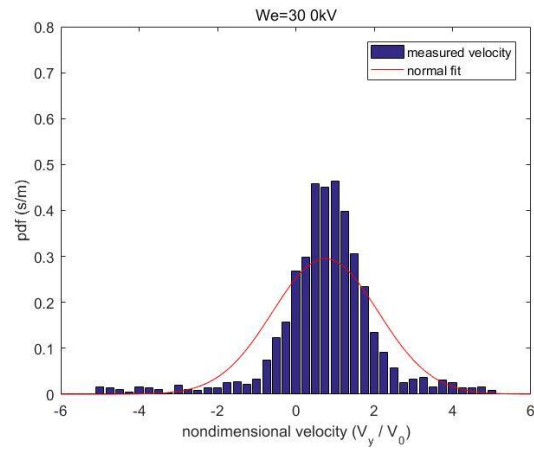


(b)

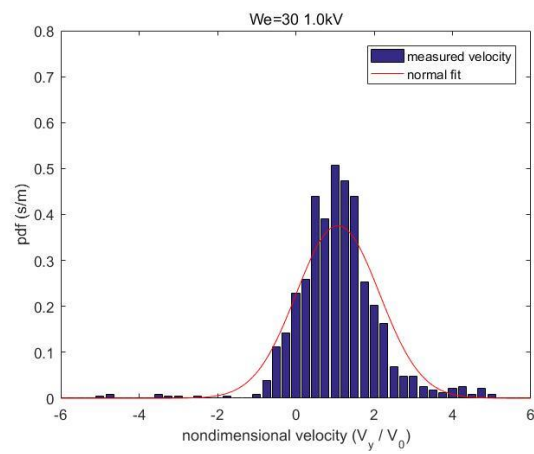


(c)

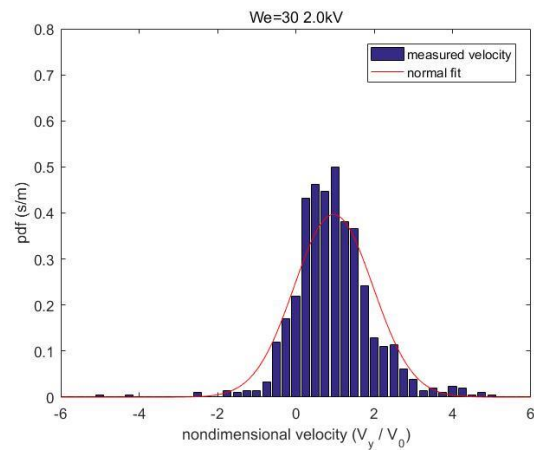
Figure 5.29 Ethanol vertical velocity PDF at $We=25$ (a) $Q=0$, (b) $Q=0.0142$, (c) $Q=0.0319$



(a)



(b)

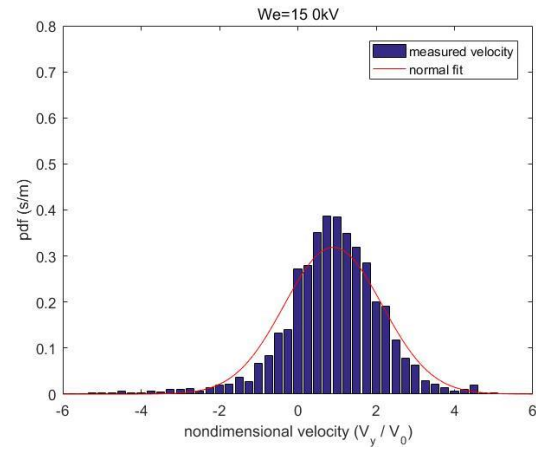


(c)

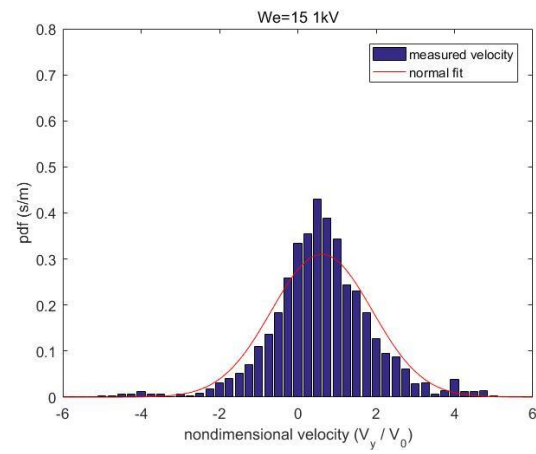
Figure 5.30 Ethanol vertical velocity PDF at $We=30$ (a) $Q=0$, (b) $Q=0.0142$, (c) $Q=0.0319$

Different from horizontal velocity, the vertical velocity appears to concentrate more around the value smaller than 1. It is reasonable since the initial droplet accelerated vertically due to the effect of gravity and decelerated due to the drag act on it. A bag was formed and broke apart during the breakup process. The spatially expanded bag, in some extent, contributed to the vertical velocity, making vertical velocity varied.

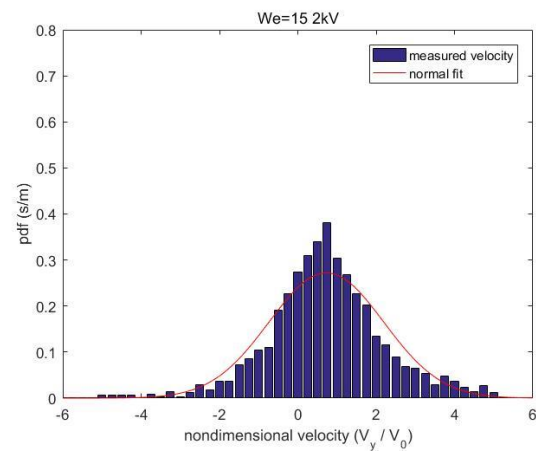
Besides with the ethanol results, the graphs of salt solution group are also shown in Figure 5.31 to 5.34 below.



(a)

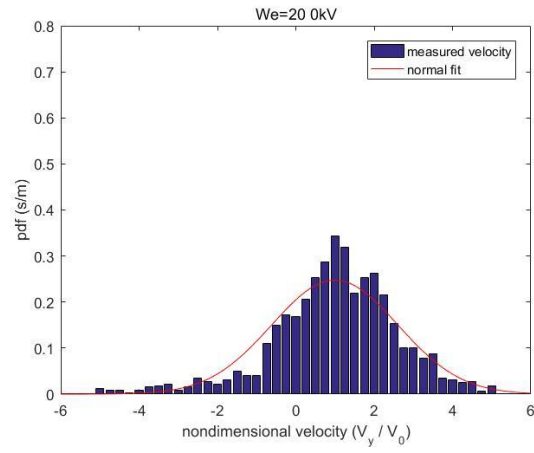


(b)

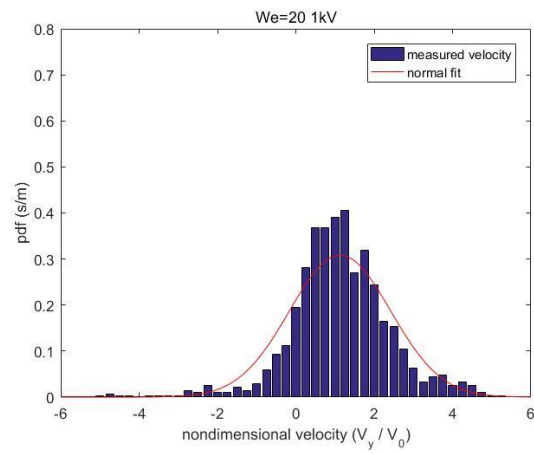


(c)

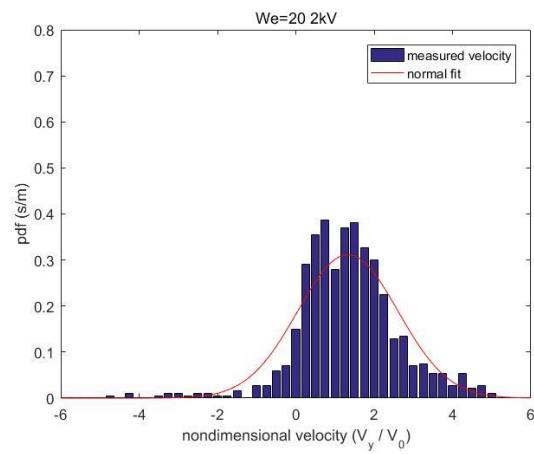
Figure 5.31 Salt solution vertical velocity PDF at $We=15$ (a) $Q=0$, (b) $Q=0.0119$, (c) $Q=0.0331$



(a)

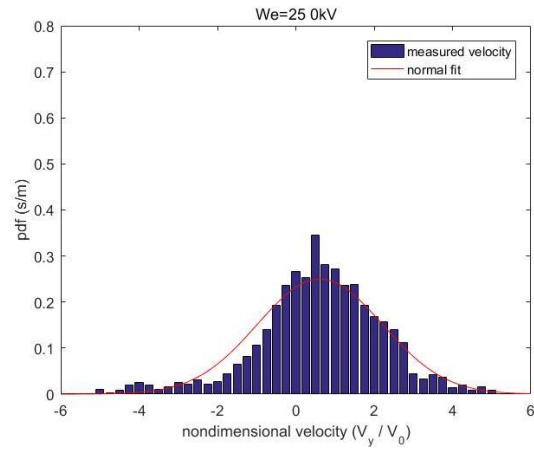


(b)

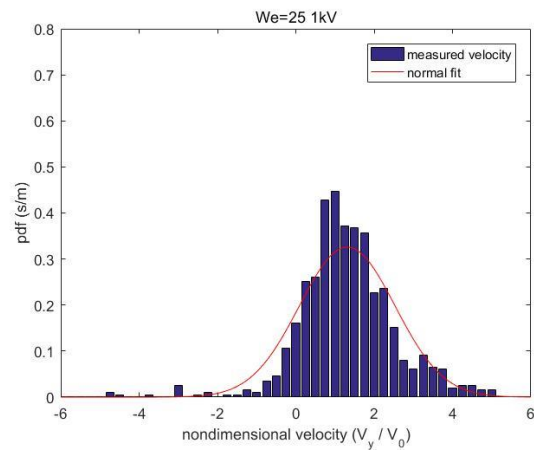


(c)

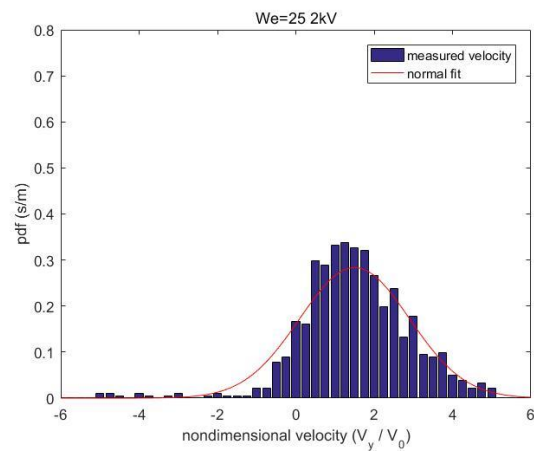
Figure 5.32 Salt solution vertical velocity PDF at $We=20$ (a) $Q=0$, (b) $Q=0.0119$, (c) $Q=0.0331$



(a)

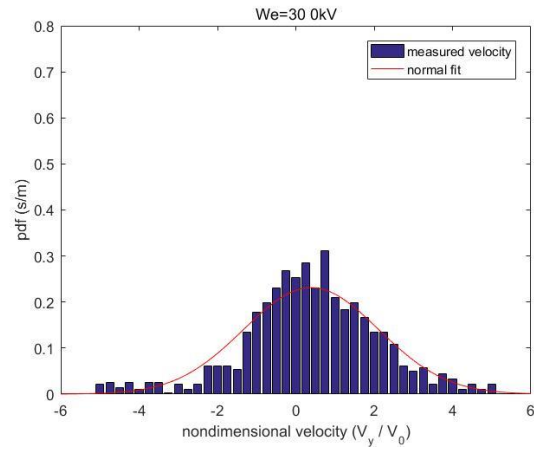


(b)

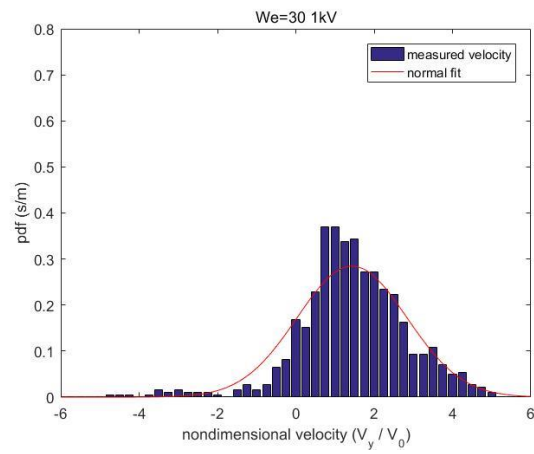


(c)

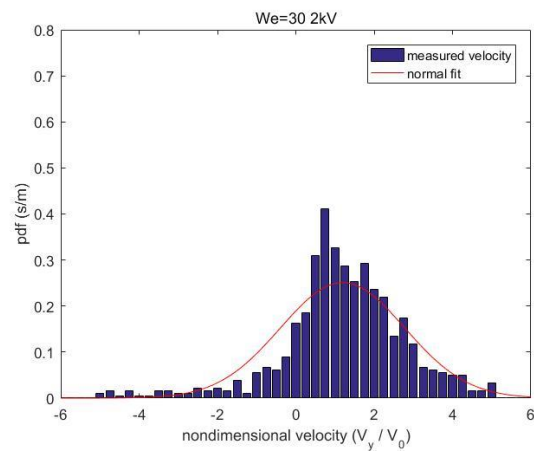
Figure 5.33 Salt solution vertical velocity PDF at $We=25$ (a) $Q=0$, (b) $Q=0.0119$, (c) $Q=0.0331$



(a)



(b)



(c)

Figure 5.34 Salt solution vertical velocity PDF at $We=30$ (a) $Q=0$, (b) $Q=0.0119$, (c) $Q=0.0331$

As shown in previous sections, FWHM of vertical velocity for fragments are also given next in Tables and Figures.

Table 5.11 Ethanol FWHM of nondimensional vertical velocity

$Q \backslash We$	0	8.86×10^{-4}	0.0142	0.0221	0.0319
15	2.96	2.15	2.55	2.21	2.14
20	2.97	2.96	2.98	2.78	2.39
25	3.12	2.64	2.97	2.83	2.69
30	3.19	2.65	2.50	2.33	2.37

Table 5.12 Salt solution FWHM of nondimensional vertical velocity

$Q \backslash We$	0	0.0119	0.0331
15	2.95	3.03	3.45
20	3.79	3.05	3.01
25	3.76	2.88	3.30
30	4.11	3.30	3.74

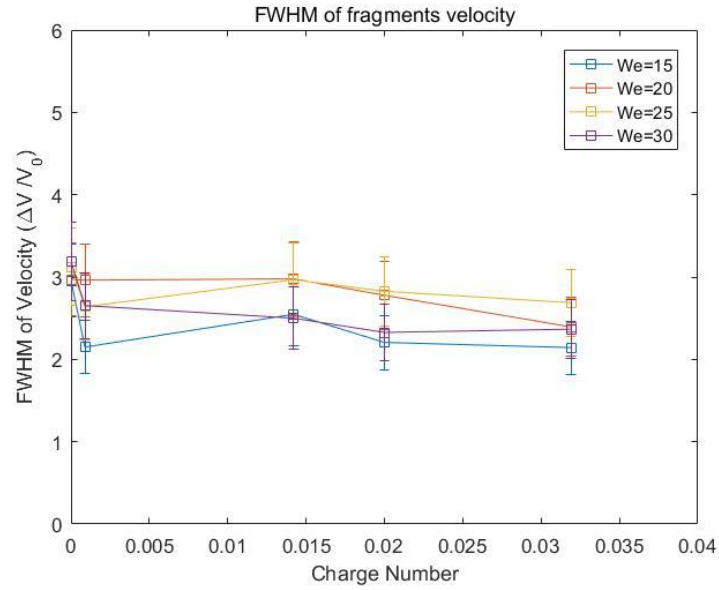


Figure 5.35 Ethanol FWHM of fragment vertical velocity

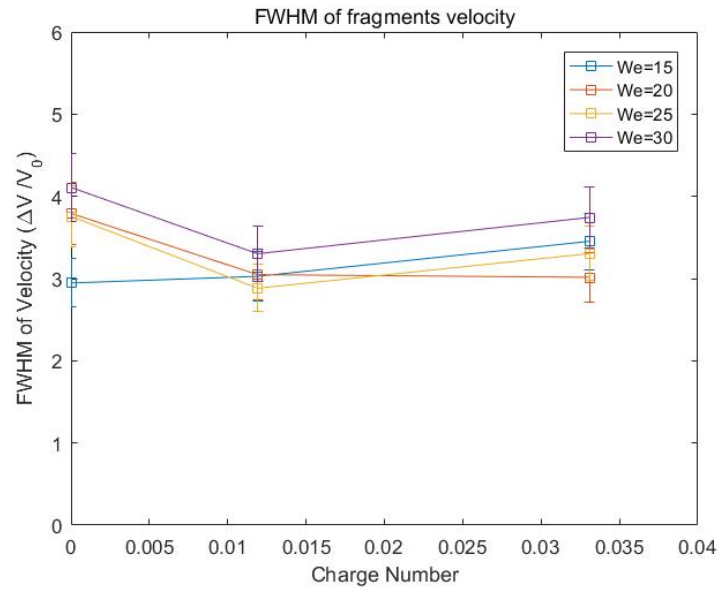


Figure 5.36 Salt solution FWHM of fragment vertical velocity

The information of the peak location of nondimensional vertical velocity are listed in Table 5.13 and Table 5.14. Plots with uncertainty bars are given in Figure 5.37 and Figure 5.38.

Table 5.13 Ethanol peak location of nondimensional vertical velocity

$We \backslash Q$	0	8.86×10^{-4}	0.0142	0.0221	0.0319
15	0.537	0.689	0.701	0.823	0.896
20	0.703	1.14	1.01	0.960	1.13
25	0.666	0.600	0.567	0.812	0.720
30	0.765	1.15	1.02	0.938	0.795

Table 5.14 Salt solution peak location of nondimensional vertical velocity

$We \backslash Q$	0	0.0119	0.0331
15	0.847	0.518	0.629
20	1.01	0.985	1.25
25	0.650	0.976	1.16
30	0.438	1.20	0.825

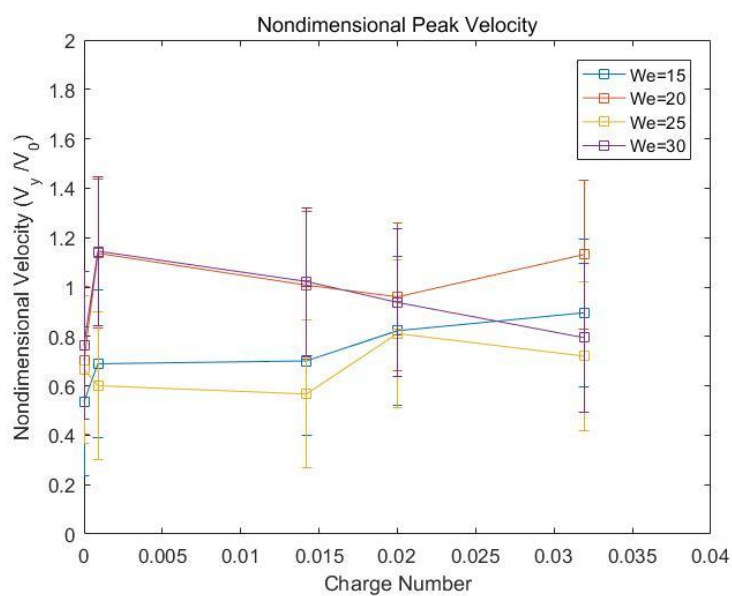


Figure 5.37 Ethanol peak location of fragment vertical velocity

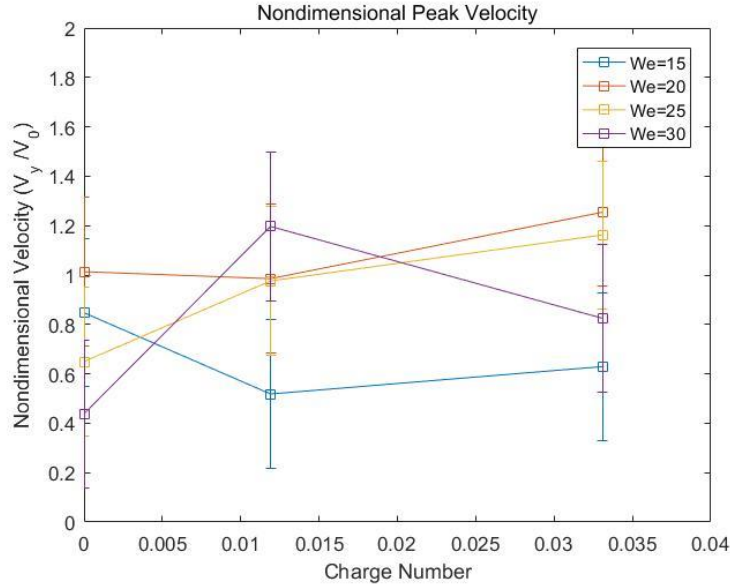


Figure 5.38 Salt solution peak location of fragment vertical velocity

From the charts and graphs above, the salt solution results, similar to the ethanol results, also concentrate to a relatively low value compared to the horizontal ones. And the results of vertical velocity for both ethanol and salt solution show no apparent change as charging potential increases.

Normalized Gaussian vertical velocity distribution for ethanol and salt-water solution is shown in the following expression:

$$\text{PDF}(\tilde{V}_y) = \frac{1}{V_0 \sigma_s \sqrt{2\pi}} \exp\left[-\frac{(\tilde{V}_y - \bar{\tilde{V}}_y)^2}{2\sigma_s^2}\right] \quad (5.3)$$

Here \tilde{V}_y is dimensionless vertical velocity of fragments and $\bar{\tilde{V}}_y$ is the mean of dimensionless vertical velocity of fragments. V_0 is vertical velocity of the initial drop let and σ_s is standard deviation of fragment vertical velocity.

Based on the results of vertical velocity of ethanol group, $\bar{\tilde{V}}_y = 0.868$ and $\sigma_s = 1.13$ with maximum error around 20.2% and 19.7%. For salt-water solution group, $\bar{\tilde{V}}_y = 1.01$ and $\sigma_s = 1.43$ with maximum error around 25.8% and 20.6%. Combining with FWHM and peak location

results provided above, we could believe the PDFs of nondimensional velocity are independent of charge number and Weber number.

To shortly conclude, the size and velocity PDFs were explored. For both types of liquid used in this experiment, no apparent difference was found when charge was induced on the initial droplet. Some oscillation of peak location, though occurred, still sit in the range of uncertainty. The expressions of size and velocity PDFs are given. And the PDFs show good consistence at different charge or Weber numbers.

5.5 Acceleration of Charged Breakup Fragments

A group of acceleration result is shown in Figure 5.35. Varied from hundred to thousand meter per second square both positively and negatively, the acceleration result seems to make no sense. The main reason leading to this problem is the camera resolution.

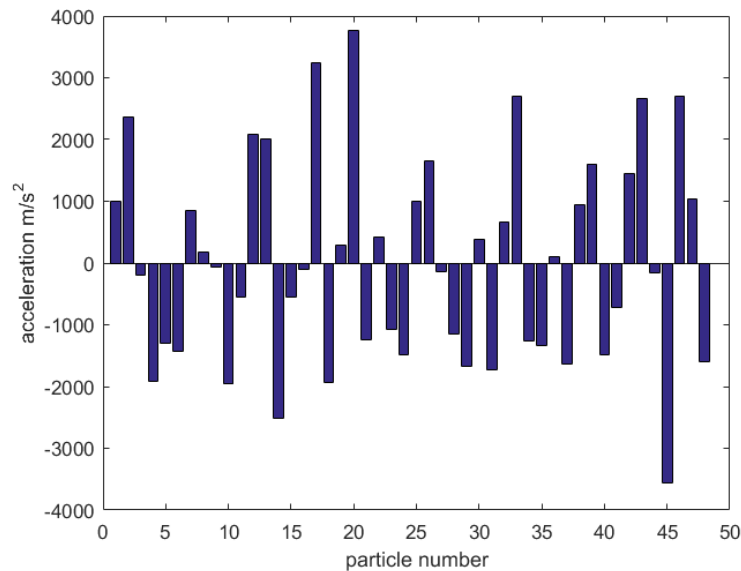


Figure 5.39 Acceleration of particles on vertical direction

From section 4.8, the minimal detected acceleration is 8000 m/s^2 . Using Eq. (4.20), the minimal potential for fragments at certain diameter could be obtained. For the smallest fragment that could be effectively detected with this resolution, the minimal potential is 47kV. According to Eq. (4.20), the uncertainty at this diameter is about 6kV. For the largest detected fragment, the

required minimal potential is 1.5MV, with the uncertainty about 0.2MV. The required potential is too high for current setup to achieve. And further protection to avoid electric shock is needed.

From the formula in chapter 4, it is apparent that the camera resolution contributes the most to both minimal potential and uncertainty in potential. Nowadays, camera with the pixel size at $7\mu\text{m}$ is available in the market. The minimal potential would be $\frac{1}{3}$ of the value in this experiment. Further, fragments smaller than $50\mu\text{m}$ are able to be detected effectively with higher resolution and the required potential for those fragments would be lower. To acquire a proper potential value in this way, it depends more on the camera capability. A smaller potential could be acquired only if a smaller pixel size occurs.

Except the resolution, the gap between also contributes to the potential value. The gap is proportional to the potential value, though it has less contribution to the uncertainty than the resolution. A smaller gap, therefore, would make the potential lower. However, the gap is also confined by other conditions. The gap should be big enough to make the droplet breakup between the electrodes. Also, the gap cannot be too small to generate a large capacitance between two electrodes. A good range of the gap is about 50 to 60mm.

In conclusion, this experiment cannot effectively detect the charge distribution in fragments after secondary breakup due to the low resolution and electric intensity. However, it is still possible to achieve that as discussed above. And this requires better equipment and protection.

6. SUMMARY AND CONCLUSIONS

In this chapter, the contents in previous chapters would be summarized. Based on these conclusions, recommendations for future work would be presented.

6.1 Summary of Previous Chapters

The thesis focuses on the secondary atomization of charged drops in the bag regime secondary atomization. The literature review section shows that breakup fragment size, velocities, and charge-to-mass ratios have not been measured. The influence of applied voltage on breakup characteristics was determined through measurements of fragments sizes and velocities.

Shadowgraphy was used first to record images of drops undergoing breakup. Digital inline holography (DIH) was used next to acquire quantitative data. By reconstructing the holograms, fragments the position, velocity and size of each fragment was calculated by further processing the data.

From the experimental results, the size PDFs of both salt solution and ethanol were acquired. No apparent difference was observed at different charging voltages or for different fluids. The expressions of normalized size distribution function show little difference at different charge and Weber number. This is consistent with the FWHM and peak location results.

The velocity PDFs for, ethanol did not show much difference for either horizontal or vertical components when applied charging potential was altered. The results of vertical velocities, though, seem to have huge oscillations, still fall in the range of uncertainty.

To get the charge carried by each fragment, the acceleration is needed. With the applied electric field intensity and the mass of each fragment, the charge could be calculated. However, due to the low resolution of the camera, the required minimal electric field intensity is much larger than the maximum value for this apparatus. Even switching to a camera whose resolution was three

times the one used here does not lower the voltage enough to allow accurate results to be obtained.

6.2 Future Work

To further explore the charge distribution of fragments after the breakup of charged droplet, some adjustments on the camera resolution and the gap between electrodes of applied electric field are needed.

By minimizing the pixel size, the minimal detected velocity would be reduced. Similarly, a smaller gap between electrodes would make the electric field intensity larger when the applied potential is unchanged. Through these ways, the accurate value of charge distribution might be obtained.

In addition, this work is limited to the bag breakup regime. Bag breakup regime only takes a relatively narrow part in the whole secondary breakup map. The temperature and velocity change are small compared with other breakup modes. Therefore, more study at different breakup modes is needed.

Finally, further exploration on non-Newtonian liquid is also needed. The shear forces acting on non-Newtonian liquid drop would be different from the Newtonian situation, making the theoretical analysis more difficult. The breakup modes for charged non-Newtonian drops might be different from current studies due to the changes on the shear forces.

REFERENCES

- Aalburg C, van Leer B, Faeth GM (2003) Deformation and drag properties of round drops subjected to shock-wave disturbances. *AIAA Journal*. 41(12): 2371-2378.
- Babinsky E, Sojka PE (2002) Modeling drop size distributions. *Progress in Energy and Combustion Science*. 28(4): 303-329.
- Bailey AG (1988) *Electrostatic Spraying of Liquids*. New York: Wiley.
- Brodkey R (1967) Formation of drops and bubbles. In: *The Phenomena of Fluid Motions* Reading, MA: Addison-Wesley.
- Cao XK, Sun ZG, Li WF, Liu HF, Yu ZH (2007) A new breakup regime of liquid drops identified in a continuous and uniform air jet flow. *Physics of Fluids* 19(5):7.
- Castellanos A (1998) *Electrohydrodynamics*. Wien: Springer.
- Chang J-S, Kelly AJ, Crowley JM (1995) *Handbook of Electrostatic Processes*. New York: Marcel Dekker, Inc.
- Chen DR, Pui DYH (1997) Experimental investigation of scaling laws for electrospraying: Dielectric constant effect. *Aerosol Science and Technology*. 27(3):367-380.
- Chou WH, Faeth GM (1998) Temporal properties of secondary drop breakup in the bag breakup regime. *International Journal of Multiphase Flow*. 24(6): 889-912.
- Chou WH, Hsiang LP, Faeth GM (1997) Temporal properties of drop breakup in the shear breakup regime. *International Journal of Multiphase Flow*. 23(4): 651-669.
- Cloupeau M, Prunet-Foch B (1994) Electrohydrodynamic spraying functioning modes: a critical review. *Journal of Aerosol Science*. 25(6):1021-1036.
- Cloupeau M (1994) Recipes for use of EHD spraying in cone jet mode and notes on corona discharge. *Journal of Aerosol Science*. 25(6):1143-1157.
- Cohen RD (1994) Effect of viscosity on drop breakup. *International Journal of Multiphase Flow*. 20(1): 211-216.
- Cooper SC, Law SE (2003) Electrostatic sprays for sunless tanning of the human body. *Ieee Transactions on Industry Applications*. 42(2): 385-391.
- Crowley JM (1986) *Fundamentals of Applied Electrostatics*. New York: Wiley.
- Dai Z, Faeth GM (2001) Temporal properties of secondary drop breakup in the multimode breakup regime. *International Journal of Multiphase Flow*. 27(2): 217-236.

- Fox RW, McDonald AT (1998) *Introduction to Fluid Mechanics*, 5th ed. New York: Wiley.
- Gamero-Castano M, Hurby V (2002) Electrical measurements of charged sprays emitted by cone-jets. *Journal of Fluid Mechanics*. 459: 245-276.
- Gao J (2014) Development and applications of digital holography to particle field measurement and in vivo biological imaging. *Purdue University*. PhD thesis.
- Gelfand BE (1996) Droplet breakup phenomena in flows with velocity lag. *Progress in Energy and Combustion Science*. 22(3): 201-265.
- Gelfand BE, Gubin SA, Kogarko SM, Komar SP (1973) Singularities of the breakup of viscous liquid droplets in shock waves. *Journal of Engineering Physics and Thermophysics*. 25(3): 1140-1142.
- Gemci T, Hitron R, Chigier N (2002) Determination of individual droplet charge in electrosprays from PDPA measurements. *ILASS-Europe*.
- Guildenbecher DR, Sojka PE (2007) Secondary Breakup of Electrically Charged Newtonian Drops. *ASME International Mechanical Engineering Congress and Exposition*. November, Seattle, Washington, USA
- Guildenbecher DR. (2009) Secondary atomization of electrostatically charged drops. *Purdue University*. PhD thesis.
- Han J, Tryggvason G (1999) Secondary breakup of axisymmetric liquid drops. I. acceleration by a constant body force. *Physics of Fluids*. 11(12): 3650-3667.
- Han J, Tryggvason G (2001) Secondary breakup of axisymmetric liquid drops II. Impulsive acceleration. *Physics of Fluids* 13(6): 1554-1565.
- Hinze HO (1995) Fundamentals of the hydrodynamic mechanism of splitting in dispersion processes. *AIChE Journal*. 1(3): 289-295.
- Hsiang LP, Faeth GM (1992) Near-limit drop deformation and secondary breakup. *International Journal of Multiphase Flow*. 18(5): 635-652.
- Hsiang LP, Faeth GM (1993) Drop properties after secondary breakup. *International Journal of Multiphase Flow*. 19(5): 721-735.
- Hsiang LP, Faeth GM (1995) Drop deformation and breakup due to shock wave and steady disturbances. *International Journal of Multiphase Flow* 21(4):545-560.
- Hwang SS, Liu Z, Reitz RD (1996) Breakup mechanisms and drag coefficients of high-speed vaporizing liquid drops. *Atomization and Sprays*. 6(3): 353-376.
- Igra D, Ogawa T, Takayama K (2002) A parametric study of water column deformation resulting from shock wave loading. *Atomization and Sprays*. 12(5-6): 577-591.

- Igra D, Takayama A (2001) Investigation of aerodynamic breakup of a cylindrical water droplet. *Atomization and Sprays*. 11(2): 167-185.
- Jahannama MR, Watkins AP, Yule AJ (2005) Electrostatic effect on agricultural air-atomized sprays and deposition part I: an experimental study. *Atomization and Sprays*. 15: 603-628.
- Jain SS, Tyagi N, Prakash RS, Ravikrishna RV, Tomar G (2018) Secondary breakup of drops at moderate Weber numbers: Effect of Density ratio and Reynolds number.
- Joseph DD, Beavers GS, Funada T (2002) Rayleigh-Taylor instability of viscoelastic drops at high Weber numbers. *Journal of Fluid Mechanics*. 453: 109-132.
- Juan LD, Mora JFDL (1996) Charge and Size Distributions of Electrospray Drops. *Journal of Colloid and Interface Science*. 186: 280-293.
- Jurgen B, Gerhard W (1996) Experiments on Sticking, Restructuring, and Fragmentation of Preplanetary Dust Aggregates. *Icarus*. 143(1): 138-146.
- Kamphoefner FJ (1972) Ink jet printing. *IEEE Transactions on Electron Devices*. 19(4):584-593.
- Khosla S, Smith CE, Throckmorton RP (2006) Detailed understanding of drop atomization by gas crossflow using the volume of fluid method. In: *ILASS Americas, 19th Annual Conference on Liquid Atomization and Spray Systems*. Toronto, Canada, May.
- Kim JH, Nakajima T (1999) Aerodynamic influences on droplet atomization in an electrostatic spray. *JSME International Journal Series B-Fluids and Thermal Engineering*. 42(2): 224-229.
- Kim K, Turnbull RJ (1976) Generation of charged drops of insulating liquids by electrostatic spraying. *Journal of Applied Physics*. 47(5): 1946-1949.
- Klein S, McClintock F (1953) Describing uncertainties in single-sample experiments. *Mechanical Engineering*. 75: 3-8.
- Kulkarni V, Sojka PE (2014) Bag breakup of low viscosity drops in the presence of a continuous air jet. *Physics of Fluids* 26, 072103 (2014).
- Law ES (2001) Agricultural electrostatic spray application: a review of significant research and development during 20th century. *Journal of Electrostatics*. 51-52: 25-42.
- Lee CH, Reitz RD (2000) An experimental study of the effect of gas density on the distortion and breakup mechanism of drops in high speed gas stream. *International Journal of Multiphase Flow*. 26(2): 229-244.
- Lefebvre AH (1989) *Atomization and Sprays*. New York: Hemisphere Pub. Corp..
- Li XG, Li MS, Fu HJ (2005) Modeling the initial droplet size distribution in sprays based on the maximization of entropy generation. *Atomization and Sprays*. 15(3): 295-321.

- Liu AB, Reitz RD (1993) Mechanisms of air-assisted liquid atomization. *Atomization and Sprays*. 3(1): 55-75.
- Liu AB, Reitz RD (1997) An analysis of the distortion and breakup mechanisms of high speed liquid drops. *International Journal of Multiphase Flow*. 23(4): 631-650.
- Loeherke RI, Nagib HM (1972) Experiments on management of free-stream turbulence. *Advisory Group for aerospace Research and Development*. Report Number 598. North Atlantic Treaty Organization.
- Michelson D (1990) *Electrostatic Atomization*. Briston: Adam Hilger.
- Neukermans (1973) Stability criteria of an electrified liquid jet. *Journal of Applied Physics*. 44(10): 4769-4770.
- Pilch M, Erdman CA (1987) Use of breakup time data and velocity history data to predict the maximum size of stable fragments for acceleration-induced breakup of a liquid drop. *International Journal of Multiphase Flow*. 13(6):741-757.
- Ranger AA, Nicholls JA (1969) Aerodynamic shattering of liquid drops. *AIAA Journal*. 7(2): 285-290.
- Rayleigh L (1882) On the equilibrium of liquid conducting masses charged with electricity. *Philosophical Magazine*. 14:184-186.
- Riddick JA, Bunger WB (1970) *Organic Solvents, Physical Properties and Methods of Purification*, 3rd ed. New York: Wiley-Interscience.
- Schmelz F, Walzel P (2003) Breakup of liquid droplets in accelerated gas flows. *Atomization and Sprays*. 13(4): 357-372.
- Shraiber AA, Podvysotsky AM, Dubrovsky VV (1996) Deformation and breakup of drops by aerodynamic forces. *Atomization and Sprays*. 6(6): 667-692.
- Shrimpton JS (2003) Pulsed charged sprays: application to DISI engines during early injection. *International Journal for Numerical Methods in Engineering*. 58(3):513-536.
- Shrimpton JS, Laoonual Y (2006) Dynamics of electrically charged transient evaporating sprays. *International Journal for Numerical Methods in Engineering*. 67: 1063- 1081.
- Simmons HC (1977) The correlation of drop-size distributions in fuel nozzle sprays part I: the drop-size/volume-fraction distribution. *Journal of Engineering for Power*. 309-314.
- Simmons HC (1977) The correlation of drop-size distributions in fuel nozzle sprays part II: the drop-size/number distribution. *Journal of Engineering for Power*. 315-319.
- Taylor G (1964) Disintegration of water drops in an electric field. *Proceedings of the Royal Society of London Series A, Mathematical and Physical Sciences*. 280(1382):383-397.

- Taylor G (1966) Studies of electrohydrodynamics. I. the circulation produced in a drop by electrical field. *Proceedings of the Royal Society of London Series A, Mathematical and Physical Sciences*. 291:159-166.
- Theofanous TG (2004) Aerobreakup in rarefied supersonic gas flows. *Journal of Fluid Mechanics* 126(4):516-527.
- Turton R, Levenspiel O (1986) A short note on the drag correlation of spheres. *Powder Technol.* 47:83-86.
- Uematsu M, Frank EU (1980) Static dielectric constant of water and steam. *Journal of Physical Chemistry Reference Data*. 9(4): 1291-1306.
- Venter A, Sojka PE, Cooks RG (2006) Droplet dynamics and ionization mechanisms in desorption electrospray ionization mass spectrometry. *Analytical Chemistry*. 78(24): 8549-8555.
- Wadhwa AR, Magi V, Abraham J (2007) Transient deformation and drag of decelerating drops in axisymmetric flows. *Physics of Fluids*. 19(11): 20.
- Wierzbna A, Takayama K (1988) Experimental investigation of the aerodynamic breakup of liquid drops. *AIAA Journal*. 26(11): 1329-1335.
- Zeleny J (1915) On the conditions of instability of electrified drops, with applications to the electrical discharge from liquid points. *Proc. of the Cambridge Philosophical Society*. 18:71-83.
- Zhang HB, Edirisinghe MJ, Jayasinghe SN (2006) Flow behavior of dielectric liquids in an electric field. *Journal of Fluid Mechanics*. 558: 103-111.
- Zhou SL, Cook KD (2000) Probing solvent fractionation in electrospray droplets with laser-induced fluorescence of a solvatochromic dye. *Analytical Chemistry*. 72(5): 963-969.